

## **UC Merced**

### **UC Merced Electronic Theses and Dissertations**

#### **Title**

Single Molecule Manipulation and Visualization of DNA Biosensor Surface

#### **Permalink**

<https://escholarship.org/uc/item/77b7084x>

#### **Author**

Gu, Qufei

#### **Publication Date**

2020

Peer reviewed|Thesis/dissertation

UNIVERSITY OF CALIFORNIA, MERCED

# Single Molecule Manipulation and Visualization of DNA Biosensor Surface

A dissertation for the degree  
Doctor of Philosophy

in

Biological Engineering and Small-scale Technologies

by

Qufei Gu

2020

Committee members:

Professor Wei-Chun Chin, Chair

Professor Tao Ye

Professor Changqing Li

Professor Bin Liu

Chapter 2 © 2018 American Chemical Society

Chapter 4 © 2017 The Royal Society of Chemistry

All other chapters © 2020 Qufei Gu

The dissertation of Qufei Gu is approved, and it is acceptable in quality and form for publication on microfilm and electronically:

---

(Professor Tao Ye)

---

(Professor Changqing Li)

---

(Professor Bin Liu)

---

(Professor Wei-Chun Chin, Chair)

University of California, Merced

2020

## Dedication

To my father Jianzhong Gu, mother Liping Tang, father-in-law Yong Ma,  
mother in-law Chiyao Li, grandmothers, grandfathers, daughter Mercedia,  
son Maxwell and wife Xue Ma.

Thank you for all your support along the way.

And lastly, I dedicated this thesis to my hometown Suzhou (Soochow), which  
is way beautiful than Venice.

# Table of Contents

Signature Page .....	iii
List of Figures .....	viii
List of Tables.....	x
Acknowledgements .....	xi
Curriculum Vitae .....	xii
Publications .....	xiii
Abstract of the Dissertation.....	xiv
<b>Chapter 1 Challenges in Characterizing DNA Biosensors .....</b>	<b>1</b>
1.1. Scope of the dissertation.....	2
1.2. Overview of DNA biosensors .....	3
1.3. Heterogeneous DNA biosensor surface.....	3
1.4. Surface characterization methods and challenges .....	4
1.4.1. Ensemble-averaging based methods .....	4
1.4.2. Single-molecule based methods .....	5
1.5. Single-molecule atomic force microscope (SM-AFM) imaging of the biosensor surface .....	6
1.5.1. SM-AFM imaging .....	6
1.5.2. The need for a comprehensive approach .....	7
Tables .....	8
Figures.....	10
References .....	12
<b>Chapter 2 Single Molecule Characterization of DNA Surface Hybridization at a Model Electrochemical Biosensor .....</b>	<b>17</b>
2.1. Introduction .....	19
2.2. Methods and materials.....	21
2.2.1. Preparation of E-DNA sensors.....	21
2.2.2. E-DNA sensor hybridization and denaturation .....	22
2.2.3. Electrochemical Measurement .....	22
2.2.4. AFM imaging.....	22

2.2.5. Probe density and hybridization yield qunatification.....	23
2.2.6. Spatial statistical analysis of probe distributions .....	23
2.2.7. Dynamic light scattering measurements .....	23
2.2.8. Synthetic oligonucleotides .....	24
2.3. Results and discussions.....	24
2.4. Conclusions and outlook.....	31
Tables .....	32
Figures.....	34
References .....	49
<b>Chapter 3 Nanoscale Spatial Organization is a Major Determinant of the Hybridization Kinetics of Surface Immobilized Hairpin DNA Probes.....</b>	<b>55</b>
3.1. Introduction .....	57
3.2. Methods and materials.....	58
3.2.1. Materials.....	58
3.2.2. E-DNA sensor fabrication and hybridization.....	58
3.2.3. AFM measurement and image analysis.....	59
3.2.4. DLS measurement.....	59
3.2.5. Damköhler number .....	60
3.2.6. Irreversible first-order Langmuir.....	60
3.2.7. Cox proportional hazard model.....	60
3.2.8. Numerical simulation.....	61
3.3. Results and discussions.....	62
3.4. Conclusions and outlook.....	66
Tables .....	68
Figures.....	70
References .....	81
<b>Chapter 4 Molecular Conformations of DNA Targets Captured by Model Nanoarrays.....</b>	<b>84</b>
4.1. Introduction .....	86
4.2. Methods and materials.....	88
4.2.1. Materials.....	88

4.2.2.	Oligonucleotides .....	88
4.2.3.	Surface monolayer preparation .....	88
4.2.4.	Atomic force microscope and nanografting .....	88
4.2.5.	DNA surface hybridization .....	89
4.2.6.	AFM image analysis.....	89
4.2.7.	Nonspecific adsorption .....	89
4.3.	Results and discussions.....	89
4.4.	Conclusions and outlook.....	93
	Tables .....	95
	Figures.....	96
	References .....	108
<b>Chapter 5</b>	<b>Conclusions and Future Study .....</b>	<b>113</b>
5.1.	Summary and conclusion .....	114
5.2.	Direction for future research.....	115
	Tables.....	118
	Figures.....	120
	References .....	122



## List of Figures

Figure 1.1: Schematic of a DNA biosensor surface.....	10
Figure 1.2: Schematic and AFM images of the switchable surface .....	11
Figure 2.1: Schematic of a switchable E-DNA sensor surface .....	34
Figure 2.2: AFM images of the surface prepared using backfilling method ..	35
Figure 2.3: Comparison of DNA probe density and DPV signal .....	36
Figure 2.4: AFM images and spatial statistical analysis of E-DNA sensor surfaces at different probe densities .....	37
Figure 2.5: Comparison of DNA surface hybridization and DPV signal suppression .....	38
Figure 2.6: AFM images of E-DNA sensor surfaces exposed to high target concentrations .....	39
Figure 2.7: Evolution of spatial patterns of hybridized DNA probes.....	40
Figure 2.8: Tracking evolution of heterogeneous spatial patterns of DNA surface hybridization .....	41
Figure 2.9: Spatial statistical analysis of probe distributions .....	42
Figure 2.10: Absence of nonspecific adsorption of targets on MUDA SAM....	43
Figure 2.11: Absence of clustering of targets using linear probes .....	44
Figure 2.12: Spatial statistical analysis of unhybridized probes.....	45
Figure 2.13: Measuring the size distribution of target molecules .....	46
Figure 2.14: AFM images of the sensor surface exposed to small targets.....	47
Figure 2.15: AFM images of E-DNA sensor surface before and after denaturation.....	48
Figure 3.1: Schematic of the kinetics prediction approach .....	70
Figure 3.2: AFM images and spatial statistical analysis of DNA surface hybridization kinetics at different probe densities.....	71
Figure 3.3: Modeling and predicting the overall hybridization kinetics based on spatial pattern.....	72
Figure 3.4: Predicting the overall hybridization kinetics with similar probe densities but different probe spatial patterns .....	73
Figure 3.5: DLS measurement of target size distributions.....	74
Figure 3.6: AFM images of probe distributions in defective areas .....	75
Figure 3.7: Comparison of probe distribution between experiment and complete spatial randomness .....	76
Figure 3.8: Numerical simulation of hybridization kinetic traces .....	77
Figure 3.9: Comparison of AFM-derived kinetic traces and numerical simulations.....	78
Figure 3.10: Spatial statistical variance at different hybridization time .....	79
Figure 3.11: Absence of nonspecifically adsorbed targets on MUDA .....	80

Figure 4.1: Schematic of nanografting surface chemical patterns with DNA probes and capture of DNA targets.....	96
Figure 4.2: AFM images of nanografted MUDA squares in a MHDA SAM....	97
Figure 4.3: Height distribution of DNA probes in nanografted squares .....	98
Figure 4.4: AFM images of nanografted MUDA squares before and after target capture in a MHDA SAM.....	99
Figure 4.5: Absence of nonspecific adsorption of targets on nanoarrays.....	100
Figure 4.6: AFM images of nanografted MUDA squares after target capture in a MHD SAM.....	101
Figure 4.7: AFM images of nanografted MUDA squares with DNA probes in a MHDA SAM .....	102
Figure 4.8: Contour length distribution of targets on nanoarray .....	103
Figure 4.9: AFM images of captured targets aligned with MUDA/MHDA boundaries. ....	104
Figure 4.10: AFM images of captured long targets partially aligned with MUDA/MHDA boundaries.....	105
Figure 4.11: AFM images of nanografted MUDA hollow squares and triangles with DNA probes in a MHDA SAM.....	106
Figure 4.12: Absence of nonspecifically adsorbed targets on MHDA .....	107
Figure 5.1: CaDNAno diagram and scheme of mini DNA tiles.....	120
Figure 5.2: Schematic of DNA nanostructure-assisted lithography of probe patterns .....	121

## List of Tables

Table 1.1: Summary of conventional ensemble-averaging methods.....	8
Table 1.2: Summary of single-molecule methods. ....	9
Table 2.1: Summary of experimentally measured probe densities.....	32
Table 2.2: Summary of probe and target sequences.....	33
Table 3.1: Sequences and secondary structures of probe and target.....	68
Table 3.2: Summary of the probe insertion conditions.....	69
Table 4.1: Summary of experimentally measured oligonucleotide sequences .	95
Table 5.1: DNA staple sequences .....	118
Table 5.2: DNA scaffold sequences.....	119

## Acknowledgements

I would first like to show my appreciation and thankfulness to my advisor, Dr. Tao Ye for his support throughout my graduate study at the University of California, Merced (UC Merced), which have transformed me from a student to an engineer.

In addition, I would like to thank my committee, Dr. Changqing Li, Dr. Bin Liu and Dr. Wei-Chun Chin for taking their precious time to give me the advice that has greatly enhanced the quality and clarity of my dissertation.

I am grateful for my colleagues in UC Merced: Dr. Gary Robert Abel, who developed the high-resolution AFM imaging technique that I have used throughout my Ph.D. education; Dr. Huan Harrison Cao, who has helped in tracking evolution of DNA surface hybridization for my project and provided a lot of meaningful suggestions; Haiyang Wang, who has developed spatial statistical tools for analyzing the distribution of DNA probes; Yehan Zhang, who has performed DLS measurement on DNA aggregation; Warren Nanney and Zachary Petrek, who helped generating figures for publication; and Melissa Goodlad, Paniz Rahmani and Okan Ciftci who have shown friendships and great support which are very important to me.

Chapters 2 were adapted with permission from the American Chemical Society. Chapter 4 were adapted with permission from the Royal Society of Chemistry.

I want to thank James Duncan for being a great friend, especially for the days when we ate pizza in Dion's.

Finally, I would like to thank my parents for their unconditional love and support for 30 years. Thank you for my father for letting me travel around the world when I was a kid. It broadens my views and perspectives on the world around me. I am very lucky to have my parents-in-law, who helped taking care of my two newborn babies. I express my deepest gratitude to my loving wife Xue Ma, who has always been on my side all along from the time we were far apart across the Pacific Ocean and after reunited in the United States.

# CURRICULUM VITA

## EDUCATION

### **PhD in Biological Engineering and Small-scale Technologies**

University of California, Merced, Merced, CA, USA 2015-2020

### **Master of Science in Physics**

University of New Mexico, Albuquerque, NM, USA 2011-2014

### **Bachelor of Science in Physics**

Sichuan University, Chengdu, Sichuan, China 2007-2011

## RESEARCH EXPERIENCE

Merced Nanomaterials Center for Energy & Sensing 2015-2019

Tao Ye Lab, Biological Engineering & Small-scale Technologies,  
UC Merced 2015-2019

UNM Center for High Performance Computing 2011-2014

## AWARD & Honors

UC Merced Graduate Dean's Dissertation Fellowship Fall 2019

UC Merced BEST Summer Fellowship Summer 2019

UC Merced BEST Summer Fellowship Summer 2018

UC Merced BEST-funded Travel Fellowship Spring 2018

NASA-funded MACES Travel Fellowship Spring 2018

UC Merced BEST Summer Fellowship Summer 2017

NASA-funded MACES Research Fellowship Fall 2016

UC Merced BEST Summer Fellowship Summer 2016

NASA-funded MACES Research Fellowship Spring 2016

## Publications

### Journal Papers

1. **Qufei Gu**, Warren Nanney, Huan Harrison Cao, Haiyang Wang, and Tao Ye. Single Molecule Profiling of Molecular Recognition at a Model Electrochemical Biosensor. *J. Am. Chem. Soc.*, **2018**, *140*(43), 14134-14143.
2. Huan H. Cao, Gary R. Abel, **Qufei Gu**, Gloria-Alexandra V. Gueorguieva, Yehan Zhang, Warren A. Nanney, Eric Provencio and Tao Ye. Seeding the Self-Assembly of DNA Origami at Surfaces, *ACS Nano*, **2020**.
3. Hao Xian, Eric A. Josephs, **Qufei Gu**, and Tao Ye. Nanoscale Control of DNA Conformations on Surface Chemical Patterns. *Nanoscale*, **2017**, *9*, 13419-13424.

### Conference Proceeding Papers

1. **Qufei Gu** and Tao Ye. Correlation between Hybridization and Electrochemical Signal in Stem-loop E-DNA Sensors using Single-Molecule AFM. *ACS National Meeting & Exposition*, page 219, 2018.
2. Tao Ye, Huan Harrison Cao, **Qufei Gu** and Warren Nanney. Surface Seeded Self-assembly of DNA Nanostructures. *Functional DNA Nanotechnology Workshop*, page 124, 2018.
3. Tao Ye, **Qufei Gu**, Warren Nanney and Huan H. Cao, Nanoscale Insight into the Impact of Spatial Organization of Probe Molecules on Surface Hybridization. *MRS Spring Meeting & Exhibit*, 2018.

## Teaching Experience

Served as teaching assistant for *General Chemistry*, *Material Science & Engineering*, and *General Physics*

Guest-lectured for *Material Science & Engineering*

## Abstract of the Dissertation

### Single Molecule Manipulation and Visualization of DNA Biosensor Surface

by

Qufei Gu

Doctor of Philosophy in Biological Engineering and Small-Scale Technologies

University of California, Merced, 2020

Committee Chair: Professor Wei-Chun Chin

A central question in DNA biosensors is how the surface structure impact the molecular recognition, and ultimately the figures of merit of device function, such as sensitivity and reproducibility. Here is a quote from seminal work by Herne and Tarlov (1997): *“surprisingly little is known about the surface structures of bound probes and the impact of the surface on hybridization reaction.”* Two decades later, this remark is still valid, notwithstanding the exponentially increasing number of publications in DNA-based biosensors. The probe surface density is extensively investigated and used to the optimize the sensing properties. These studies must rely on the assumption that the probe distribution is homogeneous and the targets can access the immobilized probes with identical binding energies, and thus that the binding affinity and kinetics can be described by the ensemble average quantities. While such studies have revealed general trends of target recognition, these observables are far from adequate descriptors of the surface structures or complex surface interactions, especially in light of growing evidence that a realistic biosensor surface may be highly heterogeneous. In this dissertation, I performed single-molecule atomic force microscope (SM-AFM) imaging to resolve the closely-spaced individual probes as well as hybridization event on a functioning DNA biosensor surface. Chapter 1 provides the background and challenges in characterizing the surface structures of DNA biosensors, as well as an introduction to SM-AFM

imaging. In Chapter 2, I applied new spatial statistical tools to characterize the spatial patterns of probe distribution and correlated these patterns to interfacial molecular recognition, which provided new insights on molecular crowding. In Chapter 3, I modeled the surface hybridization kinetics based on spatial statistical information extracted from the AFM database. This raises the intriguing prospect that the spatial patterns of biosensor surface can be rationally tailored to improve the performance. In Chapter 4, AFM is used to generate single molecule nanoarrays with well-controlled chemical and morphological heterogeneities, which serve as a model system for studying the DNA-surface interactions. And finally, in Chapter 5, I summarized the main findings, and elaborated the future research topic on surface patterning of probes with DNA nanostructures.



# Chapter 1

## Challenges in Characterizing DNA

### Biosensors

The great gushing Yangtze with piling waves flows towards the east, away it carries gallant souls of the remote bygone days. The ancient fort on the west is said to be the Crimson Cliff, where Zhou of the Three Kingdoms era Wei's navy defeated. Stone were hurled into the sky indiscriminatingly, mighty waves must have crushed onto shores hurling high snow-like foam. The river and mountains today's landscapes paint, where once there were many courageous and heroic men. Picture Zhou in his prime, dressed in plain clothes together with his young bride, gallant he must have been. Topped with a silk crest, he held in his hand a fan of feathers, with humor he helped see to, that the masts and sculls of Wei's navy go up in smoke and ashes turn into. My mind wanders in the history vested hither, my sentimentality no doubt has caused my early grey. Life is a dream, allow me to libate a drink to the river, the moon and its reflection.

Su Shi, Remembrance of the Table of the Crimson Cliff

## 1.1. Scope of the dissertation

Deoxyribonucleic acid (DNA) biosensors are analytical devices that use DNA as a recognition element and transduce binding events into physically detectable signals. They are appealing alternatives to conventional antibody-based assays for targeted molecular recognition due to their advantages of low cost, high affinity and stability, small size, and ease of modification. While rapid progress has been made in bioanalytical development, clinically or commercially successful DNA biosensors are still lacking because of the limited sensitivity and reproducibility originated from batch-to-batch variation in sensor fabrication. The objective of this thesis is to trace the origin of sensor-to-sensor variation in sensing performance, with a particular focus on understanding the molecular environment at the biosensor interface. We leverage a dynamically switchable surface and single-molecule atomic force microscope (SM-AFM) imaging to map the closely spaced individual molecules on DNA biosensor surface, while maintaining the functionality of the system. We analyze and integrate the spatial information derived from AFM maps into a structure-function framework that has applicability in biosensor manufacturing.

In Chapter 1, an overview of DNA biosensor development and potential applications is provided. Surface heterogeneities originated from both the solid substrate and the passivating layer are discussed. Surface characterization modalities are then introduced, including both ensemble-averaging and single-molecule-based ones. Comparisons of different characterization modalities in terms of their advantages and disadvantages are also discussed. Additionally, single-molecule atomic force microscope (SM-AFM) imaging, the focus of this dissertation, is introduced from the aspects of surface patterning and interaction. The challenges and current advances in SM-AFM imaging are also discussed.

Chapter 2 and 3 are the main chapters of this thesis build upon SM-AFM imaging. In chapter 2, spatial patterns and surface hybridization of single molecules are resolved on a functioning electrochemical DNA biosensor. New insights are given on how molecular crowding impacts target binding. This finding also raises the prospect that the spatial patterns of biosensor surface can be tailored to improve the performance. We take one step further by applying single-molecule spatial statistical tools and developing a new model that connects nanoscale spatial patterns to target recognition (Chapter 3). We then verify this model by coupling it with the numerical simulation to predict the surface hybridization, which leads to a key step toward elucidating the structure-function relationship.

The molecular environment of DNA biosensor is a complex multicomponent system. Instead of the above-mentioned spatial patterns, we devote Chapter 4 to a SM-AFM study of how surface functionalities and morphologies impact the

conformation of DNA molecules by constructing model nanoarrays. The DNA conformations are found to be sensitive to both surface parameters, enabling potentially more complex sensing architectures on surface.

Chapter 5 summarizes the contributions of this work and areas for future research based on this SM-AFM platform.

## 1.2. Overview of DNA biosensors

A biosensor consists of two basic elements: a recognition element that recognizes the analyte of interest and a transducer element that converts the recognition event into detectable signals. Both of them are decisive factors in determining the sensitivity of the biosensor. The recognition element may be an enzyme, antibody, nucleic acid, or a combination of molecules. Among these recognition elements, Deoxyribonucleic acid (DNA) biosensors (genosensors), based on Watson-Crick base-pair complementarity,<sup>1</sup> have been extensively explored for their high binding specificity and physiochemical stability.<sup>2-9</sup> In general, DNA biosensors rely on the immobilization of a single-stranded DNA (probe) with a known sequence of bases onto an optical,<sup>10</sup> electrochemical,<sup>11</sup> or piezoelectric<sup>12</sup> transducer surface and its highly specific hybridization with the complementary DNA sequence (target). They allow rapid, highly sensitive, highly selective, and real time detection of DNA hybridization. In addition, the molecular recognition capability of DNA probes extends beyond nucleic acids. Some DNA biosensors incorporate DNA aptamer probes that can recognize small molecules, proteins and even cells.<sup>13-20</sup> Even though numerous applications have been developed, ranging from medical diagnostics<sup>21-22</sup> to environmental monitoring,<sup>23-25</sup> and even food analysis,<sup>26</sup> only a few DNA-based biosensors have successfully entered clinical and industrial use.<sup>27-28</sup> This is mostly because the current existing methods of sensor surface fabrication focusing on optimizing the desired probe-target interaction cannot guarantee consistent and reproducible sensing performance with limited knowledge of molecular environment at the biosensor interface, which is generally described by an idealized cartoon of grid-like DNA probe arrangement (Figure 1.1a).<sup>29</sup> However, for a practical biosensor surface consisting of neighboring DNA probes, target molecules, solution, solid substrate and passivating layer (film), with none of them being homogeneous (Figure 1.1b), this simple cartoon is not an adequate descriptor of the system; further information regarding the non-ideal nature of the multicomponent biosensor surface are still needed. This raises a question of what a realistic DNA biosensor surface “looks” like.

## 1.3. Heterogeneous DNA biosensor surface

The DNA biosensor surface is conventionally thought to be homogeneous in all aspects and all DNA probes possess identical binding affinities and association or dissociation kinetics for their targets in a way similar to that in

solution (Figure 1.1a),<sup>30</sup> which is also a prerequisite for the use of ensemble-averaging methods. However, in a real biosensor, the probes become heterogeneous upon immobilization on solid support due to the existence of defects in the solid substrate or passivating film. The defects are energetically favorable binding sites for DNA probes because of lower energy barrier. Intrinsic defects can exist on the surface of any solids consisting of random facets and even single-crystal have defective regions ranging from atomic scale steps<sup>31</sup> to micrometer scale scratches. Another important source of defects is the molecular grain boundaries induced by phase segregation of the passivating film<sup>32-33</sup> during assembly. Despite their different origins, both type of defects can coexist and be responsible for the clustering of surface-immobilized DNA probes caused by either probe-probe interaction or high local probe density in defective region (Figure 1.1b).<sup>34</sup>

The clustering of surface-bound probes introduces new complexity to biosensor application for two reasons. First, the clustering domain of probes favors the adsorption of targets through non-specific interactions and thus reduces the binding specificity.<sup>35-36</sup> Second, molecular crowding inhibits the specific binding of targets in the area of clustered probes, lowering the detection sensitivity.<sup>37-38</sup> Apart from the example of probe clustering, the heterogeneity of the biosensor surface can also arise from other features such as conformational change, surface morphology and chemical environment. Therefore, it is critical to determine the existence and extent of these heterogeneous features on the surface and how they affect the overall sensing performance. The ideal surface analysis methods should be sensitive to both nanoscopic nonidealities and macroscopic collective behaviors. This brings about the next question on how to characterize the heterogeneity of the biosensor surface.

## 1.4. Surface characterization methods and challenges

### 1.4.1. Ensemble-averaging based methods

The commonly used ensemble methods, averaging the measured parameters over the entire biosensor surface, inevitably lost important information on spatially localized signals. The advantages and disadvantages of the commonly used ensemble-averaging methods such electrochemical<sup>11</sup> and optical spectroscopic (ER<sup>39</sup>, IR<sup>40</sup>, SPR<sup>41-42</sup>, SERS<sup>43</sup> and QCM<sup>44</sup>) techniques are summarized in Table 1.1. It should be noted that, although these methods can measure average properties of the biosensor surface, including the molecular compositions, conformations and interactions, none of them provide any details on local heterogeneity. Take electrochemical methods as an example, it probes the biosensor interface through electron transfer and the measured current is the average of the entire sensor surface. As the electron transfer is a function of faradic impedance, defective areas (substrate or passivating film) with low

impedance should facilitate more rapid electron transport than those defect-free areas on surface.<sup>29</sup> However, the overall current cannot quantify or even distinguish between different local environments, hampering the effort to elucidate the surface heterogeneity. Moreover, the sensitivity of ensemble measurements depends strongly on the signal/noise ratio and drawbacks influencing the background signal such as nonspecific binding of targets, laser damage of biological sample and nanostructured surface can further reduce the sensitivity. Although ensemble averaging methods may directly show the existence of nonideal features (i.e., clustering of probes) by providing physical signals that are distinct from the homogeneous sensor surface, other approaches that can directly probe the local surface heterogeneity are still needed so as to correlate the ensemble-averaged signals to the actual physical structures of the DNA biosensor surface.

### 1.4.2. Single-molecule based methods

Beyond the conventional ensemble-averaged methods, a number of single-molecule approaches have been developed to characterize the surface structure of biosensors. A summary of the advantages and disadvantages of these techniques are given in Table 1.2. Total internal reflection fluorescence (TIRF) microscopy enables tracking of surface hybridization pathway of individual molecules<sup>30, 45</sup> and the large field of view is compatible with the micrometer-sized sensor surface.<sup>46</sup> However, the imaging is still limited to extremely diluted coverages because the lateral resolution is typically 100-200 nm, which is insufficient to resolve probe molecules on practical biosensor surfaces. In addition, it also suffers from photobleaching and the fluorescence tag may affect the target recognition. Label-free single-molecule imaging of DNA molecule with differential surface plasmon resonance (DPSR) has been reported.<sup>47</sup> But just like TIRF microscope, the lateral resolution is restricted to ~300 nm, making it difficult to be implemented into real biosensor surface where the probes are closely packed. Scanning probe microscopies including scanning tunneling microscope (STM)<sup>48-49</sup> and atomic force microscope (AFM)<sup>34, 50-51</sup> have been extensively used to study the DNA layer with a coverage compatible with practical biosensor surface. A major limitation of STM is that it cannot image thick insulating layers and only ordered SAM of short passivating molecules can be used.<sup>52</sup> Although a well-ordered SAM of long-chain molecules preventing the substrate from nonspecific adsorption of targets is desired for biosensor fabrication, such a surface is not compatible with STM. This limitation was shortly overcome by the invention of AFM<sup>53</sup> which depends on tip-surface interaction, rather than tip-surface conduction. An important requirement for AFM investigation is that the sample molecules must be immobilized on a flat surface, and in the case of weakly or partially bound molecules the AFM tip tends to move them. This is clearly illustrated by the observations that only the first few bases near the surface (tethering

point) of immobilized DNA probes can be resolved.<sup>50-51, 54</sup> The spatial information derived from the tethering point is capable of determining not only the density but also the spatial patterns of probes (Figure 1.1b). However, to assess the impact of the probe spatial organization on the sensor performance, it is equally important to have a complete picture of molecular structure of DNA probes and how the structure evolves during the sensing process. Therefore, careful control of the imaging conditions may result in more detailed information on surface structures.

## 1.5. Single-molecule atomic force microscope (SM-AFM) imaging of the biosensor surface

### 1.5.1. SM-AFM imaging

Immobilization of the sample is a key step toward successful AFM imaging of biological molecules. Till now, a few of sample preparation techniques based on cation-assisted DNA-mica interactions have achieved single-molecule resolution.<sup>55-60</sup> Since both DNA and mica surface are negatively charged under physiological conditions, positively charged cations (i.e.,  $Mg^{2+}$  and  $Ni^{2+}$ ) can serve as a salt bridge that promote the binding of DNA onto mica. We applied the same concept to the gold substrate passivated with carboxyl-terminated SAM that are deprotonated under a saline Tris-acetate-EDTA (STAE) buffer, making the SAM negatively charged.<sup>61</sup> DNA probes, once anchored into the SAM through gold-thiol bonds, can be repelled from the negatively charged SAM surface and stay in “free state” for facile hybridization (see left panel of Figure 1.2a). As a consequence, only the anchor points of probes can be resolved with AFM and appear as dot-like protrusions shown in the left column of Figure 1.2b. The probes can be strongly bound to the surface in the presence of divalent cations ( $Ni^{2+}$ ) and switch to an “immobilized state” (right panel of Figure 1.2a) for high-resolution imaging. Figure 1.2 shows the complete molecular structures of probes including both free probes (circular protrusions) and target-probe duplexes (worm-like protrusions). The distinct molecular structures before and after target capture allows us to directly quantify the hybridization yield by counting the number of each type of features. Importantly, these immobilized probes can return to their “free state” by removing the  $Ni^{2+}$  from the surface with STAE buffer, enabling continuous monitoring of the probe structures during the hybridization. A dynamically switchable surface (when coupled with AFM), capable of successive mapping of both the spatial distribution and conformational change of DNA probes at the single-molecule level, is a powerful surface characterization tool for heterogeneous biosensor surface. Despite the robustness of this approach, the scanning rate of conventional AFM is slow, thus making it implausible to perform nanoscopic characterization over the macro-sized biosensing surface.

Ultrafast scanning methods that can potentially image the entire sensor surface are still under development.<sup>62-63</sup>

### **1.5.2. The need for a comprehensive approach**

Ultimately, a thorough surface characterization of the heterogeneity of the biosensor surface requires not only the identification of localized nonideal features, but also the assessment of the global ensemble properties. On one hand, SM-AFM imaging technique introduced above can provide nanoscale spatial and structural information but are unable to cover the entire sensor surface. On the other hand, ensemble methods competent of measuring averaged properties are not sensitive to the local surface environment. Therefore, approaches combining SM-AFM and ensemble-averaging methods will connect the nanoscopic nonidealities with the macroscopic collective behaviors, thus moving beyond the simple cartoons of homogeneous biosensor surface.<sup>29</sup>

**Table 1.1.** Summary of Conventional Ensemble-Averaging Methods.

<b>Ensemble Method</b>	<b>Advantages</b>	<b>Disadvantages</b>
Electrochemical Method	Probe the entire sensor surface through electron transfer	Rely on the impedance or coulombic charge, do not reveal the extent of heterogeneity
Electroreflectance (ER)	Discriminate different components on the surface	Not sensitive to local environments
Infrared Spectroscopy (IR)	Provide molecular composition and orientation information	Not sensitive to local heterogeneity
Surface Plasmon Resonance (SPR)	Evaluate binding kinetics in real time	Require large area to be analyzed, suffer from nonspecific binding
Surface-enhanced Raman Spectroscopy (SERS)	Provide the molecular structure information, analyze multicomponent sample	Requires nanostructured surface, high energy laser may damage the bio-sample
Quartz Crystal Microbalance (QCM)	Detect the mass change in the order of nanogram	Suffer from nonspecific binding, not sensitive to local environments



**Table 1.2.** Summary of Single-Molecule Methods.

<b>Single Molecule Method</b>	<b>Advantages</b>	<b>Disadvantages</b>
Total Internal Reflection Fluorescence Microscope (TIRFM)	Measure the density and distribution of probes	Limited to low probe surface coverage, suffer from photo bleaching, require fluorescence labeling
Differential Surface Plasmon Resonance (DSPR)	High contrast single-molecule imaging	Only apply to extremely diluted probe coverage
Scanning Tunneling Microscopy (STM)	Provide atomic resolution	Small field of view, slow scanning
Atomic Force Microscope (AFM)	Provide nanometer resolution	Slow imaging, inability to achieve high resolution on most biochemical ligands, such as DNA and proteins, not compatible with rough surface

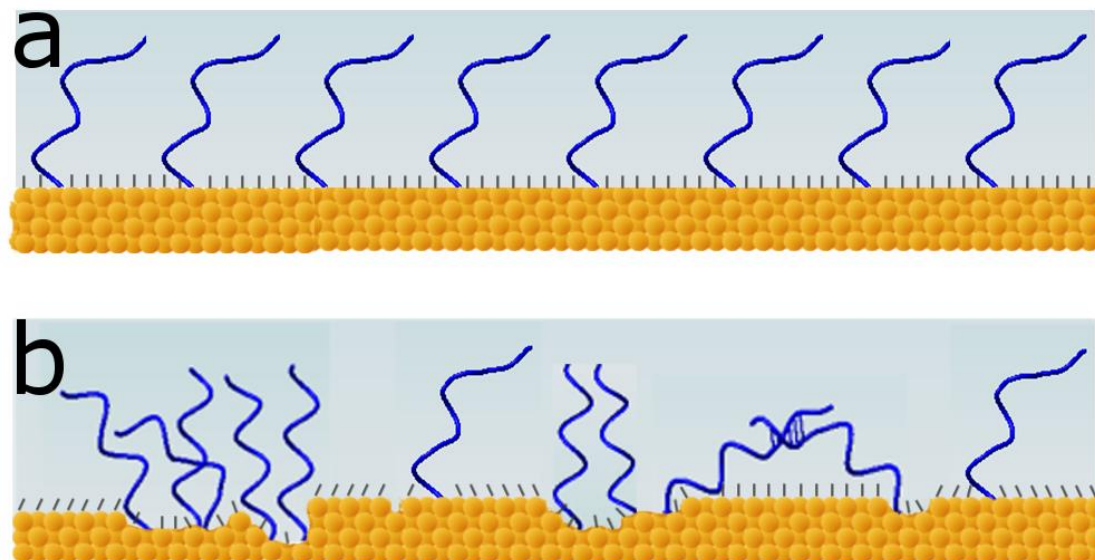


**Figure 1.1.** Schematic of a DNA biosensor surface comprised of surface-bound DNA probes (blue), solution (cyan), solid substrate (gold) and passivating layer (black). (a) grid-like DNA probe distribution, (b) clustering of DNA probes caused by either probe-probe interaction or high local probe density located in/near defects in the substrate (or the passivating layer).

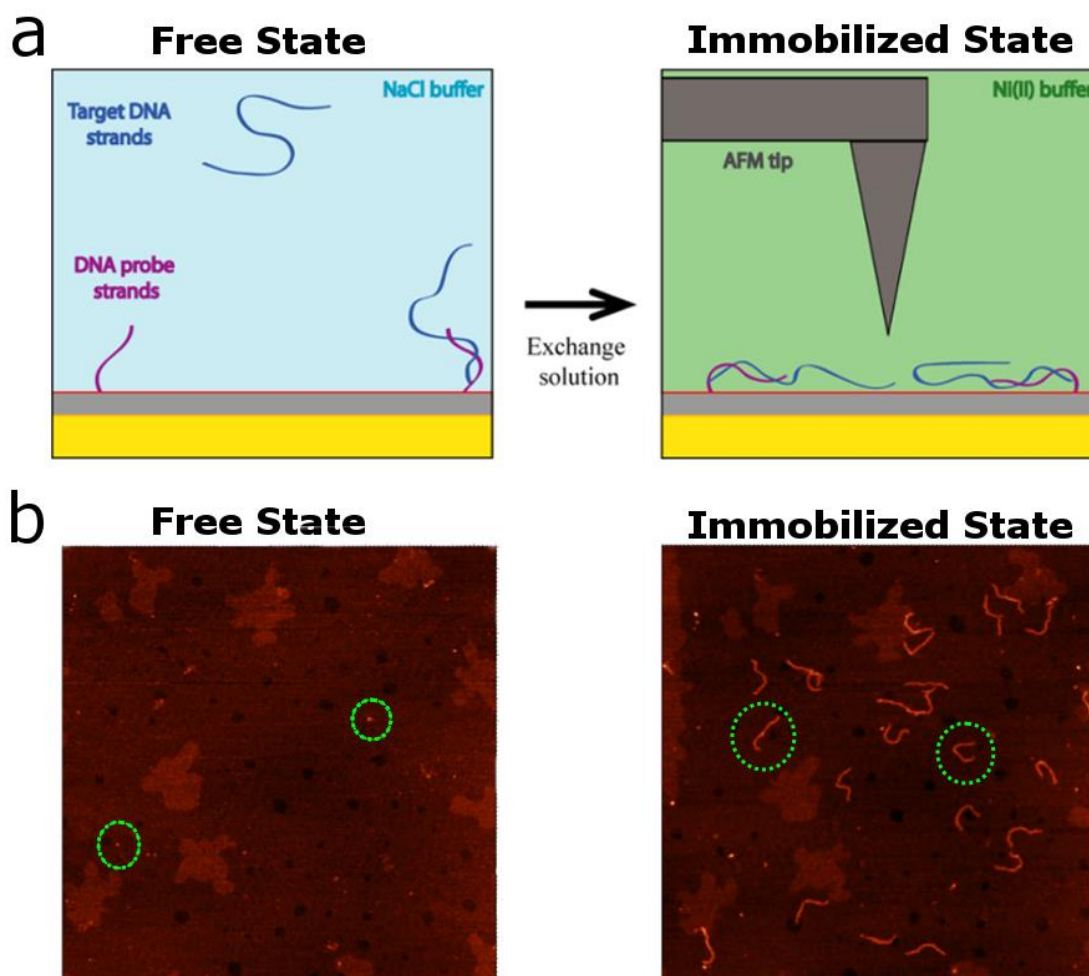


**Figure 1.2.** Schematic of a dynamically switchable surface. (a) DNA probes (pink) are covalently anchored to a carboxyl-terminated SAM on Au substrate and exposed to a STAE buffer containing complementary target DNA (blue). (left) After replacing the SATE solution with  $\text{Ni}^{2+}$  buffer, probes are strongly adsorbed onto the SAM surface and can be scanned by AFM (right). (b) AFM images of the biosensor surface with probes in “free state” (left) and “immobilized state” (right).

## References

1. Watson, J. D.; Crick, F. H. C., Molecular Structure of Nucleic Acids - a Structure for Deoxyribose Nucleic Acid. *Nature* **1953**, *171* (4356), 737-738.
2. Teles, F. R. R.; Fonseca, L. R., Trends in DNA Biosensors. *Talanta* **2008**, *77*(2), 606-623.
3. Du, Y.; Dong, S. J., Nucleic Acid Biosensors: Recent Advances and Perspectives. *Anal. Chem.* **2017**, *89*(1), 189-215.
4. Sassolas, A.; Leca-Bouvier, B. D.; Blum, L. J., DNA Biosensors and Microarrays. *Chem. Rev.* **2008**, *108*(1), 109-139.
5. Li, D.; Song, S. P.; Fan, C. H., Target-Responsive Structural Switching for Nucleic Acid-Based Sensors. *Accounts Chem. Res.* **2010**, *43*(5), 631-641.
6. Drummond, T. G.; Hill, M. G.; Barton, J. K., Electrochemical DNA Sensors. *Nature Biotechnology* **2003**, *21*(10), 1192-1199.
7. Liu, J. W.; Cao, Z. H.; Lu, Y., Functional Nucleic Acid Sensors. *Chem. Rev.* **2009**, *109*(5), 1948-1998.
8. Xiao, M. S.; Lai, W.; Man, T. T.; Chang, B. B.; Li, L.; Chandrasekaran, A. R.; Pei, H., Rationally Engineered Nucleic Acid Architectures for Biosensing Applications. *Chem. Rev.* **2019**, *119*(22), 11631-11717.
9. Wang, J., From DNA Biosensors to Gene Chips. *Nucleic Acids Res.* **2000**, *28*(16), 3011-3016.
10. Mirkin, C. A.; Letsinger, R. L.; Mucic, R. C.; Storhoff, J. J., A DNA-Based Method for Rationally Assembling Nanoparticles into Macroscopic Materials. *Nature* **1996**, *382*(6592), 607-609.
11. Fan, C. H.; Plaxco, K. W.; Heeger, A. J., Electrochemical Interrogation of Conformational Changes as a Reagentless Method for the Sequence-Specific Detection of DNA. *P. Natl. Acad. Sci. USA* **2003**, *100*(16), 9134-9137.
12. Okahata, Y.; Matsunobu, Y.; Ijiro, K.; Mukae, M.; Murakami, A.; Makino, K., Hybridization of Nucleic-Acids Immobilized on a Quartz Crystal Microbalance. *J. Am. Chem. Soc.* **1992**, *114*(21), 8299-8300.
13. Stojanovic, M. N.; de Prada, P.; Landry, D. W., Aptamer-Based Folding Fluorescent Sensor for Cocaine. *J. Am. Chem. Soc.* **2001**, *123*(21), 4928-4931.
14. Stojanovic, M. N.; Landry, D. W., Aptamer-Based Colorimetric Probe for Cocaine. *J. Am. Chem. Soc.* **2002**, *124*(33), 9678-9679.
15. Xi, Q.; Zhou, D. M.; Kan, Y. Y.; Ge, J.; Wu, Z. K.; Yu, R. Q.; Jiang, J. H., Highly Sensitive and Selective Strategy for Microrna Detection Based on Ws2 Nanosheet Mediated Fluorescence Quenching and Duplex-Specific Nuclease Signal Amplification. *Anal. Chem.* **2014**, *86*(3), 1361-1365.

16. Xiao, Y.; Lubin, A. A.; Heeger, A. J.; Plaxco, K. W., Label-Free Electronic Detection of Thrombin in Blood Serum by Using an Aptamer-Based Sensor. *Angew. Chem. Int. Edit.* **2005**, *44* (34), 5456-5459.
17. Fang, X. H.; Tan, W. H., Aptamers Generated from Cell-SeleX for Molecular Medicine: A Chemical Biology Approach. *Accounts Chem. Res.* **2010**, *43* (1), 48-57.
18. Meyer, S.; Maufort, J. P.; Nie, J.; Stewart, R.; McIntosh, B. E.; Conti, L. R.; Ahmad, K. M.; Soh, H. T.; Thomson, J. A., Development of an Efficient Targeted Cell-SeleX Procedure for DNA Aptamer Reagents. *Plos One* **2013**, *8* (8).
19. Sefah, K.; Shangguan, D.; Xiong, X. L.; O'Donoghue, M. B.; Tan, W. H., Development of DNA Aptamers Using Cell-SeleX. *Nat. Protoc.* **2010**, *5* (6), 1169-1185.
20. Xiao, Y.; Piorek, B. D.; Plaxco, K. W.; Heeger, A. J., A Reagentless Signal-on Architecture for Electronic, Aptamer-Based Sensors Via Target-Induced Strand Displacement. *J. Am. Chem. Soc.* **2005**, *127*(51), 17990-17991.
21. Mascini, M.; Tombelli, S., Biosensors for Biomarkers in Medical Diagnostics. *Biomarkers* **2008**, *13* (7-8), 637-657.
22. Singh, R.; Das Mukherjee, M.; Sumana, G.; Gupta, R. K.; Sood, S.; Malhotra, B. D., Biosensors for Pathogen Detection: A Smart Approach Towards Clinical Diagnosis. *Sensor Actuat. B-Chem.* **2014**, *197*, 385-404.
23. Chiti, G.; Marrazza, G.; Mascini, M., Electrochemical DNA Biosensor for Environmental Monitoring. *Anal. Chim. Acta.* **2001**, *427* (2), 155-164.
24. Rodriguez-Mozaz, S.; de Alda, M. J. L.; Barcelo, D., Biosensors as Useful Tools for Environmental Analysis and Monitoring. *Anal. Bioanal. Chem.* **2006**, *386* (4), 1025-1041.
25. Rodriguez-Mozaz, S.; de Alda, M. J. L.; Marco, M. P.; Barcelo, D., Biosensors for Environmental Monitoring - a Global Perspective. *Talanta* **2005**, *65* (2), 291-297.
26. Schaertel, B. J.; Firstenbergeden, R., Biosensors in the Food-Industry - Present and Future. *J. Food Protect.* **1988**, *51* (10), 811-820.
27. Ni, X.; Castanares, M.; Mukherjee, A.; Lupold, S. E., Nucleic Acid Aptamers: Clinical Applications and Promising New Horizons. *Curr. Med. Chem.* **2011**, *18* (27), 4206-4214.
28. Sundaram, P.; Kurniawan, H.; Byrne, M. E.; Wower, J., Therapeutic Rna Aptamers in Clinical Trials. *Eur. J. Pharm. Sci.* **2013**, *48* (1-2), 259-271.

29. Bizzotto, D.; Burgess, I. J.; Doneux, T.; Sagara, T.; Yu, H. Z., Beyond Simple Cartoons: Challenges in Characterizing Electrochemical Biosensor Interfaces. *ACS Sensors* **2018**, *3*(1), 5-12.
30. Peterson, E. M.; Manhart, M. W.; Harris, J. M., Single-Molecule Fluorescence Imaging of Interfacial DNA Hybridization Kinetics at Selective Capture Surfaces. *Anal. Chem.* **2016**, *88*(2), 1345-1354.
31. Goss, C. A.; Brumfield, J. C.; Irene, E. A.; Murray, R. W., Imaging and Modification of Au(111) Monatomic Steps with Atomic-Force Microscopy. *Langmuir* **1993**, *9*(11), 2986-2994.
32. Tamada, K.; Hara, M.; Sasabe, H.; Knoll, W., Surface Phase Behavior of N-Alkanethiol Self-Assembled Monolayers Adsorbed on Au(111): An Atomic Force Microscope Study. *Langmuir* **1997**, *13*(6), 1558-1566.
33. Vericat, C.; Vela, M. E.; Salvarezza, R. C., Self-Assembled Monolayers of Alkanethiols on Au(111): Surface Structures, Defects and Dynamics. *Phys. Chem. Chem. Phys.* **2005**, *7*(18), 3258-3268.
34. Herne, T. M.; Tarlov, M. J., Characterization of DNA Probes Immobilized on Gold Surfaces. *J. Am. Chem. Soc.* **1997**, *119*(38), 8916-8920.
35. Murphy, J. N.; Cheng, A. K. H.; Yu, H. Z.; Bizzotto, D., On the Nature of DNA Self-Assembled Monolayers on Au: Measuring Surface Heterogeneity with Electrochemical in Situ Fluorescence Microscopy. *J. Am. Chem. Soc.* **2009**, *131*(11), 4042-4050.
36. Yu, Z. L.; Yang, C. W. T.; Triffaux, E.; Doneux, T.; Turner, R. F. B.; Bizzotto, D., Measuring and Remediating Nonspecific Modifications of Gold Surfaces Using a Coupled in Situ Electrochemical Fluorescence Microscopic Methodology. *Anal. Chem.* **2017**, *89*(1), 886-894.
37. Ricci, F.; Lai, R. Y.; Heeger, A. J.; Plaxco, K. W.; Sumner, J. J., Effect of Molecular Crowding on the Response of an Electrochemical DNA Sensor. *Langmuir* **2007**, *23*(12), 6827-6834.
38. Peterson, A. W.; Heaton, R. J.; Georgiadis, R., Kinetic Control of Hybridization in Surface Immobilized DNA Monolayer Films. *J. Am. Chem. Soc.* **2000**, *122*(32), 7837-7838.
39. Sagara, T.; Kato, N.; Kakashima, N., Electroreflectance Study of Gold Nanoparticles Immobilized on an Aminoalkanethiol Monolayer Coated on a Polycrystalline Gold Electrode Surface. *J. Phys. Chem. B* **2002**, *106*(6), 1205-1212.
40. Limaj, O.; Etezadi, D.; Wittenberg, N. J.; Rodrigo, D.; Yoo, D. H.; Oh, S. H.; Altug, H., Infrared Plasmonic Biosensor for Real-Time and Label-Free Monitoring of Lipid Membranes. *Nano Lett.* **2016**, *16*(2), 1502-1508.

41. Abdulhalim, I.; Zourob, M.; Lakhtakia, A., Surface Plasmon Resonance for Biosensing: A Mini-Review. *Electromagnetics* **2008**, *28*(3).
42. Guo, X. W., Surface Plasmon Resonance Based Biosensor Technique: A Review. *J. Biophotonics* **2012**, *5*(7), 483-501.
43. Papadopoulou, E.; Gale, N.; Thompson, J. F.; Fleming, T. A.; Brown, T.; Bartlett, P. N., Specifically Horizontally Tethered DNA Probes on Au Surfaces Allow Labelled and Label-Free DNA Detection Using Sers and Electrochemically Driven Melting. *Chem. Sci.* **2016**, *7*(1), 386-393.
44. Okahata, Y.; Kawase, M.; Niikura, K.; Ohtake, F.; Furusawa, H.; Ebara, Y., Kinetic Measurements of DNA Hybridisation on an Oligonucleotide-Immobilized 27-Mhz Quartz Crystal Microbalance. *Anal. Chem.* **1998**, *70*(7), 1288-1296.
45. Monserud, J. H.; Schwartz, D. K., Mechanisms of Surface-Mediated DNA Hybridization. *ACS Nano* **2014**, *8*(5), 4488-4499.
46. Lu, X.; Nicovich, P. R.; Gaus, K.; Gooding, J. J., Towards Single Molecule Biosensors Using Super-Resolution Fluorescence Microscopy. *Biosens. Bioelectron.* **2017**, *93*, 1-8.
47. Yu, H.; Shan, X. N.; Wang, S. P.; Chen, H. Y.; Tao, N. J., Plasmonic Imaging and Detection of Single DNA Molecules. *ACS Nano* **2014**, *8*(4), 3427-3433.
48. Wackerbarth, H.; Grubb, M.; Zhang, J. D.; Hansen, A. G.; Ulstrup, J., Long-Range Order of Organized Oligonucleotide Monolayers on Au(111) Electrodes. *Langmuir* **2004**, *20*(5), 1647-1655.
49. Wackerbarth, H.; Marie, R.; Grubb, M.; Zhang, J. D.; Hansen, A. G.; Chorkendorff, I.; Christensen, C. B. V.; Boisen, A.; Ulstrup, J., Thiol- and Disulfide-Modified Oligonucleotide Monolayer Structures on Polycrystalline and Single-Crystal Au(111) Surfaces. *J. Solid State Electr.* **2004**, *8*(7), 474-481.
50. Josephs, E. A.; Ye, T., Electric-Field Dependent Conformations of Single DNA Molecules on a Model Biosensor Surface. *Nano Lett.* **2012**, *12*(10), 5255-5261.
51. Josephs, E. A.; Ye, T., Nanoscale Spatial Distribution of Thiolated DNA on Model Nucleic Acid Sensor Surfaces. *ACS Nano* **2013**, *7*(4), 3653-3660.
52. Binnig, G.; Rohrer, H., Scanning Tunneling Microscopy. *Ibm. J. Res. Dev.* **1986**, *30*(4), 355-369.
53. Binnig, G.; Quate, C. F.; Gerber, C., Atomic Force Microscope. *Phys. Rev. Lett.* **1986**, *56*(9), 930-933.

54. Bosco, A.; Bano, F.; Parisse, P.; Casalis, L.; DeSimone, A.; Micheletti, C., Hybridization in Nanostructured DNA Monolayers Probed by Afm: Theory Versus Experiment. *Nanoscale* **2012**, *4* (5), 1734-1741.
55. Brack, C., DNA Electron Microscopy. *CRC Crit. Rev. Biochem.* **1981**, *10* (2), 113-169.
56. Rivetti, C.; Guthold, M.; Bustamante, C., Scanning Force Microscopy of DNA Deposited onto Mica: Equilibration Versus Kinetic Trapping Studied by Statistical Polymer Chain Analysis. *J. Mol. Biol.* **1996**, *264* (5), 919-932.
57. Vesenka, J.; Guthold, M.; Tang, C. L.; Keller, D.; Delaine, E.; Bustamante, C., Substrate Preparation for Reliable Imaging of DNA Molecules with the Scanning Force Microscope. *Ultramicroscopy* **1992**, *42-44* ( Pt B), 1243-1249.
58. Hansma, H. G.; Laney, D. E., DNA Binding to Mica Correlates with Cationic Radius: Assay by Atomic Force Microscopy. *Biophys. J.* **1996**, *70* (4), 1933-1939.
59. Hansma, H. G.; Vesenka, J.; Siegerist, C.; Kelderman, G.; Morrett, H.; Sinsheimer, R. L.; Elings, V.; Bustamante, C.; Hansma, P. K., Reproducible Imaging and Dissection of Plasmid DNA under Liquid with the Atomic Force Microscope. *Science* **1992**, *256* (5060), 1180-1184.
60. Bezanilla, M.; Drake, B.; Nudler, E.; Kashlev, M.; Hansma, P. K.; Hansma, H. G., Motion and Enzymatic Degradation of DNA in the Atomic Force Microscope. *Biophys. J.* **1994**, *67* (6), 2454-2459.
61. Abel, G. R., Jr.; Josephs, E. A.; Luong, N.; Ye, T., A Switchable Surface Enables Visualization of Single DNA Hybridization Events with Atomic Force Microscopy. *J. Am. Chem. Soc.* **2013**, *135* (17), 6399-6402.
62. Ando, T.; Kodera, N.; Takai, E.; Maruyama, D.; Saito, K.; Toda, A., A High-Speed Atomic Force Microscope for Studying Biological Macromolecules. *Proc. Natl. Acad. Sci. USA* **2001**, *98* (22), 12468-12472.
63. Ida, H.; Takahashi, Y.; Kumatani, A.; Shiku, H.; Matsue, T., High Speed Scanning Ion Conductance Microscopy for Quantitative Analysis of Nanoscale Dynamics of Microvilli. *Anal. Chem.* **2017**, *89* (11), 6016-6021.

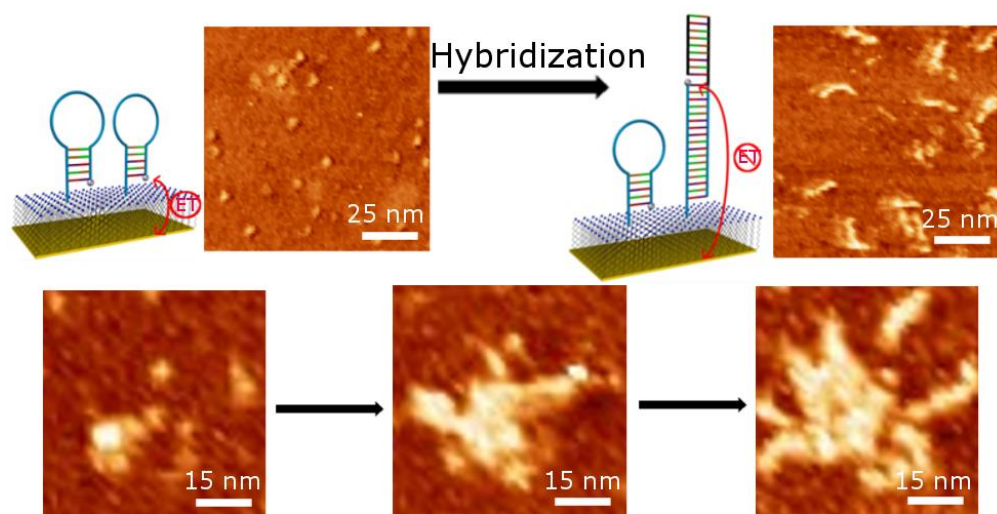


## Chapter 2

# Single Molecule Characterization. of DNA Surface Hybridization at a Model Electrochemical Biosensor

Raging with fury that raises my hair and topple my crest, I lean against a rail as heavy rain breaks, I look up to roar at the sky, with high hopes at heart. Achieving high ranks by thirty on dusty battlefields, and dusty the ranks are, means three thousand miles on the road following clouds and many a moon. Never take for granted time, once hair has greyed, there leaves only regret. As long as the Jingkang disgrace still awaits revenge, how can my remorse be laid to rest? We shall charge our chariots to stomp out all intruders on the Helan Pass. I swear we'd feed on the flesh of the northern tribes when hungry, and cheerfully drink their blood when thirsty. The day we recover what used to be our territory, we'd pay our respect in the direction of the Gate of Heaven.

Yue Fei, Lyrics to the Melody of a River of Blossoms



**Abstract:** The spatial organization of target and probe molecules on the biosensor is a crucial aspect of the biointerface structure that ultimately determines the properties of DNA surface hybridization and the performance of the biosensing. However, the spatial arrangements of single molecules on practical biosensors have been unknown, hampering the effort to rationally engineer biosensors. Here we have employed high resolution atomic force microscopy to map closely positioned individual probes as well as discrete hybridization events on a functioning electrochemical DNA sensor surface. We also developed and apply spatial statistics to characterize the spatial arrangements at nanometer level. We observed the emergence of heterogeneous spatiotemporal patterns of interfacial molecular recognition of stem-loop probes. The clustering of target capture suggests that surface hybridization may be enhanced by proximity of probes and targets that are about 10 nm apart. The counter-intuitive enhancement was rationalized by the complex interplay between the nanoscale spatial pattern of probe molecules, the conformational changes of the probe molecules, and target recognition. Such single molecule information may allow us to tailor the spatial organization of the biosensor surfaces to increase both the sensitivity and reproducibility.

## 2.1. Introduction

Biosensors typically consist of biorecognition components immobilized on the surfaces of materials that transduce recognition events into measurable signals. For instance, the electrochemical DNA (E-DNA) sensors,<sup>1-2</sup> which are leading candidates for point-of-care diagnostic systems due to their high specificity and sensitivity in detecting a broad range of biomarkers in complex biofluids or even in vivo,<sup>3</sup> immobilize nucleic acid capture probes onto the electrode surfaces. As DNA surface hybridization is influenced by the complex interactions between the probe and the biointerface, which comprised of neighboring probe molecules and captured target molecules in close proximity, the solid substrate (planar<sup>3</sup> or nanostructured surfaces<sup>4-5</sup>), the passivating layer, and the solution,<sup>6-7</sup> a main bottleneck is that the influences of the biointerface are complicated and challenging to predict, making it difficult to engineer biosensors with predictable performance. The effects of probe design,<sup>8</sup> probe surface coverage,<sup>9-12</sup> surface chemistry,<sup>13-14</sup> and surface morphology<sup>15</sup> on sensing performance have been extensively explored. However, one aspect that has been neglected is how spatial patterns of probe and captured target molecules impacts target binding. The spatial organization is a crucial aspect of the biointerface structure that ultimately determines the properties of DNA surface hybridization and the complex interactions. The heterogeneity of local probe density was thought to have difficult-to-predict influences on the accessibility of target molecules to the capture probes (molecular crowding).<sup>11, 16-17</sup> Many studies indirectly evidenced that the influences of the poorly controlled, often heterogeneous spatial arrangement of capture probes<sup>18</sup> may be significant: they may not only reduce detection sensitivity<sup>4, 17</sup> but also be the principle cause of the undesired batch-to-batch signal variabilities<sup>6, 19-22</sup> of many of these surface-based biosensing assays. Procedures that promote the dispersion of surface-immobilized probe molecules<sup>18</sup> were found to enhance reproducibility in target binding.<sup>19, 22-23</sup> Moreover, the assembly of capture probes into three-dimensional DNA tetrahedral nanostructures increased the hybridization rate by orders of magnitude.<sup>17, 24-25</sup> It was proposed that the large footprint of the tetrahedral nanostructures helps maintain uniform inter-probe separations and facilitate molecular recognition.

However, a definitive correlation between nanoscale spatial organizations and DNA surface hybridization had remained elusive because existing imaging techniques cannot resolve single molecules on biosensors.<sup>26-27</sup> On a practical biosensor surface with a probe density ranging from  $10^{10}$  to  $10^{13}$  probes/cm<sup>2</sup>, or  $10^2$  to  $10^5$  probes/ $\mu\text{m}^2$ ,<sup>7, 28</sup> many of the probe molecules are closely packed and separated by 10 nm or less, which is beyond the resolving ability of existing techniques. Although a few techniques, such as atomic force microscopy<sup>31</sup>, fluorescence microscopy<sup>27, 29-30</sup> and surface plasmon resonance<sup>32</sup> have detected single recognition events, these techniques in general are only suitable for

surfaces with extremely dilute coverages of molecules. So far knowledge of how surface immobilization impacts molecular recognition has been almost all derived from studies measuring average surface densities.<sup>11, 26, 33</sup> While such studies have demonstrated general characteristics indicating that molecular crowding by probe molecules<sup>11, 16-17</sup> and captured targets<sup>34</sup> hinders DNA surface hybridization, these ensemble averaging observables alone are inadequate descriptors of the molecular crowding, especially in the context of growing evidence that a practical biosensor may be highly heterogeneous in probe density.<sup>6, 18</sup> In addition, the complex impacts of other surface parameters such as surface chemistry, surface morphology<sup>35</sup> and molecular conformations<sup>6-7</sup> may compound the difficulty in interpreting crowding interactions.

Previously, using surfaces that can switch interactions with DNA on demand,<sup>18, 36-37</sup> we have for the first time allowed atomic force microscopy (AFM) to spatially resolve individual DNA molecules that are covalently attached to gold passivated with self-assembled monolayers (SAMs),<sup>38</sup> which underlines a broad range of electrochemical biosensors. However, our previous work did not elucidate the complex relationship between the surface conformation of the DNA probes and the target hybridization, as the surface hybridization kinetics was determined using the overall hybridization yield, which is an ensemble-averaging observable that conveys limited information on an intrinsically heterogeneous surface. In addition, how the surface structure affects the electrochemical signals was unknown because the imaging was not performed on functioning electrochemical biosensors.

In order to deal with the above problems, we have investigated for the first time how the spatial organizations of individual probes impact the DNA surface hybridization of a functioning biosensor. We built model surfaces that serve as electrochemical DNA sensors and at the same time employed AFM to spatially resolve target recognition even when the inter-probe separation is less than 10 nm, thus enabling monitoring of the regime where molecular crowding is important. The biosensor surfaces consisting of electroactive DNA probes attached to highly ordered SAMs, make it possible to modulate interaction with DNA<sup>36</sup> and provide an ideal platform for examining how spatial organizations of single molecules alters surface hybridization as these surfaces minimize the impact of difficult-to-control morphological and compositional heterogeneities. Moreover, our study revealed unexpected spatiotemporal patterns of surface hybridization by applying spatial statistics including Ripley's K function,<sup>39-41</sup> nearest-neighbor distances, local crowding indices to describe heterogeneous probe distribution in target binding.<sup>18</sup> The hybridization yields of probe molecules were found to change markedly with the nearest neighbor-distance. Hybridization of DNA targets with stem-loop probes preferentially appears in the region where the probes are clustered, suggesting that the interactions between molecules separated by  $\sim 10$  nm may enhance target binding of structured probes. Contrary to the prevailing view

that increasing crowding interaction inhibits target binding,<sup>11, 16, 33</sup> the cooperative effect reveals new mechanisms through which the surface structure can impact target capturing.

Our study provided the first definitive evidence that, surface structure of bound probes, *i.e.*, the nanoscale spatial organization of probe molecules exerts a profound impact on interfacial molecular recognition. Our findings have ramifications in biosensor design, as the sensitivity of a biosensor is directly linked to target recognition. The dramatic effect of the nearest-neighbor distance on surface hybridization opens a new avenue to increase the sensitivity: we may carefully design the spatial patterns to favor inter-probe separations with maximized hybridization efficiency. It should also be emphasized that the nanoscale spatial pattern likely has important but not fully understood impacts on almost all surface-based biosensors.<sup>4, 42-43</sup> In addition to surface hybridization, our approach of incorporating single molecule spatial statistics into spatially resolved measurement on model sensor surfaces may be applied to other types of molecular recognition, such as aptamer-based sensors that detect proteins.<sup>24, 44-45</sup> How complex intermolecular interactions at the surface influence the pathways of interfacial molecular recognition remain largely undetermined. Therefore, monitoring and analyzing these biointerfaces at the molecular scale will identify strategies that can help improve the performance of these biosensors.

## 2.2. Method and materials

### 2.2.1. Preparation of E-DNA sensors

All oligonucleotide sequences are summarized in Table 2.2. Unless otherwise stated, all chemicals were obtained from Fisher Scientific Co. (Pittsburg, PA, USA). Insertion Method: An Au (111) single crystal disk (MaTeck GmbH, Juelich, Germany) substrate was used for both electrochemical measurement and AFM imaging. The Au single crystal disk was treated in hot nitric acid for 20 min and annealed with hydrogen flame just before SAM preparation.<sup>36-37</sup> The Au substrate was then immersed into 1 mM MUDA (Sigma-Aldrich Co., St. Louis, MO, USA) solution in 9:1 ethanol (VWR, Radnor, PA, USA):acetic acid for 1 h. The disulfide DNA probes (P1 or P2) were reduced in 2mM TCEP (Tris-(2-carboxyethyl)-phosphate, Sigma-Aldrich Co., St. Louis, MO, USA) at room temperature for 20 min and then purified using a QIAquick Nucleotide Removal Kit (QIAGEN, Germantown, MD, USA) and stored at -20°C. After 1 h, the Au substrate was thoroughly rinsed with 9:1 ethanol:acetic acid and water, blown dried with filtered air, and incubated with a buffer containing the thiolated DNA probes, 50 mM NaAc, and 2 mM TCEP for 30 minutes. Following the insertion step, the substrate was rinsed 3 times with a TAE (40 mM Tris-acetate and 1 mM EDTA, pH 8.3) buffer to remove nonspecific probe adsorption. Backfilling Method: The Au

substrate was treated in hot nitric acid for 20 min and annealed with hydrogen flame just before probe deposition. The cleaned Au substrate was immersed into a buffer containing the 20 nM thiolated DNA probes, 50 mM NaAc, and 2 mM TCEP for 1 h. After DNA probe assembly, the Au disk substrate was backfilled with 1 mM MUDA solution in 9:1 ethanol:acetic acid for 3h. Following the backfilling step, the substrate was thoroughly rinsed with in 9:1 ethanol:acetic acid and TAE buffer.

### **2.2.2. E-DNA sensor hybridization and denaturation**

The hybridization was carried out by incubating the sensor surface with a buffer containing DNA targets (T1 or T2), 1x PBS7 (10 mM Phosphate, 1M NaCl, pH 7) at room temperature in the dark. After a predetermined hybridization time, the sensor surface was then rinsed 3 times with an STAE buffer (1x TAE, 200 mM NaCl) to remove nonspecifically bound targets. To track the hybridization kinetics, the sensor surface was regenerated by immersion in an alkaline buffer (1x AB = 10 mM NaOH, 330  $\mu$ M EDTA, pH 12) for 5 minutes after each target incubation, followed by thorough rinsing with STAE to remove the denatured targets. The denatured sensor surface is shown in Figure 2.15.

### **2.2.3. Electrochemical measurement**

A home-made Ag/AgCl (3M KCl) reference electrode was used to match the size of the AFM liquid cell. As Cl<sup>-</sup> ion is a contaminant that can specifically adsorb onto gold substrate, we have designed a small electrode compartment where only limited ions could diffuse out from the reference electrode into the AFM liquid cell. Small drift in the potential of the home-made Ag/AgCl electrodes is commonly observed over long time storage. Therefore, the potential of these electrodes is calibrated versus commercially available Ag/AgCl electrodes for accurate measurement. All DPV measurement was carried out relative to a home-made Ag/AgCl reference electrode at room temperature using an Epsilon electrochemical analyzer (BASI, West Lafayette, IN, USA). A scan frequency of 100 Hz between -0.4 V to -0.1 V (vs. Ag/AgCl) and the pulse amplitude was 50 mV. An Au single crystal disk was used as a working electrode, together with a platinum counter electrode. In all experiment, the PBS7 was used as the electrolyte, which was nitrogen purged for 10 min prior to the start of measurement.

### **2.2.4. AFM imaging**

All AFM images (except Figure 2.8) were acquired in the topography mode and were taken with high resolution 256 pixels x 256 pixels at one line per second using Agilent/Keysight 5500 AFM (Keysight Technologies, Santa Rosa, CA, USA) and Ntegra Vita AFM (NT-MDT Co., Moscow, Russia) equipped with SNL-10 cantilevers (spring constants of 0.2-0.4 N/m, Bruker, Bellerica, MA,

USA) under a  $\text{Ni}^{2+}$  buffer (5 mM  $\text{NiAc}_2$ , 0.1x TAE). Tapping mode AFM imaging with a resonant frequency of approximately 16 kHz was carried out. After imaging, the sensor surface was thoroughly rinsed with the STAE buffer to remove  $\text{Ni}^{2+}$  cations by chelation.

### 2.2.5. Probe density and hybridization yield quantification

In order to measure the surface probe densities, AFM imaging was performed in at least four different areas of the Au substrate. An average probe density (molecules/area) in the absence of target molecules was estimated by counting the number of corresponding features (8 nm diameter circular protrusions) in images using Gwyddion (<http://gwyddion.net/>) and WSxM<sup>46</sup> image process software. The number of hybridized probes after hybridization (~20 nm long worm-like protrusions) was estimated in the same manner as the above. The hybridization yield was then calculated as the number of hybridized probes divided by the total number of probes after hybridization.

### 2.2.6. Spatial statistical analysis of probe distributions

Gwyddion image processing software was utilized to extract the XY-coordinates of DNA probes from AFM images. A mask was generated for all features that are above the minimal pixel area and height threshold. Minor manual editing was performed to separate the partially overlapping features, especially for surfaces at higher probe densities. The coordinates of the centroids were then used to calculate the Ripley's  $K(r)$  function as well as  $[K(r)/\pi]^{1/2} - r = L(r) - r$ .<sup>40</sup> The observed  $L(r) - r$  can be compared side-by-side with the corresponding data under complete spatial randomness (CSR) realized by Monte Carlo simulation. 999 simulations were carried out to minimize the sampling uncertainty and calculate the quantiles of  $L(r) - r$  for each value of  $r$ , in which 0.025 and 0.975 quantiles were directly compared with  $L(r) - r$ . The same coordinates were also utilized for N.N.D. and LCI analyses, where the former determines the distance between a probe and its closest neighboring probe, while the latter counts the number of probes surrounding a specific probe.

### 2.2.7. Dynamic light scattering measurements

The sample solutions containing different concentrations of T1 targets (10 nM, 100 nM and 1 $\mu$ M) were prepared in PBS7 (10 mM Phosphate, 1M NaCl, pH 7) buffer. A quartz cuvette (ZEN2112) QS 3.00 mm from Malvern Instruments Ltd., (Malvern, UK) was used to determine the aggregation of the target molecules. DLS measurements were performed using a Malvern Zetasizer Nano-S90 from Malvern Instruments Ltd. under the following conditions: wavelength, 633 nm; scattering angle, 90°; temperature, 25°C; accumulation time, 100 sec. The hydrodynamic sizes of the DNA targets in buffer solution are classically calculated using the Stokes-Einstein equation:

$$d = \frac{kT}{3\pi\eta D} \quad (2.1)$$

where  $k$  is the Boltzmann constant,  $T$  is the temperature,  $\eta$  is the viscosity,  $D$  is the diffusion coefficient.

### 2.2.8. Synthetic oligonucleotides

The oligonucleotide probes (P1, P2) were separated and purified using Anion exchange HPLC (AX-HPLC) from Biosearch Technologies (Petaluma, CA, USA). The oligonucleotide targets (T1, T2) with standard desalting were purchased from Integrated DNA Technologies (Coralville, IA, USA) and used without further purification.

## 2.3. Results and discussion

To characterize target capture by electrochemical DNA sensors at the single molecule level, we assembled a 11-mercaptoundecanoic acid (MUDA) SAM on single-crystal Au(111) disk electrodes, then 23-base hairpin probes (P1) containing a methylene blue (MB) redox tag<sup>47</sup> on the 3' end and a terminal thiol group on the 5' end were attached to the SAM (insertion method, see Methods for details), which generates a relatively uniform spatial organization of probes,<sup>18</sup> contrasting the commonly used conventional backfilling method (Figure 2.2).<sup>10</sup> It should be noted that the carboxyl groups are deprotonated under buffer conditions (pH  $\sim$ 7), resulting in a negatively charged MUDA SAM. Similar negatively charged SAMs have been employed for electrochemical DNA sensors in previous studies.<sup>14, 48</sup> The capture probes can be strongly immobilized on the MUDA SAM in Ni<sup>2+</sup> buffer (Figure 2.1a), appearing as circular protrusions of  $\sim$ 8 nm diameter under AFM (Figure 2.1e).<sup>36</sup> Importantly, these surface-tethered probes can return to their upright state by removing the Ni<sup>2+</sup> cations with a saline Tris-acetate-EDTA (STAE) buffer, enabling both differential pulse voltammetry (DPV) measurement and target recognition (Figure 2.1b, c). The sensor surface produces a well-resolved DPV peak, whereas in the presence of target DNAs, the peak signal drops (Figure 2.1f, g). We used a target molecule possessing a 19-bp double-stranded segment, a 2-base spacer, and a 19-base single-stranded sticky-end (T1). The double-stranded tail was designed to facilitate AFM identification of the target-probe duplexes that can be distinguished from the free probes based on their conformations. Moreover, the target can to some extent mimic the larger footprints of nucleic acid targets utilized in clinical applications, which are often 150-300 nt in length, *i.e.*, much longer than the DNA capture probes (20-50 nt in length).<sup>7, 34</sup> The radius of gyration of the P1-T1 duplex is about 18 nm, which is analogous to that of a target-probe duplex that contains a 20-bp double-stranded segment and 150-nt single-stranded tail.<sup>7, 49</sup> The AFM images of the surface before and after the addition of targets illustrated distinct molecular



features that correspond to unhybridized hairpin probes (circular protrusions, Figure 2.1e) and P1-T1 duplexes (~20 nm long worm-like protrusions, Figure 2.1h).

We first investigated how the probe densities can be controlled based on the above platform. The Au electrode passivated with MUDA SAM was exposed to solutions of different concentrations (100 nM to 4  $\mu$ M) of thiolated DNA capture probes, as shown in Figure 2.3a (as well as in Figure 2.4a), the probe surface density steadily rises as the concentration of thiolated capture probes is increased from 100 nM to 2.5  $\mu$ M (from left to right panel). When the concentration is 4  $\mu$ M, the resulting immobilized individual probe molecules are difficult to resolve due to severe overlap between the molecular features (Figure 2.4a). Hence only a lower limit,  $2 \times 10^{12}$  probes/cm<sup>2</sup> could be estimated (marked as red dot in Figure 2.3e). As given in Table 2.1, these values cover most of the range of probe surface densities of practical biosensors and microarrays, with the exception of high end at  $10^{12}$ - $10^{13}$  probes/cm<sup>2</sup>.<sup>7, 12</sup> While single molecule AFM imaging can directly quantify the probe densities, we also utilized the unique ability to characterize the spatial arrangements of single probes, which are inaccessible with existing ensemble averaging techniques.<sup>33, 50-51</sup> First, we calculated the Ripley's K function, which can determine the tendency of clustering/dispersing of the probes at different spatial scales.

$$K(r) = \lambda^{-1}E = \lambda^{-1} \sum_i \sum_{j \neq i} w(l_i, l_j)^{-1} \frac{I(d_{i,j} < r)}{N} \quad (2.2)$$

where  $\lambda$  is the number density of the molecules, E is the number of molecules within a radius of r from the molecule of interest, w( $l_i, l_j$ ) the weight function for edge correction, I is the indicator function. For a surface with a completely random spatial pattern,

$$\left[ \frac{K(r)}{\pi} \right]^{\frac{1}{2}} - r = L(r) - r = 0 \quad (2.3)$$

Statistically significant clustering or dispersion can be identified by comparing measured  $L(r) \cdot r$  against Monte Carlo simulated  $L(r) \cdot r$  curves under complete spatial randomness (Figure 2.4b). All  $L(r) \cdot r$  curves, except for those with very low probe densities ( $1.33 \times 10^{10}$  probe/cm<sup>2</sup> and  $2.91 \times 10^{10}$  probe/cm<sup>2</sup>, where fluctuation in  $L(r) \cdot r$  is significant due to sparsity), fall close to the expected value of 0 for all distances up to 150 nm, indicating an overall spatially random distribution of probes (Figure 2.3c and 2.4b). An exception is that for surfaces with medium probe densities ranging from  $5.90 \times 10^{10}$  probe/cm<sup>2</sup> to  $1.04 \times 10^{11}$  probe/cm<sup>2</sup>, the  $L(r) \cdot r$  values dip below the 2.5% quantile of Monte Carlo simulated  $L(r) \cdot r$  values at 10 nm (black curve of Figure 2.3c and red curves of Figure 2.4b). The statistically significant deviation shows the tendency for the probe molecules to be dispersed at this scale. The dispersion may be

rationalized by the repulsive interactions between the molecules during surface immobilization of probes, especially under our low ionic strength (50 mM NaAc). The absence of dispersion at higher probe densities (blue curve in Figure 2.3c) suggests that the repulsive interactions are overcome by a larger driving force to pack the surface with probe molecules. While the Ripley's K function characterizes the tendency for the entire sensor surface to cluster or disperse, a spatial property that likely has a direct effect on target recognition is the nearest neighbor distance (N.N.D.), *i.e.*, the distance between a probe and its closest neighboring probe. We displayed the N.N.D. of each of the probe molecules in the heat map in Figure 2.3b using the spatial coordinates. The range of N.N.D. values is very broad. However, as shown in Ripley's K function (Figure 2.3c), the broad distribution of N.N.D. is a consequence of random distribution instead of clustering of molecules. It should be noted that according to the histograms of N.N.D. (Figure 2.4c), up to 94.4% of the values are below the commonly used average probe separation,  $\langle \text{N.N.D.} \rangle_{\text{Lat}} = (A/n)^{1/2}$ ,<sup>12, 33, 52-53</sup> which is calculated based on the assumption that the molecules are organized in a square lattice, using A, the total surface area, and n, the number of molecules. The discrepancy clearly indicates that the average inter-probe separation is not an adequate descriptor of molecular crowding.

We then examined the correlation between the electrochemical signal and the overall probe density. The peak current increased with increasing DNA probe concentration ranging from 100 nM to 4  $\mu\text{M}$ , as depicted in Figure 2.3d (bottom to top). More importantly, Figure 2.3e illustrates that the peak current scaled linearly with the probe density from  $1.3 \times 10^{10}$  probes/cm<sup>2</sup> to  $1.0 \times 10^{11}$  probes/cm<sup>2</sup>, then began to saturate at  $5.2 \times 10^{11}$  probes/cm<sup>2</sup>. The saturation in peak current and the decline in peak current/probe density ratio indicates that the inter-probe interactions may trigger the unfolding of the stem-loop probe,<sup>54-56</sup> increasing the separation between the redox reporter and the electrode surface and slowing the rate of electron transfer. Alternatively, as the inter-probe separations are decreased, the repulsive interactions between probe molecules led to subtle orientation/conformational changes,<sup>16, 34</sup> separating the redox label from the electrode surface. Notably, while the imaging resolution achieved (a few nm) is not sufficient for differentiating between the folded and unfolded states, the results above nevertheless provide direct evidence that crowding interaction impacts the electrochemical signals.

We next explored the correlation between the hybridization yield and electrochemical signal suppression. Specifically, we measured the signal suppression of a surface with a probe density of  $5.9 \times 10^{10}$  probes/cm<sup>2</sup>, when the target concentration was varied between 10 nM to 1  $\mu\text{M}$  (300 nM and 1  $\mu\text{M}$  in Figure 2.6) at a fixed hybridization time of 30 min. AFM images of the sensor surface were collected as well (Figure 2.5a-d) to directly quantify the overall hybridization yield. Figure 2.5e shows that the fraction of hybridized probes, *i.e.*, hybridization yield, increases with the increasing target concentration and

reaches a plateau of 88% at 100 nM (red curve). The trend tracks the curve of the DPV signal suppression (blue curve). The gap between the hybridization yield curve and signal suppression curve is consistent with the observation that some of the probe/target duplexes have sufficient conformational freedom to tilt toward the surface for facile electron transfer, resulting in incomplete signal suppression.<sup>12</sup> In addition, while from electrochemical measurement alone, it is not clear whether the incomplete signal suppression is caused by the finite electron transfer rate or incomplete hybridization,<sup>14</sup> single molecule AFM analysis provides direct evidence that a small fraction (~10%) of the probe molecules are inactive because no further improvement in hybridization yield was observed even at higher target concentrations of 300 nM and 1  $\mu$ M (Figure 2.5e and 2.6). An incomplete hybridization was also observed for hybridization in a homogeneous solution.<sup>57</sup> The origin is not yet clear. Commercial synthetic oligonucleotides typically contain 10-15% impurities that are missing one or more nucleotides,<sup>58</sup> because the yield of each of the solid phase coupling reaction steps is below 100%. Therefore, it is possible that these truncated oligonucleotides may account for the less than unity hybridization yield. In addition to concentration dependence, the hybridization yield was measured at different time intervals at a fixed target concentration of 100 nM. The hybridization yield increased over time and saturated after 30 minutes (Figure 2.7a). The same trend was observed in the corresponding time evolution of DPV suppression (Figure 2.7b).

In addition to calibration-free, quantitative measurement of the overall hybridization yield, high resolution AFM imaging affords the unique opportunity to characterize the spatial patterns of surface hybridization. Interestingly, we found that the probe-target duplexes tend to form clusters and the number of clusters rises with increasing target concentrations (Figure 2.5a-d, highlighted by green circles). To develop a more quantitative description, we analyzed the spatial organization of these duplexes using the Ripley's K function. The positive values in Figure 2.5f show that the duplexes are clustered. The values approach zero with increasing target concentrations, presumably due to the merging of clusters ( $L(r) - r$  curves for 300 nM and 1  $\mu$ M targets are shown in Figure 2.6c).<sup>41</sup>

The emergence of a heterogeneous spatial pattern of hybridization from a mostly random spatial distribution of probe molecules is rather surprising as molecular crowding is conventionally thought to hinder interfacial target recognition. The spatial organization suggests target binding is instead a cooperative process. To gain more mechanistic insights, we relocated the same areas of the biosensor surface ( $5.9 \times 10^{10}$  probes/cm<sup>2</sup>) to monitor the evolution of the spatial patterns (Figure 2.8a-c). This experiment can provide definitive information on how probe spatial arrangement impacts the cluster distribution and the pathway of cluster formation. The areas in green squares zoomed in the insets of Figure 2.8a-c illustrate that the cluster began to emerge at 45 min

and evolved into a complete cluster at 105 min at 10 nM target concentration. The nearest-neighbor distances (N.N.D.) map in Figure 2.8d showed that the captured target molecules predominantly appeared in the regions where the N.N.D. are less than or equal to 15 nm (red or orange dots). The histograms in Figure 2.9a and 2.9c further confirm that the hybridization of the probes is highly sensitive to N.N.D.. The fraction of hybridized probes with N.N.D. of 10 nm is close to 50%, while only 5% of the probes with N.N.D. of 25 nm are hybridized. These results provide direct evidence that under certain circumstance, the molecular crowding between the molecules may enhance instead of hindering surface hybridization. In addition, we also employed the local crowding index  $LCI(r)$ , a parameter we introduced in a previous work,<sup>18</sup> to explore if molecules that are located beyond nearest-neighbors also affect hybridization.  $LCI(r)$  counts the number of neighboring probes surrounding a specific probe, within an interaction radius  $r$  (20 nm which is about twice the length of probe P1 is used here). A measure of the local probe density at a specific spatial scale,  $LCI(r)$  allows us to assess the degree of local crowding experienced by individual probes, which can then be correlated to their hybridization efficiency. Compared to N.N.D., which serves an indicator of the “two-body” interactions between the probe of interest and its nearest neighbor,  $LCI(r)$  enables us to evaluate our system from “many-body” perspective of neighboring probe molecules. The  $LCI(20\text{ nm})$  versus N.N.D. plots at 45 min and 105 min (Figure 2.9b, d) show that the probability of hybridized probe molecules (red dots) increases at the top. For probe molecules with the same N.N.D., those with higher LCIs are more likely to hybridize. Overall, Figure 2.9 demonstrates that the presence of neighboring molecules (~15 nm) may accelerate the hybridization rate of the hairpin probes by an order of magnitude or more. In addition, probe molecules that are located beyond the nearest-neighbors can also impose molecular crowding that accelerate hybridization.

To confirm that the observed enhancement in hybridization is a consequence of the local crowding of probe molecules, one possibility we need to rule out is that clustered probe molecules may coincide with disordered SAM domains that may facilitate hybridization through nonspecific adsorption on a more hydrophobic surface.<sup>27</sup> A previous study suggested that hydrophobic surfaces increase the residence time of the DNA targets and thus accelerate the hybridization rate.<sup>59</sup> The absence of target molecules on the MUDA SAM without capture probes shows that only targets binding to the captured probes can remain on the surface and non-specific binding of targets on SAM domains is weak (Figure 2.10). Moreover, we replaced the stem-loop probe P1 with a linear probe P2 (Figure 2.11). Interestingly, although the probe surface density and spatial organization of immobilized P2 molecules (Figure 2.11b, c) are similar to those of P1 (Figure 2.8d and 2.12), the spatial pattern of P2-T1 duplexes is substantially different (Figure 2.11d, e). The clustering function

indicates a random spatial pattern of P2-T1 duplexes (Figure 2.11f). The absence of target clustering on surfaces with P2 indicates that nonspecific binding of targets on local SAM domains is not responsible for clustering of target-probe duplexes. The lack of clustered target molecules also exclude the possibility that the aggregation of target molecules in free solution is responsible for the clustering of captured targets with the stem-loop probe P1. Another piece of supporting evidence is that clustering of captured targets is observed at target concentrations as low as 10 nM in a monovalent cation  $\text{Na}^+$  buffer. Dynamic light scattering (DLS) measurements of the target solutions used for hybridization showed that there is no aggregation (Figure 2.13). Consistent with previous studies, aggregation of DNAs in a monovalent buffer solution only forms at higher concentrations ( $\mu\text{M}$  or more).<sup>60-62</sup> Therefore, we conclude that the clustering is caused by a combination of the secondary structure of the probe and a higher local probe density. Furthermore, we carried out a hybridization experiment that used P1 to capture T2, which is a shorter, 19-base single-stranded counterpart of T1. Ripley's K function analysis also revealed a random spatial pattern of the P1-T2 duplexes under the same experimental conditions, including probe surface density, and target concentration (Figure 2.14).

Two distinct characteristics of the surface-tethered probes can be responsible for the observed spatial heterogeneity. First, the molecular crowding is more important for surface-tethered probe molecules than for probes in free solution. In contrast to the average inter-probe separation on a biosensor surface ranging between a few nanometers and tens of nanometers, the average inter-probe distance in a homogeneous solution is typically 100 nm or more, as the typical probe concentration is less than micromolar. Second, although the hybridized and unhybridized probes undergo free Brownian diffusion in solution hybridization, the surface immobilized probes maintain their positions relative to the biosensor surface. Therefore, the inter-probe interactions between neighboring molecules in a dilute solution are short-lived. In contrast, the spatial heterogeneity of surface-tethered probes is persistent (Figure 2.8a-c) and hence can impact hybridization kinetics as well as binding affinity substantially.

Our study provides the first single molecule level evidence that the spatial proximity of capture probes has a major influence on surface hybridization. However, our findings are a departure from the prevailing assumption that crowding interaction inhibits target binding and optimal hybridization kinetics is achieved at the lowest densities.<sup>10-12, 16, 26, 33</sup> This discrepancy may be attributed to two factors. First, it has not been possible to quantify the influences of specific inter-probe separations, as existing studies measured the overall target binding kinetics of surfaces that have highly heterogeneous inter-probe distances.<sup>18, 20, 63</sup> Our single molecule resolution of hybridization offers a straightforward way to fill the knowledge gap. Second, many existing

studies focus on high surface density regimes,  $10^{12}$  probes/cm<sup>2</sup> or greater,<sup>11, 26, 33</sup> where the accessibility to probe molecules may indeed be the limiting factor. Our study focuses on a less crowded regime ( $\sim 10^{11}$  probes/cm<sup>2</sup>), where accessibility is less an issue and enhancement mechanisms may manifest themselves. The use of less perturbing imaging modes, such as noncontact AFM,<sup>64</sup> may allow AFM to study the single molecule spatial arrangements at higher probe densities, when the probes are separated by less than a few nanometers, where limited accessibility to the probe molecules may begin to hinder target recognition.

The unexpected cooperative effect may be rationalized by exploring the microscopic mechanisms of DNA hybridization. The hybridization of a DNA stem-loop probe is thought to proceed via a nucleation step that forms a stable contact between the loop and the target molecule, followed by the melting of the stem, and propagation of the base paired region to form a full probe-target duplex (zippering).<sup>65</sup> While the rate limiting step for hybridization of unstructured probes is the formation of stable target-probe contacts, that for hybridization of stem-loop probes may be stem melting.<sup>50, 65</sup> When the probe molecules are separated by 10-15 nm, there is sufficient space for a target to form contacts with a probe. Based on the data either directly from this work or the literature,<sup>66</sup> we propose three mechanisms including (i) probe crowding, (ii) target crowding and (iii) crowding-induced surface trapping that may accelerate target binding at these inter-probe separations. First, these probe molecules may impose a repulsive potential that causes the destabilization of the hairpin structure of neighboring probe molecules and facilitates target capture.<sup>12</sup> Supporting evidence of this mechanism includes Figure 2.9 as well as the absence of clustering of target-probe duplexes using linear probes, P2 (Figure 2.11d-f). In addition, the sublinear relationship between the electrochemical signal and the probe density when the probe density exceeds  $1 \times 10^{11}$  /cm<sup>2</sup> (Figure 2.3e) also reveals that probe crowding interaction favors the unfolded state. Unfolding of closely packed DNA hairpin probes was also observed in previous studies.<sup>54-55</sup> While the probe density studied,  $5.9 \times 10^{10}$ /cm<sup>2</sup>, appears too low to cause a significant fraction of them to unfold, our spatial statistics shows that 20% of the probe molecules have N.N.D. of 10 nm or less (Figure 2.12) due to the random nature of spatial arrangement. Notably, zippering does not necessarily need to be preceded by complete unfolding.<sup>66</sup> Even a modest destabilization of the stem-loop may lower the activation energy barrier of concomitant stem melting and formation of target-probe duplex and accelerate the hybridization kinetics. The second mechanism is the destabilization of the stem by binding of target molecules to nearby hairpins. A probe-target duplex increases electrostatic repulsion within a hemisphere, owing to its ability to rotate around its tethering point; the localized increase of electrostatic repulsion may also favor unfolding of neighboring stem-loop probes and accelerate target binding in close proximity. This target crowding is supported

by the more facile hybridization of T1 compared to that of the shorter target, T2 (Figure 2.14). Notably, this target crowding-induced cooperative effect is likely relevant, as many nucleic acid targets for molecular diagnostics are notably longer than the capture probes (P1) used in this work.<sup>7, 34</sup> The third enhancement mechanism is that probe molecules in proximity can trap the target molecules and increase their residence time. The formation of a full duplex is typically preceded by many unproductive contacts between the target and the hairpin loop.<sup>66</sup> A target molecule that is transiently bound may have a greater opportunity to hop onto a neighboring probe molecule and get captured. So far, no single mechanism could explain all the findings. While there is definitive evidence supporting the first two mechanisms, probe crowding and target crowding, we cannot rule out the possibility that the third mechanism also aids the enhancement. Future studies that systematically investigate the effects of target size, probe density and probe design can identify the relative contributions of the proposed mechanisms.

## 2.4. Conclusion and outlook

Spatially resolved measurement of molecular recognition of an E-DNA sensor revealed novel complex, heterogeneous behaviors that are difficult to capture using conventional ensemble averaging techniques. Even when the probe density is relatively uniform, the wide distribution of inter-probe separations arising from random probe immobilization may lead to heterogeneous target hybridization. Therefore, the probe density alone may not be an adequate descriptor of interfacial molecular recognition, given the observed major impact of inter-probe distances on target hybridization. These findings set the stage for future studies that can explore how these probe spatial patterns help determine the sensitivity and device to device variabilities of existing electrochemical biosensors.<sup>6, 20-22</sup> Moreover, the detailed mechanisms of enhancement and the impact of molecular crowding interactions still remain unclear. Ultimately, the mechanistic insights from spatially resolved measurements and single molecule spatial statistics may help build a predictive relationship between molecular scale spatial organizations and the biosensing performance, paving the way to rationally engineer biosensor devices.

**Table 2.1.** Summary of experimentally measured probe densities.

probe DNA concentration(nM)	probe density (probes/cm <sup>2</sup> )
100	$1.33 \times 10^{10}$
250	$2.91 \times 10^{10}$
500	$5.90 \times 10^{10}$
750	$6.46 \times 10^{10}$
1000	$7.90 \times 10^{10}$
1500	$1.04 \times 10^{11}$
2000	$5.24 \times 10^{11}$
2500	$8.06 \times 10^{11}$
4000	$\sim 2.00 \times 10^{12}$



**Table 2.2.** Summary of probe and target sequences. Abbreviations used: NH<sub>2</sub> = amide; MB = methylene blue; SS =disulfide.

Name	DNA Sequence & Modifications
P1	5'-SS-(CH <sub>2</sub> ) <sub>11</sub> -CGGTCCGGTGGAATGAAGGACCG-NH <sub>2</sub> -MB-3'
P2	5'-SS-(CH <sub>2</sub> ) <sub>11</sub> -TTTTCCGGTGGAATGAAGGACCA-3'
T1	5'-AAAGGGATGGGTAGGGAGGCCTCCCTACCCATCCCTTTTT GGTCCTTCATTCCACCGGA-3'
T2	5'-GGTCCTTCATTCCACCGGA-3'

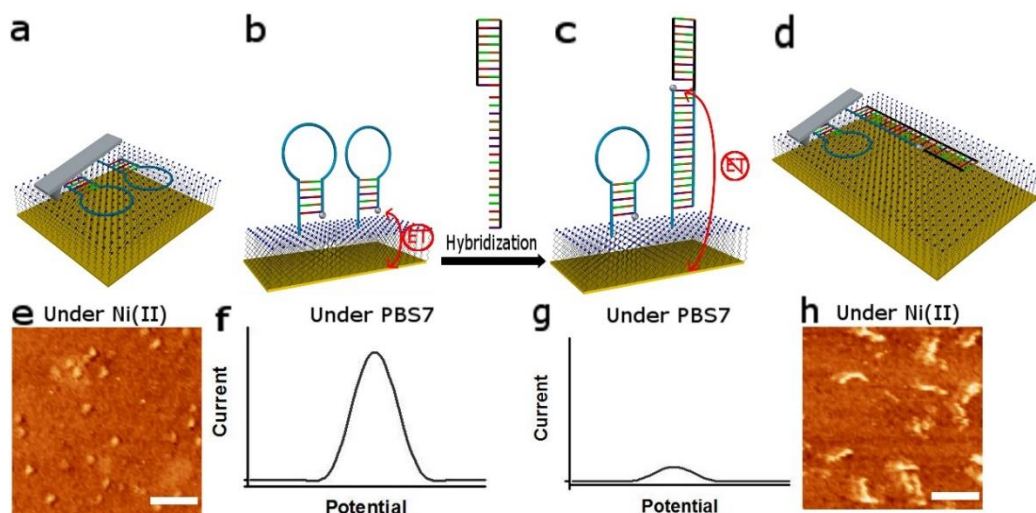


**Figure 2.1.** Schematic of a dynamically switchable E-DNA sensor surface. (a) A stem-loop DNA probe is covalently tethered at one end to a single-crystal Au electrode passivated with a MUDA monolayer and modified with a MB tag (Silver) at the other end. The probe is pinned down to the surface after adding  $\text{Ni}^{2+}$  and thus can be imaged by AFM. (b) After imaging, the surface is rinsed with an STAE buffer and a DPV measurement is carried out under a PBS7 buffer. (c) Upon the addition of a complementary target DNA into the PBS7 buffer, the same DPV measurement is repeated. (d) The hybridized surface is imaged following the same procedure as given in step (a) above. AFM images and DPV signals of the sensor surface (e,f) before and (h,g) after the hybridization with the targets. The scale bar is 25 nm.

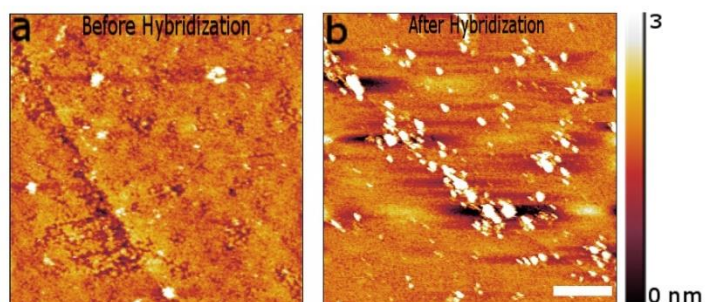


**Figure 2.2.** Representative AFM images of the sensor surface prepared using the backfilling method before (a) and after (b) exposure to 100 nM target (T1). The surfaces were imaged with AFM in the imaging buffer (5 mM  $\text{Ni}^{2+}$  in  $0.1\times$  TAE). The probes (except aggregations) were difficult to resolve because of the poor SAM quality prior to hybridization with the targets. Severe aggregations between hybridized probes were formed after hybridization. Scale bar is 100 nm.

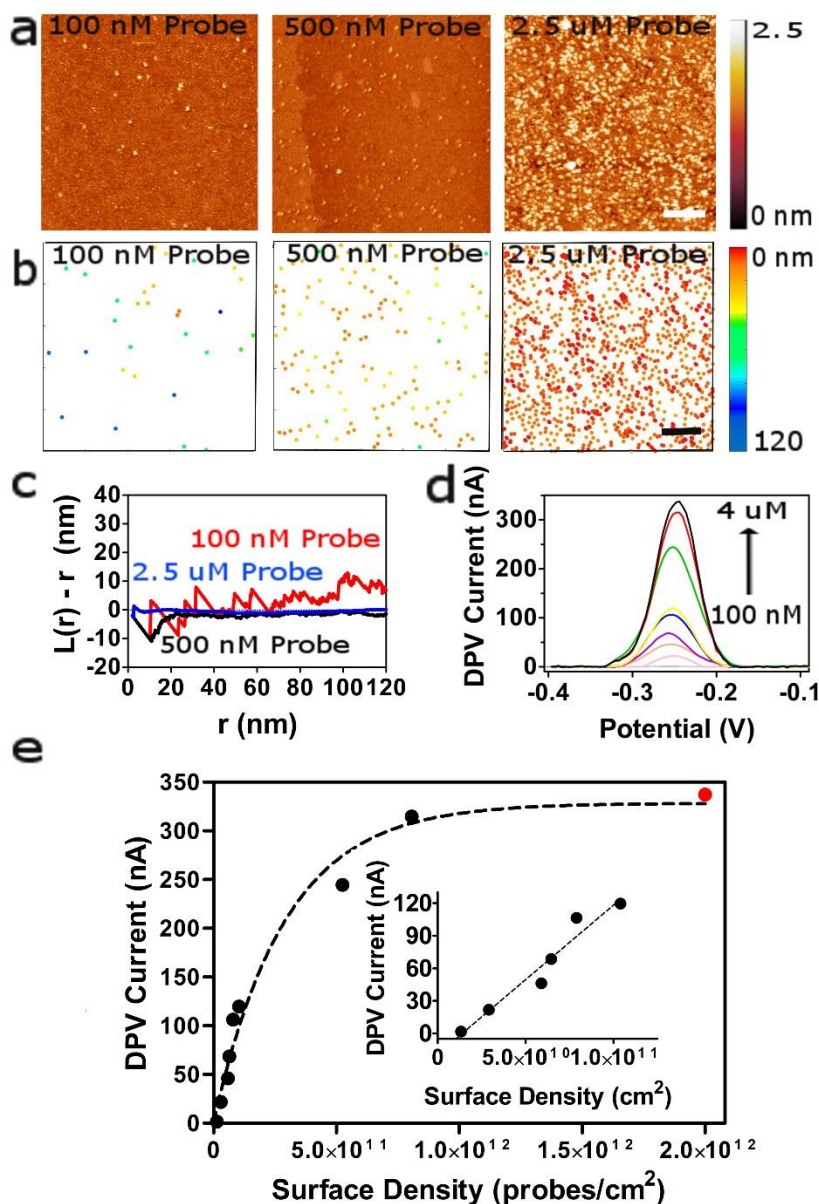


**Figure 2.3.** Correlating probe density and DPV of the E-DNA sensor surface. (a) Representative AFM images of the sensor surface fabricated using DNA probe concentrations at 100 nM, 500 nM and 2.5 μM. The insertion time is fixed at 30 min. The scale bar is 100 nm. (b) The nearest-neighbor distance (N.N.D.) analysis of probes in panel (a). The color bar indicates the range of N.N.D. from 0 nm (red) to 120 nm (blue). (c) The Ripley's K-function analysis of the distribution of probes. (d) The corresponding DPV voltammograms (from bottom to top). (e) The relation between probe surface density and peak current. Inset, the current peak of E-DNA sensor is linearly related to the probe surface density at low probe densities (< 10<sup>11</sup> probes/cm<sup>2</sup>). Red dot represents the estimated probe density.

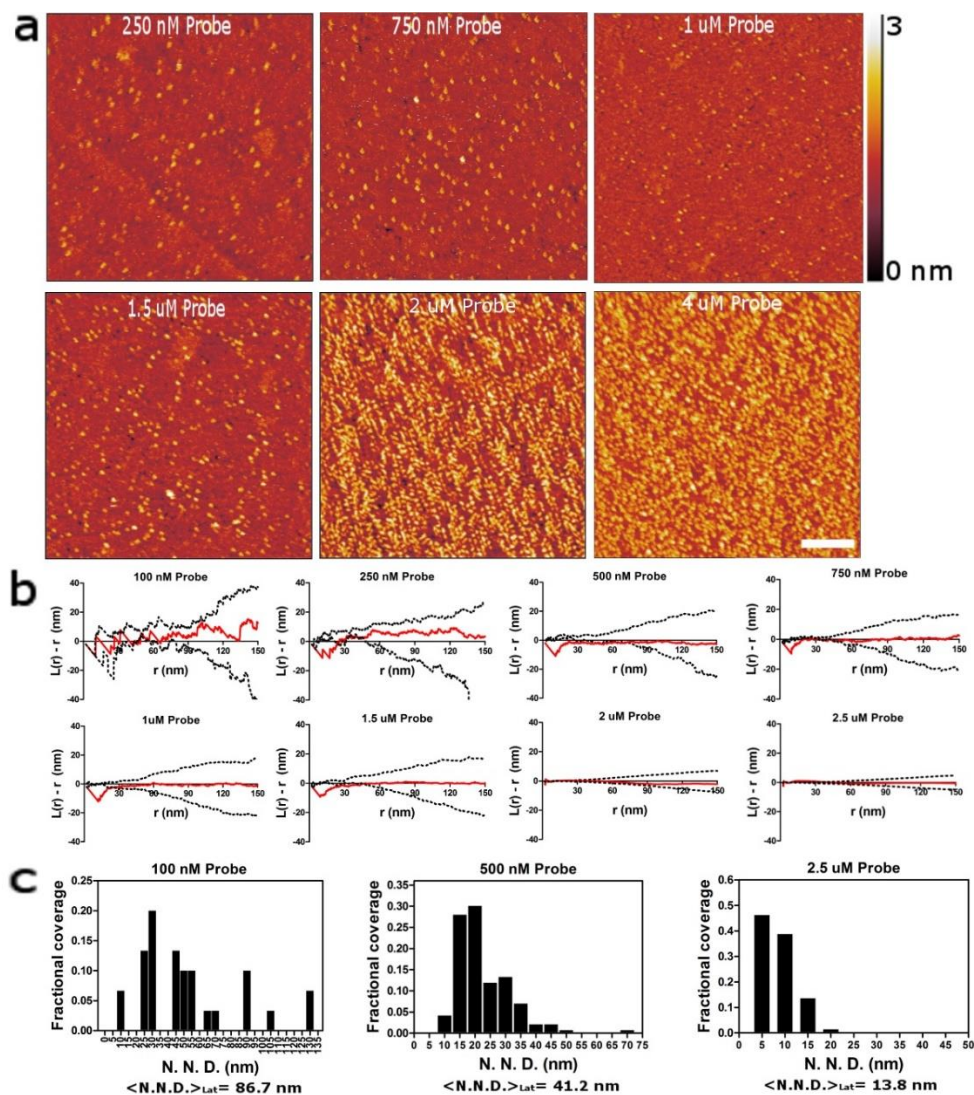


**Figure 2.4.** (a) Representative AFM images of the sensor surfaces immobilized with different concentration of P1 probes, 250 nM, 750 nM, 1  $\mu$ M, 1.5  $\mu$ M, 2  $\mu$ M, and 4  $\mu$ M. The insertion time is fixed at 30 min. The scale bar is 100 nm. (b)  $L(r) - r$  curves for probe distributions on sensor surfaces prepared using probe concentrations of 100 nM, 250 nM, 500 nM, 750 nM, 1  $\mu$ M, 1.5  $\mu$ M, 2  $\mu$ M, and 2.5  $\mu$ M. Dashed lines are the 0.025 and 0.975 quantiles of  $L(r) - r$  estimated from 999 simulations. (c) The histograms of N.N.D. for sensor surfaces prepared with 100 nM, 500 nM and 2.5  $\mu$ M DNA probes, and below each are the calculated average probe separations.

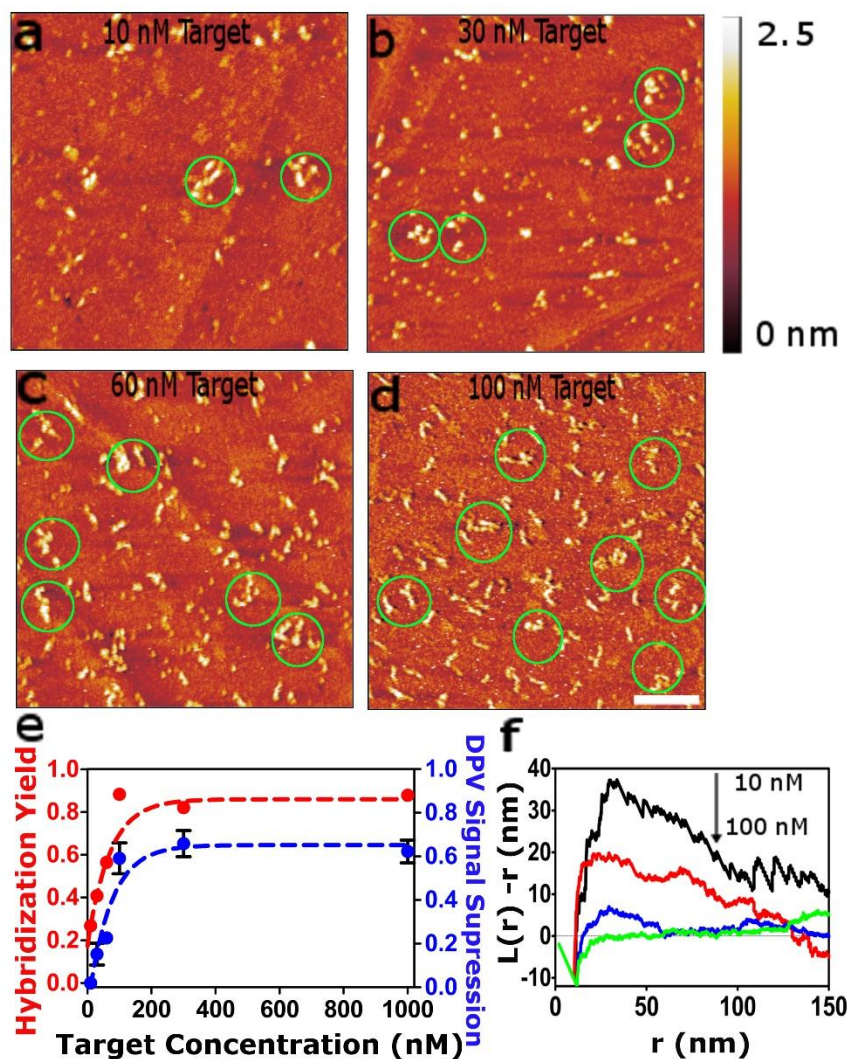


**Figure 2.5.** Spatial patterns of surface hybridization. (a-d) Representative AFM images of the sensor surface in the presence of complementary T1 target DNAs at 10 nM, 30 nM, 60 nM and 100 nM. The green dotted circles are used to outline the clusters. The hybridization time is fixed at 30 min. The scale bar is 100 nm. (e) The relation between hybridization yield (red curve) and DPV signal suppression (blue curve) at different target concentrations. (f) The Ripley's K-function analysis of the distribution of hybridized probes. The  $L(r) - r$  curve shows a decrease of clustering with increasing target concentration (from top to bottom).

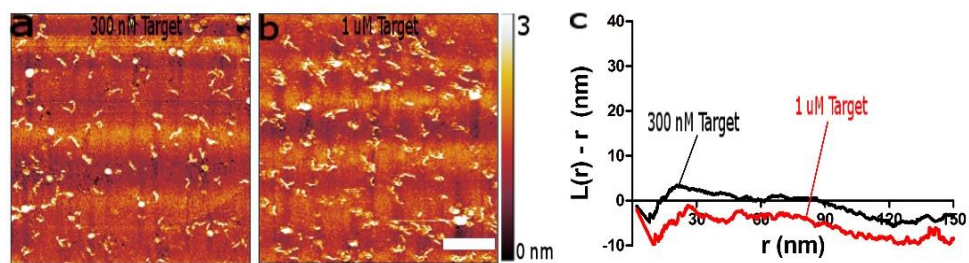


**Figure 2.6.** Representative AFM images of the sensor surfaces incubated with (a) 300 nM and (b) 1 μM T1 targets for 30 min and (c) the corresponding  $L(r) - r$  curves. Scales bars are 100 nm.

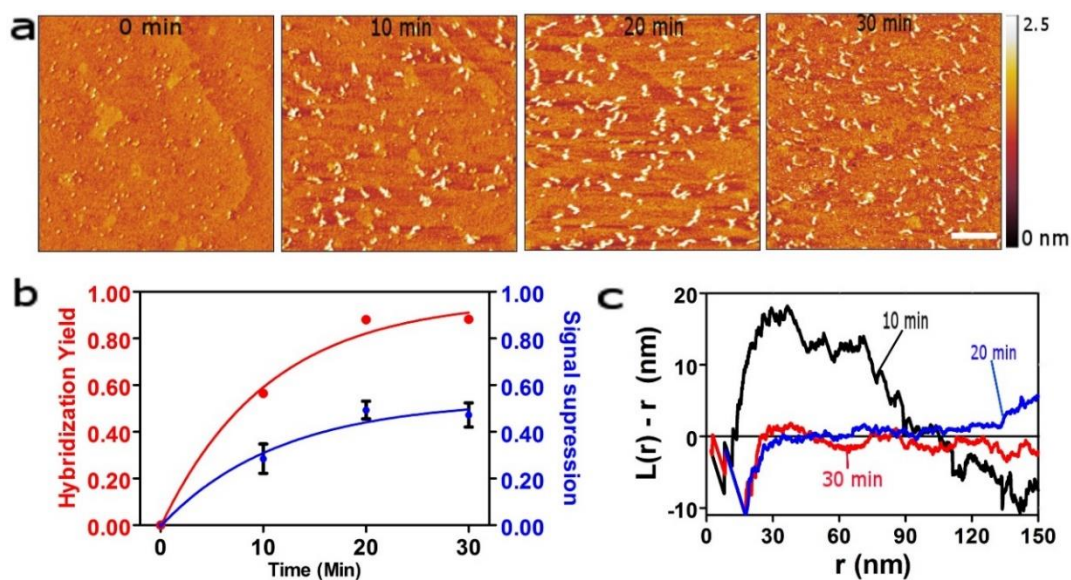


**Figure 2.7.** Evolution of spatial patterns of hybridized probes. (a) Representative AFM images of the sensor surface in the presence of 100 nM T1 after exposure times of 0 min, 10 min, 20 min and 30 min. The scale bar is 100 nm. (b) Hybridization yield and DPV signal suppression at different time points. (c) The Ripley's K-function analysis of the spatial distribution of hybridized probes. The  $L(r) - r$  curve shows a decrease of clustering over time (from top to bottom).



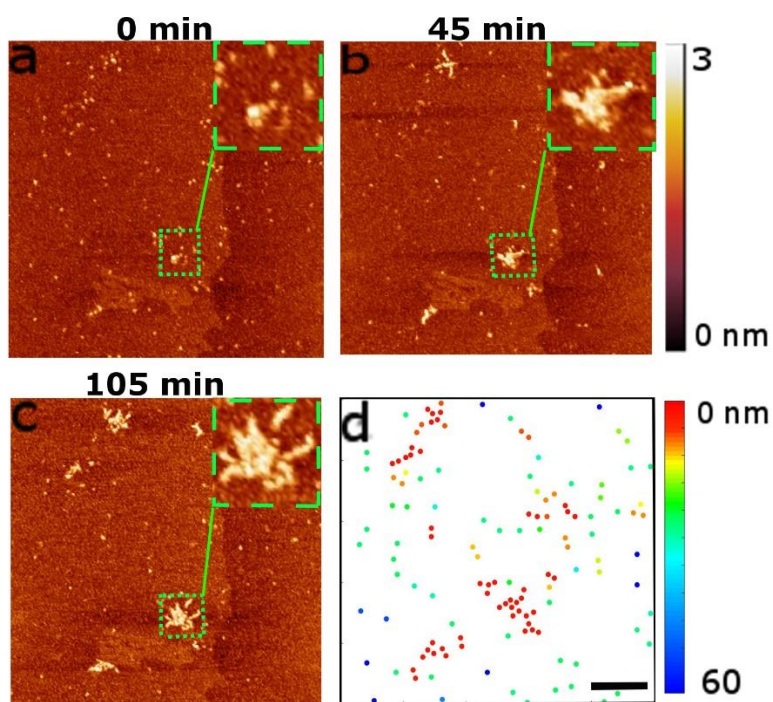


**Figure 2.8.** Tracking evolution of heterogeneous spatial patterns of DNA surface hybridization. Representative AFM images of the sensor surface after exposed to 10 nM target DNA for (a) 0 min, (b) 45 min and (c) 105 min. The scale bar is 100 nm. Insets are zoom in images of green-squared areas. (d) The nearest-neighbor distance (N.N.D.) analysis of unhybridized probes in panel (a). The color bar indicates the range of N.N.D. from 10 nm (red) to 60 nm (blue).

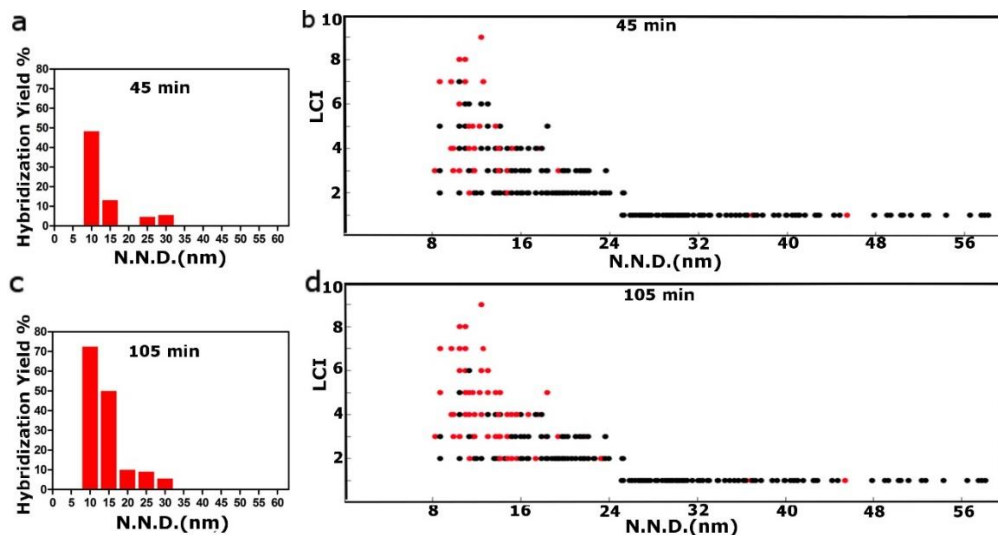


**Figure 2.9.** Spatial statistical analysis of probe distributions. (a), (c) The histograms of the hybridization yield at 45 min and 105 min as a function of N.N.D.. (b), (d) Plots of LCI vs. N.N.D. at 45 min and 105 min for each DNA probe. Probes with high LCI and low N.N.D. are more likely to capture targets. The red dots represent hybridized probes, while the black dots represent unhybridized probes.

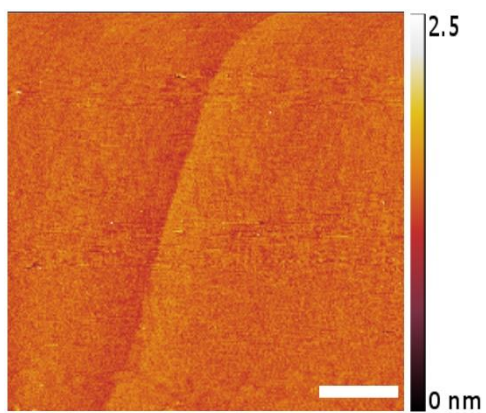


**Figure 2.10.** Representative AFM image of the MUDA SAM surface (without probes) incubated with 100 nM large targets (T1) for 30 minutes. The absence of targets indicates that the non-specific adsorption is minimized. Scale bar is 100 nm.

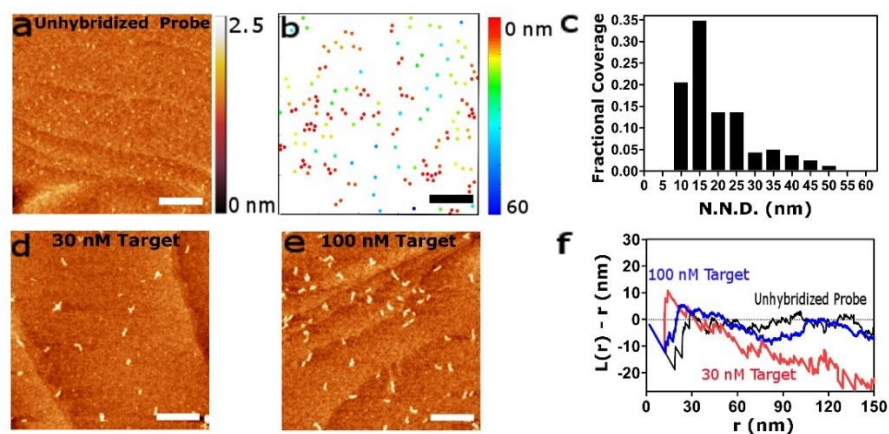


**Figure 2.11.** Control experiment using linear probes. Representative AFM images of the linear probe surface in the absence (a) and presence of complementary target DNAs at 30 nM (d) and 100 nM (e). The hybridization time is fixed at 15 min. The scale bar is 100 nm. (b) The nearest-neighbor distance (N.N.D.) analysis of unhybridized probes in panel (a). The color bar indicates the range of N.N.D from 10 nm (red) to 60 nm (blue). Histograms of unhybridized probes in panel (a) as a function of N.N.D.. (f) The Ripley's K-function analysis of the distribution of hybridized probes. The  $L(r) - r$  curves show uniform distributions of unhybridized probes (black) and hybridized probes at 100 nM (blue), and a relatively dispersed distribution of hybridized probes at 30 nM (red).

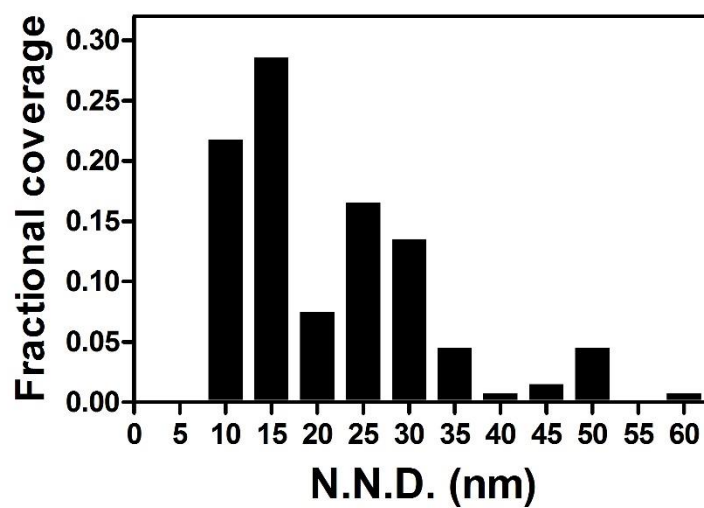


**Figure 2.12.** N.N.D. distribution histogram for unhybridized probes (P1) at 0 min in Figure 2.8a.

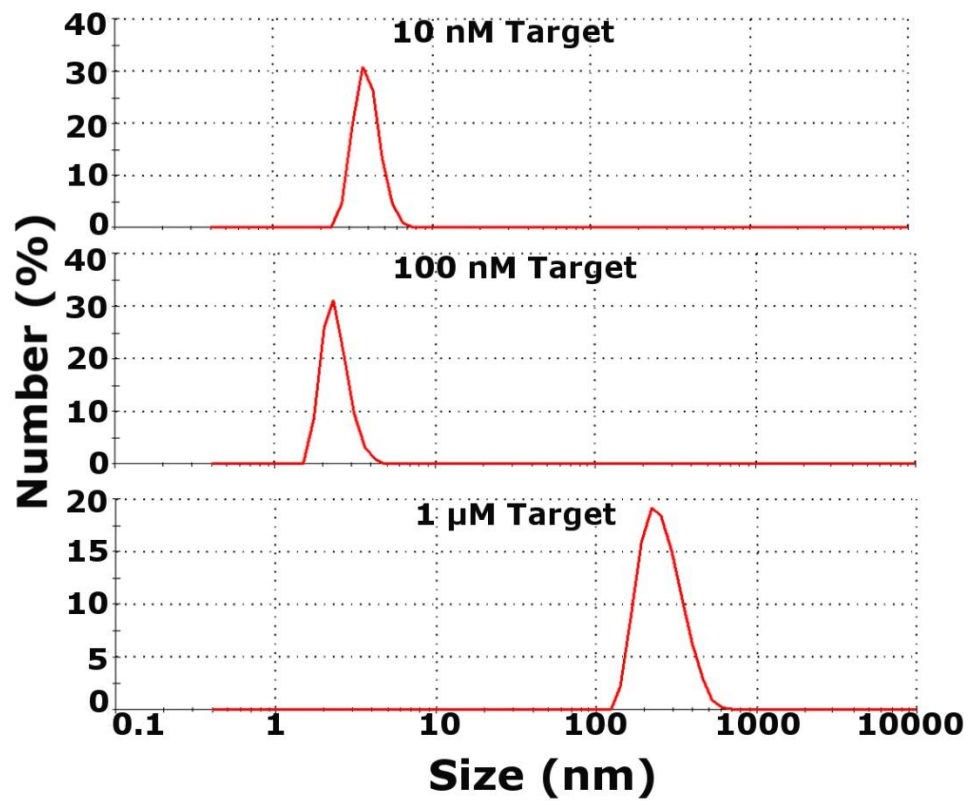


**Figure 2.13.** DLS study of the size distribution of T1 target molecules at the concentrations of 10 nM, 100 nM and 1 μM in PBS7.

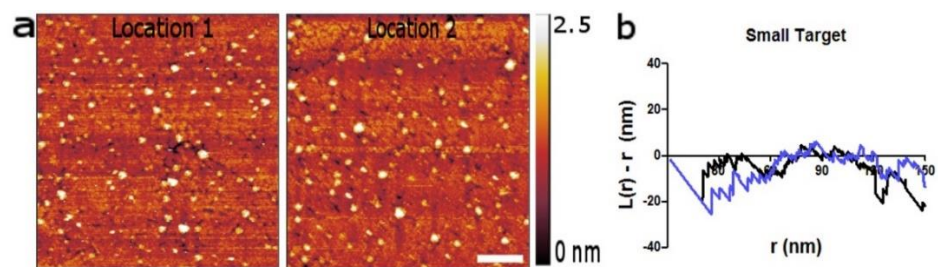


**Figure 2.14.** Representative AFM images of the P1 immobilized surfaces incubated with small targets (T2) and the corresponding  $L(r) - r$  curves. Scale bar is 100 nm.

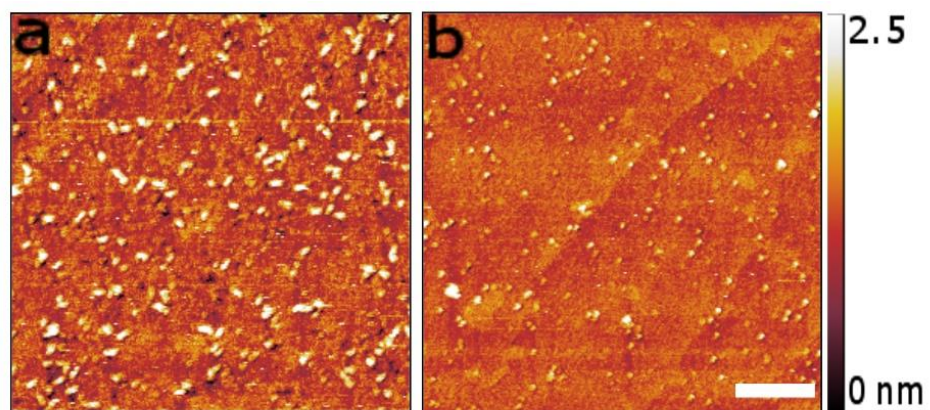


**Figure 2.15.** Representative AFM images of the sensor surface before (a) and after (b) denaturation. Scale bar is 100 nm.



## References

1. Drummond, T. G.; Hill, M. G.; Barton, J. K., Electrochemical DNA Sensors. *Nature Biotechnology* **2003**, *21* (10), 1192-1199.
2. Smith, S. J.; Nemr, C. R.; Kelley, S. O., Chemistry-Driven Approaches for Ultrasensitive Nucleic Acid Detection. *J. Am. Chem.Soc.* **2017**, *139* (3), 1020-1028.
3. Arroyo-Curras, N.; Somerson, J.; Vieira, P. A.; Ploense, K. L.; Kippin, T. E.; Plaxco, K. W., Real-Time Measurement of Small Molecules Directly in Awake, Ambulatory Animals. *Proc. Natl. Acad. Sci. USA.* **2017**, *114* (4), 645-650.
4. Kelley, S. O.; Mirkin, C. A.; Walt, D. R.; Ismagilov, R. F.; Toner, M.; Sargent, E. H., Advancing the Speed, Sensitivity and Accuracy of Biomolecular Detection Using Multi-Length-Scale Engineering. *Nat. Nanotechnol.* **2014**, *9* (12), 969-980.
5. Liu, B. W.; Sun, Z. Y.; Huang, P. J. J.; Liu, J. W., Hydrogen Peroxide Displacing DNA from Nanoceria: Mechanism and Detection of Glucose in Serum. *J. Am. Chem. Soc.* **2015**, *137*(3), 1290-1295.
6. Bizzotto, D.; Burgess, I. J.; Doneux, T.; Sagara, T.; Yu, H. Z., Beyond Simple Cartoons: Challenges in Characterizing Electrochemical Biosensor Interfaces. *ACS Sensors* **2018**, *3*(1), 5-12.
7. Rao, A. N.; Grainger, D. W., Biophysical Properties of Nucleic Acids at Surfaces Relevant to Microarray Performance. *Biomaterials Science* **2014**, *2* (4), 436-471.
8. Liu, Y. T.; Irving, D.; Qiao, W. Q.; Ge, D. B.; Levicky, R., Kinetic Mechanisms in Morpholino-DNA Surface Hybridization. *J. Am. Chem. Soc.* **2011**, *133* (30), 11588-11596.
9. Giljohann, D. A.; Seferos, D. S.; Patel, P. C.; Millstone, J. E.; Rosi, N. L.; Mirkin, C. A., Oligonucleotide Loading Determines Cellular Uptake of DNA-Modified Gold Nanoparticles. *Nano Lett.* **2007**, *7*(12), 3818-3821.
10. Herne, T. M.; Tarlov, M. J., Characterization of DNA Probes Immobilized on Gold Surfaces. *J. Am. Chem. Soc.* **1997**, *119*(38), 8916-8920.
11. Peterson, A. W.; Heaton, R. J.; Georgiadis, R. M., The Effect of Surface Probe Density on DNA Hybridization. *Nucleic Acids Res.* **2001**, *29* (24), 5163-5168.
12. Ricci, F.; Lai, R. Y.; Heeger, A. J.; Plaxco, K. W.; Sumner, J. J., Effect of Molecular Crowding on the Response of an Electrochemical DNA Sensor. *Langmuir* **2007**, *23* (12), 6827-6834.

13. Kuralay, F.; Campuzano, S.; Wang, J., Greatly Extended Storage Stability of Electrochemical DNA Biosensors Using Ternary Thiolated Self-Assembled Monolayers. *Talanta* **2012**, *99*, 155-160.
14. Ricci, F.; Zari, N.; Caprio, F.; Recine, S.; Amine, A.; Moscone, D.; Palleschi, G.; Plaxco, K. W., Surface Chemistry Effects on the Performance of an Electrochemical DNA Sensor. *Bioelectrochemistry* **2009**, *76*(1-2), 208-213.
15. Soleymani, L.; Fang, Z. C.; Sargent, E. H.; Kelley, S. O., Programming the Detection Limits of Biosensors through Controlled Nanostructuring. *Nat. Nanotechnol.* **2009**, *4*(12), 844-848.
16. Morrin, G. M.; Schwartz, D. K., Three Regimes of Polymer Surface Dynamics under Crowded Conditions *Macromolecules* **2018**, *51* (3), 1207-1214.
17. Pei, H.; Lu, N.; Wen, Y. L.; Song, S. P.; Liu, Y.; Yan, H.; Fan, C. H., A DNA Nanostructure-Based Biomolecular Probe Carrier Platform for Electrochemical Biosensing. *Adv. Mater.* **2010**, *22*(42), 4754+.
18. Josephs, E. A.; Ye, T., Nanoscale Spatial Distribution of Thiolated DNA on Model Nucleic Acid Sensor Surfaces. *ACS Nano* **2013**, *7*(4), 3653-3660.
19. Cao, H. H.; Nakatsuka, N.; Serino, A. C.; Liao, W. S.; Cheunkar, S.; Yang, H. Y.; Weiss, P. S.; Andrews, A. M., Controlled DNA Patterning by Chemical Lift-Off Lithography: Matrix Matters. *ACS Nano* **2015**, *9*(11), 11439-11454.
20. Du, H.; Disney, M. D.; Miller, B. L.; Krauss, T. D., Hybridization-Based Unquenching of DNA Hairpins on Au Surfaces: Prototypical "Molecular Beacon" Biosensors. *J. Am. Chem. Soc.* **2003**, *125*(14), 4012-4013.
21. Li, H.; Dauphin-Ducharme, P.; Ortega, G.; Plaxco, K. W., Calibration-Free Electrochemical Biosensors Supporting Accurate Molecular Measurements Directly in Undiluted Whole Blood. *J. Am. Chem. Soc.* **2017**, *139*(32), 11207-11213.
22. Yang, L.; Zhang, C. H.; Jiang, H.; Li, G. J.; Wang, J. H.; Wang, E. K., Insertion Approach: Bolstering the Reproducibility of Electrochemical Signal Amplification Via DNA Superstructures. *Anal. Chem.* **2014**, *86*(10), 4657-4662.
23. Macazo, F. C.; Karpel, R. L.; White, R. J., Monitoring Cooperative Binding Using Electrochemical DNA-Based Sensors. *Langmuir* **2015**, *31* (2), 868-875.
24. Wang, S.; Zhang, L. Q.; Wan, S.; Cansiz, S.; Cui, C.; Liu, Y.; Cai, R.; Hong, C. Y.; Teng, I. T.; Shi, M. L.; Wu, Y.; Dong, Y. Y.; Tan, W. H., Aptasensor with Expanded Nucleotide Using DNA Nanotetrahedra for Electrochemical Detection of Cancerous Exosomes. *ACS Nano* **2017**, *11* (4), 3943-3949.
25. Wen, Y. L.; Pei, H.; Wan, Y.; Su, Y.; Huang, Q.; Song, S. P.; Fan, C. H., DNA Nanostructure-Decorated Surfaces for Enhanced Aptamer-Target

- Binding and Electrochemical Cocaine Sensors. *Anal. Chem.* **2011**, *83* (19), 7418-7423.
26. Mirmomtaz, E.; Castronovo, M.; Grunwald, C.; Bano, F.; Scaini, D.; Ensafi, A. A.; Scoles, G.; Casalis, L., Quantitative Study of the Effect of Coverage on the Hybridization Efficiency of Surface-Bound DNA Nanostructures. *Nano Lett.* **2008**, *8*(12), 4134-4139.
27. Monserud, J. H.; Schwartz, D. K., Mechanisms of Surface-Mediated DNA Hybridization. *ACS Nano* **2014**, *8* (5), 4488-4499.
28. Cutler, J. I.; Auyeung, E.; Mirkin, C. A., Spherical Nucleic Acids. *J. Am. Chem. Soc.* **2012**, *134* (3), 1376-1391.
29. Peterson, E. M.; Manhart, M. W.; Harris, J. M., Single-Molecule Fluorescence Imaging of Interfacial DNA Hybridization Kinetics at Selective Capture Surfaces. *Anal. Chem.* **2016**, *88* (2), 1345-1354.
30. Lu, X.; Nicovich, P. R.; Gaus, K.; Gooding, J. J., Towards Single Molecule Biosensors Using Super-Resolution Fluorescence Microscopy. *Biosens. Bioelectron.* **2017**, *93*, 1-8.
31. Husale, S.; Persson, H. H. J.; Sahin, O., DNA Nanomechanics Allows Direct Digital Detection of Complementary DNA and Microrna Targets. *Nature* **2009**, *462* (7276), 1075-U1138.
32. Zijlstra, P.; Paulo, P. M. R.; Orrit, M., Optical Detection of Single Non-Absorbing Molecules Using the Surface Plasmon Resonance of a Gold Nanorod. *Nat. Nanotechnol.* **2012**, *7*(6), 379-382.
33. Gong, P.; Levicky, R., DNA Surface Hybridization Regimes. *Proc. Natl. Acad. Sci. USA.* **2008**, *105* (14), 5301-5306.
34. Halperin, A.; Buhot, A.; Zhulina, E. B., Brush Effects on DNA Chips: Thermodynamics, Kinetics, and Design Guidelines. *Biophys. J.* **2005**, *89* (2), 796-811.
35. Hao, X.; Josephs, E. A.; Gu, Q.; Ye, T., Molecular Conformations of DNA Targets Captured by Model Nanoarrays. *Nanoscale* **2017**, *9*(36), 13419-13424.
36. Abel, G. R., Jr.; Josephs, E. A.; Luong, N.; Ye, T., A Switchable Surface Enables Visualization of Single DNA Hybridization Events with Atomic Force Microscopy. *J. Am. Chem. Soc.* **2013**, *135* (17), 6399-6402.
37. Josephs, E. A.; Ye, T., A Single-Molecule View of Conformational Switching of DNA Tethered to a Gold Electrode. *J. Am. Chem. Soc.* **2012**, *134* (24), 10021-10030.
38. Gooding, J. J.; Ciampi, S., The Molecular Level Modification of Surfaces: From Self-Assembled Monolayers to Complex Molecular Assemblies. *Chem. Soc. Rev.* **2011**, *40* (5), 2704-2718.

39. Goreaud, F.; Pelissier, R., On Explicit Formulas of Edge Effect Correction for Ripley's K-Function. *J. Veg. Sci.* **1999**, *10*(3), 433-438.
40. Haase, P., Spatial Pattern-Analysis in Ecology Based on Ripley K-Function - Introduction and Methods of Edge Correction. *J. Veg. Sci.* **1995**, *6*(4), 575-582.
41. Kiskowski, M. A.; Hancock, J. F.; Kenworthy, A. K., On the Use of Ripley's K-Function and Its Derivatives to Analyze Domain Size. *Biophys. J.* **2009**, *97*(4), 1095-1103.
42. Luo, X. L.; Davis, J. J., Electrical Biosensors and the Label Free Detection of Protein Disease Biomarkers. *Chem. Soc. Rev.* **2013**, *42*(13), 5944-5962.
43. Sassolas, A.; Blum, L. J.; Leca-Bouvier, B. D., Immobilization Strategies to Develop Enzymatic Biosensors. *Biotechnol. Adv.* **2012**, *30*(3), 489-511.
44. Xiao, Y.; Lubin, A. A.; Heeger, A. J.; Plaxco, K. W., Label-Free Electronic Detection of Thrombin in Blood Serum by Using an Aptamer-Based Sensor. *Angew. Chem. Int. Ed.* **2005**, *44*(34), 5456-5459.
45. Xiao, Y.; Piorek, B. D.; Plaxco, K. W.; Heeger, A. J., A Reagentless Signal-on Architecture for Electronic, Aptamer-Based Sensors Via Target-Induced Strand Displacement. *J. Am. Chem. Soc.* **2005**, *127*(51), 17990-17991.
46. Horcas, I.; Fernandez, R.; Gomez-Rodriguez, J. M.; Colchero, J.; Gomez-Herrero, J.; Baro, A. M., Wsxn: A Software for Scanning Probe Microscopy and a Tool for Nanotechnology. *Rev. Sci. Instrum.* **2007**, *78*(1).
47. Vallee-Belisle, A.; Plaxco, K. W., Structure-Switching Biosensors: Inspired by Nature. *Curr. Opin. Struct. Biol.* **2010**, *20*(4), 518-526.
48. Martens, I.; Fisher, E. A.; Bizzotto, D., Direct Mapping of Heterogeneous Surface Coverage in DNA-Functionalized Gold Surfaces with Correlated Electron and Fluorescence Microscopy. *Langmuir* **2018**, *34*(7), 2425-2431.
49. Sim, A. Y. L.; Lipfert, J.; Herschlag, D.; Doniach, S., Salt Dependence of the Radius of Gyration and Flexibility of Single-Stranded DNA in Solution Probed by Small-Angle X-Ray Scattering. *Physical Review E* **2012**, *86*(2).
50. Gao, Y.; Wolf, L. K.; Georgiadis, R. M., Secondary Structure Effects on DNA Hybridization Kinetics: A Solution Versus Surface Comparison. *Nucleic Acids Res.* **2006**, *34*(11), 3370-3377.
51. Steel, A. B.; Herne, T. M.; Tarlov, M. J., Electrochemical Quantitation of DNA Immobilized on Gold. *Anal. Chem.* **1998**, *70*(22), 4670-4677.
52. White, R. J.; Phares, N.; Lubin, A. A.; Xiao, Y.; Plaxco, K. W., Optimization of Electrochemical Aptamer-Based Sensors Via Optimization of

Probe Packing Density and Surface Chemistry. *Langmuir* **2008**, *24*(18), 10513-10518.

53. Wong, I. Y.; Melosh, N. A., An Electrostatic Model for DNA Surface Hybridization. *Biophys. J.* **2010**, *98*(12), 2954-2963.

54. Cederquist, K. B.; Golightly, R. S.; Keating, C. D., Molecular Beacon-Metal Nanowire Interface: Effect of Probe Sequence and Surface Coverage on Sensor Performance. *Langmuir* **2008**, *24*(16), 9162-9171.

55. Cederquist, K. B.; Keating, C. D., Hybridization Efficiency of Molecular Beacons Bound to Gold Nanowires: Effect of Surface Coverage and Target Length. *Langmuir* **2010**, *26*(23), 18273-18280.

56. Watkins, H. M.; Simon, A. J.; Ricci, F.; Plaxco, K. W., Effects of Crowding on the Stability of a Surface-Tethered Biopolymer: An Experimental Study of Folding in a Highly Crowded Regime. *J. Am. Chem. Soc.* **2014**, *136*(25), 8923-8927.

57. Zhang, J. X.; Fang, J. Z.; Duan, W.; Wu, L. R.; Zhang, A. W.; Dalchau, N.; Yordanov, B.; Petersen, R.; Phillips, A.; Zhang, D. Y., Predicting DNA Hybridization Kinetics from Sequence. *Nat. Chem.* **2018**, *10*(1), 91-98.

58. <https://www.idtdna.com/pages/home>.

59. Chan, V.; Graves, D. J.; McKenzie, S. E., The Biophysics of DNA Hybridization with Immobilized Oligonucleotide Probes. *Biophys. J.* **1995**, *69*(6), 2243-2255.

60. Rill, R. L., Liquid-Crystalline Phases in Concentrated Aqueous-Solutions of Na<sup>+</sup> DNA. *Proc. Natl. Acad. Sci. USA.* **1986**, *83*(2), 342-346.

61. Strzelecka, T. E.; Davidson, M. W.; Rill, R. L., Multiple Liquid-Crystal Phases of DNA at High-Concentrations. *Nature* **1988**, *331*(6155), 457-460.

62. Strzelecka, T. E.; Rill, R. L., Solid-State P-31 Nmr-Studies of DNA Liquid-Crystalline Phases - the Isotropic to Cholesteric Transition. *J. Am. Chem. Soc.* **1987**, *109*(15), 4513-4518.

63. Murphy, J. N.; Cheng, A. K. H.; Yu, H. Z.; Bizzotto, D., On the Nature of DNA Self-Assembled Monolayers on Au: Measuring Surface Heterogeneity with Electrochemical in Situ Fluorescence Microscopy. *J. Am. Chem. Soc.* **2009**, *131*(11), 4042-4050.

64. Inada, N.; Asakawa, H.; Matsumoto, Y.; Fukuma, T., Molecular-Scale Surface Structures of Oligo (Ethylene Glycol)-Terminated Self-Assembled Monolayers Investigated by Frequency Modulation Atomic Force Microscopy in Aqueous Solution. *Nanotechnology* **2014**, *25*(30).

65. Yin, Y. D.; Zhao, X. S., Kinetics and Dynamics of DNA Hybridization. *Acc. Chem. Res.* **2011**, *44*(11), 1172-1181.

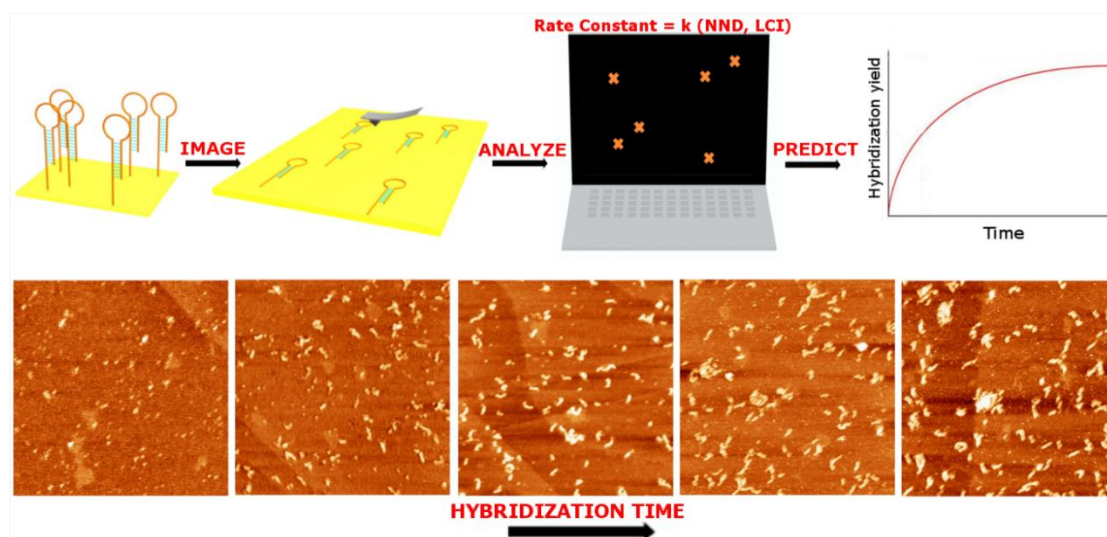
66. Chen, C. L.; Wang, W. J.; Wang, Z.; Wei, F.; Zhao, X. S., Influence of Secondary Structure on Kinetics and Reaction Mechanism of DNA Hybridization. *Nucleic Acids Res.* **2007**, *35* (9), 2875-2884.

## Chapter 3

# Nanoscale Spatial Organization of Probe Molecules is a Major Determinant of the Hybridization Kinetics of Surface Immobilized Hairpin DNA Probes

Lonely and lonesome, bleak and bitter, deep in dreary thoughts I missed you miserably so. In a season when warmth could suddenly a chill become, unable to rest was a weary soul. How could light wine of two or three pours fend off a rush of wind in the late hours? As wild geese flew by, in sorrow I dwelled, and remembered how I had seen them before. On grounds in piles were petals of yellow. Wilting in grief, who'd these flowers pick? By the window I pined, in solitude how could I while away the day till darkness arrived? Drizzle through phoenix trees fell, at twilight, drops and drips dribbled and rolled. In fall, how could sorrow possibly spell a melancholy overflow!

Li Qingzhao, Lyric to the Adagio Resonance



**Abstract:** Hybridization of DNA probes immobilized on a solid support is a key process for DNA biosensors and microarrays. Although the surface environment is known to influence the kinetics of DNA hybridization, so far it has not been possible to quantitatively predict how hybridization kinetics is influenced by the complex interactions of the surface environment. Herein, we show that the hybridization kinetics of an electrochemical DNA (E-DNA) sensor may be quantitatively predicted if the lateral spatial pattern of the immobilized DNA probes can be determined. Using spatial statistical analysis of probes and hybridized target molecules on a few E-DNA sensor surfaces, we developed a model that describes how the hybridization rates for single probe molecules are determined by the local environment. The predicted single-molecule rate constants, upon incorporation into the numerical simulation reproduced the overall kinetics of E-DNA sensor surfaces at different probe densities and different degree of probe clustering. Our study showed that the nanoscale spatial organization is a major factor behind the counter-intuitive trends in hybridization kinetics. It also highlights the importance of models that can account for heterogeneity in surface hybridization. The molecular level understanding of hybridization at surfaces and accurate prediction of hybridization kinetics may lead to new opportunities in development of more sensitive and reproducible DNA biosensors and microarrays.



### 3.1. Introduction

The molecular recognition of surface bound ligands/probes is a key step in numerous biotechnological devices, such as biosensors, and microarrays,<sup>1</sup> as well as in many biological phenomena, such as cell adhesion,<sup>2</sup> immune responses.<sup>3</sup> As the surface environment is often crowded with molecules, an open question is how such crowding interactions alter the binding affinity and binding kinetics of interfacial molecular recognition. The question has been challenging as the spatial organization of these molecules is often heterogeneous and poorly characterized. Here we seek to understand how the nanoscale lateral distribution of DNA probes immobilized on a solid support influences surface hybridization, which is key to many DNA sensors and microarrays that are being used for applications ranging from gene profiling,<sup>1</sup> *in vivo* monitoring,<sup>4</sup> to point of care diagnostics.<sup>5-7</sup> Many studies showed that as the average surface density of probe molecules increases,<sup>8-15</sup> crowding interactions such as steric hinderance and electrostatic repulsion not only reduce binding affinity but also decelerate the binding kinetics. However, the average probe surface density is unlikely a reliable descriptor for crowding interactions when the lateral organization of probe molecules is often far from homogeneous.<sup>16-18</sup> Indeed, some studies provided indirect evidence that heterogeneous probe densities may be the origin of significant device-to-device signal variabilities.<sup>19-22</sup> Previously, we have enabled a new atomic force microscopy (AFM) method to spatially resolve<sup>23</sup> the probe molecules and hybridized targets of electrochemical DNA (E-DNA) sensor surfaces, which utilize the conformational changes of surface-immobilized electroactive DNA probes upon target binding to detect analytes.<sup>24</sup> While it is commonly assumed that molecular crowding inhibits target capture,<sup>11, 25-26</sup> single molecule imaging observed an unexpected cooperative effect: the presence of neighboring hairpin probes may substantially accelerate target binding under specific circumstances. However, a direct, quantitative correlation between nanoscale lateral organization of the DNA probes and the overall hybridization kinetics has remained elusive. As the hybridization kinetics determines key figures of merit, such as limit of detection and detection speed, such a structure-function relationship is critically needed for rational engineering DNA based sensors and microarrays.

Here we have combined high resolution imaging of the DNA probes and hybridized DNA target molecules with statistical models of single molecule rate constants to investigate how the overall kinetics of surface hybridization is influenced by the interfacial environment. We found that as the probe density increased from  $1.83 \times 10^{10}$  to  $2.03 \times 10^{11}$  probes/cm<sup>2</sup>, the overall hybridization kinetics displayed a non-monotonic trend that is difficult to explain using the overall surface densities. However, the trend could be readily rationalized by examining the local probe spatial organization, such as the

nanoscale distance to the nearest DNA probe. Moreover, the overall kinetics of surface hybridization were largely reproduced by numerical simulations based on our statistical model of single molecule rate constants that included the effects of the nanoscale crowding at the surface. Simulation also successfully predicted divergent hybridization kinetics of two surfaces with similar overall surface densities but different spatial patterns of probe molecules. Overall, our work provides direct evidence that the local probe spatial organization is a determining factor in the kinetics of surface hybridization of hairpin probes. By providing a new framework that connects the spatial patterns of DNA probes to the hybridization kinetics, our study represents a step toward elucidating the structure-function relationship of DNA biosensors and microarrays and rational engineering of devices that are capable of sensitive, rapid and highly reproducible detection of target molecules.

## **3.2. Methods and materials**

### **3.2.1. Materials**

Tris-(2-carboxyethyl) phosphine hydrochloride (TCEP) and 11-mercaptoundecanoic acid (MUDA) were purchased from Sigma-Aldrich Inc. (St. Louis, MO). 99.99% gold wire with 1mm diameter was purchased from Scientific Instrument Service (Ringoes, NJ). The oligonucleotide probe (HP) and target (T) with sequences summarized in Table 3.1 were synthesized by Biosearch Technologies, Inc. (Petaluma, CA) and Integrated DNA Technologies (Coralville, IA) respectively. Unless otherwise specified, all chemicals were purchased from Fisher Scientific Co. (Pittsburgh, PA).

### **3.2.2. E-DNA sensor fabrication and hybridization**

To form the MUDA self-assembled monolayer, a gold bead containing single-crystal Au(111) facets prepared by melting the gold wire based on Clavilier's method<sup>27</sup> was cleaned in hot nitric acid and flame-annealed with hydrogen. The gold bead was then incubated overnight in a 1mM MUDA ethanolic solution that contains 10% (v/v) of acetic acid. After incubation, the gold bead was thoroughly rinsed with 9:1 (v/v) ethanol:acetic acid, and then ultrapure water. The disulfide oligonucleotide probe was mixed with a tris(2-carboxyethyl)phosphine (TCEP) reduction buffer for 20 min at room temperature in dark. After reduction, the reaction mixture was purified using a QIAGEN nucleotide removal kit (Germantown, MD) and immediately used in all experiments. The MUDA functionalized gold bead was immersed in an insertion buffer for 30 min with the following composition: purified oligonucleotide probe, 2 mM TCEP and 50 mM NaAc (all E-DNA sensor surfaces except for the clustered surface S5 in Figure 3.4, which was prepared using 250 mM NaAc). The detailed insertion conditions used in this work were summarized in Table 3.2.

All hybridization experiments were performed at a fixed target (T) concentration of 100 nM in the phosphate buffer (10 mM Phosphate, 1M NaAc, pH7) for a predetermined time. The gold bead was then thoroughly rinsed with an STAE buffer (1 x TAE, 200 mM NaAc) to remove the unbound oligonucleotide targets. To track the hybridization kinetics, the gold bead was completely submerged in an alkaline buffer containing 10 mM NaOH and 330  $\mu$ M EDTA (pH10) for 5 min to denature the target-probe duplexes after each target incubation.

### 3.2.3. AFM measurement and image analysis

All AFM images were acquired with Ntegra Vita AFM (NT-MDT Co., Moscow, Russia) or Keysight 5500 AFM (Keysight Technologies, Santa Rosa, CA) under intermittent contact mode (tapping mode) with E-DNA sensor surface exposed to an imaging buffer of 5 mM NiAc<sub>2</sub> and 0.1 x TAE. SNL-10 AFM tips (Bruker, Bellerica, MA) with a spring constant of approximately 0.3 N/m were used in all experiments. STAE buffer was used to remove the remaining Ni<sup>2+</sup> from the surface prior to each target incubation.

All AFM images were first-order flattened using WSxM 5.0 software from Nanotec Electronica.<sup>28</sup> An average probe density was determined by manually masking the features of probes and automatically counting the total number of masks using Gwyddion (<http://gwyddion.net/>) in each AFM image. The XY-coordinates of the probes were extracted from the corresponding masks and used for nearest neighbor distance (NND) and local crowding index (LCI) analyses. The former measures the distance between the closest neighboring molecules and the later counts the number of neighboring molecules surrounding a specific molecule. The hybridization yield was determined by counting the number of target-probe duplexes and dividing it by the total number of probes.

### 3.2.4. DLS measurement

The size and size distribution of target molecules (100 nM and 1  $\mu$ M) in PBS7 buffer were measured using a Malvern Zetasizer Nano-S90 (Malvern Instruments Ltd., Malvern, UK), as shown in Figure 3.5. Measurement parameters were as follows: a laser wavelength of 633 nm, a scattering angle of 90°, a room temperature of 25°C and an accumulation time of 100 sec. Before DLS measurement, the target solution was loaded into a Malvern quartz cuvette (ZEN2112) QS 3.00. The Stokes-Einstein equation is used to determine the hydrodynamic diameter of the target molecules

$$d = \frac{kT}{3\pi\eta D} \quad (3.1)$$

where  $k$  is the Boltzmann constant,  $T$  is the temperature,  $\eta$  is the viscosity and  $D$  is the diffusion coefficient, respectively.

### 3.2.5. Damköhler Number

The rate of target capture is governed by both hybridization kinetics and diffusion. To determine the relative importance of two processes, we calculated the Damköhler number<sup>29</sup>

$$Da = \frac{K\sigma h}{D_{diff}} \quad (3.2)$$

where  $K$  is the apparent rate constant extracted from the overall kinetic traces by fitting the data to an irreversible first-order Langmuir adsorption model,  $\sigma$  is the probe surface density,  $h$  is the fluidic channel height and  $D_{diff}$  is the diffusion coefficient calculated using the Einstein-Stokes equation with hydrodynamic diameter derived from dynamic light scattering (DLS) measurements (Figure 3.5). The small values of the Damköhler number ( $< 0.08$  for all cases we consider) indicate that the target diffusion is fast enough to supply the surface hybridization reaction.

### 3.2.6. Irreversible first-order Langmuir

For probes in each of the categories of NNDs and LCIs, we performed kinetic trace fitting using an irreversible first-order Langmuir adsorption model  $HP + T \rightarrow HPT$  following equation,

$$\Gamma = 1 - e^{-K[T]t} \quad (3.3)$$

where  $K$  is the overall rate constant and  $[T]$  is the target concentration. All fittings were performed with MATLAB using curve fitting package. The corresponding rate constants were extracted and plotted in Figure 3.3a.

### 3.2.7. Cox proportional hazard model

The Cox proportional hazard model (Cox PHM)<sup>30</sup> is widely used in the biological sciences to study how influencing factors affects the survival rate. Our E-DNA sensor meets the three prerequisites for the appropriate use of the Cox PHM: (1) Independence of the rate constants between distinct individual probes. (2) A constant rate constant over time (reaction limited). (3) Multivariable correlation between the single-molecule rate constant and the spatial variables. The Cox PHM can be generally written as follows:

$$k_i = k_0 \exp(b_1 X_1 + b_2 X_2 + \dots + b_n X_n) \quad (3.4)$$

where  $k_i$  is the expected single-molecule rate constant,  $k_0$  is the base line rate constant represents the rate constants when all the variables ( $X_1, X_2 \dots X_n$ ) are equal to zero and  $b_1, b_2 \dots b_n$  are the regression parameters. The Cox PHM fitting was performed across all rate constants (Figure 3.3a) using curve fitting

package in MATLAB. A modified exponential equation (Equation 3.9) which takes into account both NND and LCI was used, as depicted in Figure 3.3b.

### 3.2.8. Numerical simulation of the overall kinetics

In numerical simulation, one random number  $r$  is created per iteration, each sampled from a uniform distribution bounded by 0 and 1.  $r$  is used to compute the time of each step  $\Delta t$ ,

$$\Delta t = \frac{1}{K} \ln \left( \frac{1}{r} \right) \quad (3.5)$$

where  $K$  is the average rate constant with the following expression:

$$K = \sum_i^N \rho_i k_i \quad (3.6)$$

where  $\rho_i$  is the fraction of probes for each single-molecule rate constant  $k_i$ . The fraction of hybridized probes in each iteration can be expressed as follows,

$$\rho_{hyb} = K[T]\Delta t \quad (3.7)$$

The fraction of probes  $\rho_i$  is recalculated in each iteration,

$$\rho_i' = \frac{\rho_i - k_i[T]\Delta t}{\sum_i^N \rho_i - k_i[T]\Delta t} \quad (3.8)$$

Individual iterations are accumulated to generate the overall kinetic trace. Numerical simulation of an E-DNA sensor hybridization with 100 nM target was performed using the following algorithm in MATLAB:

- (1) Categorize the probes according to their NNDs and LCIs and the fraction of each category is calculated.
- (2) For each category of probes with different NND and LCI, generate the single-molecule rate constant by plugging its values of NND and LCI into Equation 3.9 (Cox PHM). Calculate the average rate constant  $K$  using Equation 3.6.
- (3) In each iteration, generate one random number  $r$  from 0 to 1. Random number  $r$  determines the time interval using Equation 3.5.
- (4) The fraction of hybridized probes in each iteration is computed using Equation 3.7 and the fraction of each type of probes is recalculated using Equation 3.8.
- (5) Repeat the iteration until the set time is reached.

Each simulation experiment is repeated 100 times and averaged results are presented in Figure 3.3c and 3.4d.

### 3.3. Results and discussion

We chose to focus on E-DNA sensor surfaces<sup>31</sup> for a number of reasons. First, these sensor surfaces have been widely studied due to their high selectivity and potential in point of care diagnostics and in vivo monitoring.<sup>4, 26</sup> Second, these surfaces are an ideal model system for investigating how spatial organization of single molecules influences molecular recognition as highly ordered self-assembled monolayers may be used to minimize the impact of uncontrolled morphological and compositional heterogeneities.<sup>19</sup> Third, these surfaces are compatible with an imaging technique that can spatially resolve individual probes and captured DNA targets even when the inter-probe separation is less than 10 nm.<sup>32</sup> Stem-loop probes (a stem length of 6 bps and a loop length of 11 bases) modified with a thiol group at the 5' end were immobilized onto a preassembled 11-mercaptopundecanoic acid (MUDA) self-assembled monolayer (SAM) on a single-crystal Au (111) support. As shown previously,<sup>33</sup> the surface serves as a functioning electrochemical sensor as the electrochemical signal (differential pulse voltammetry). Details of the preparation and characterization of the interface can be found in the Methods and Materials section. A target molecule (T) consisting a 19-bp double-stranded tail, a 2-base spacer, and a 19-base single-stranded sticky-end was designed to facilitate AFM identification of the target-probe duplexes. Hybridization was performed by exposing the probe-modified single-crystal gold surface to the desired concentration of targets. To create a sufficiently representative data set for developing a predictive model of single-molecule rate constants, we used AFM to measure the hybridization yields of the same biosensor surface at different time points and about 2000 individual probes were analyzed at each time point. Figure 3.2a-d exhibited distinct conformations before (compact dot-like features) and after hybridization (extended worm-like features), allowing direct quantification of the hybridization yield by counting the number of hybridized probes and dividing it by the total number of probes, as illustrated by the symbols in Figure 3.2e. In all experiments, the targets were kept at a fixed concentration of 100 nM, to ensure a hybridization time scale of hours and minimize the aggregation of targets (Figure 3.5).<sup>33</sup> Kinetic traces, consisting of the hybridization yield as a function of time, were determined for probe coverages ranging from  $1.83 \times 10^{10}$  to  $2.03 \times 10^{11}$  probes/cm<sup>2</sup>, or 183 to 2030 probes/ $\mu\text{m}^2$ .

Figure 3.2e shows that the hybridization kinetics slowed down as the probe densities increased from  $1.83 \times 10^{10}$  to  $8.25 \times 10^{10}$  probes/cm<sup>2</sup> (cyan, blue and then black dashed curves), which appears to be consistent with the ensemble-averaging-based observations that increasing molecular crowding inhibits target binding.<sup>8-15</sup> However, the hybridization kinetics accelerated when the probe density increased to  $2.03 \times 10^{11}$  probes/cm<sup>2</sup> (green dashed curve). The nonmonotonic trend is difficult to rationalize. If an increasing overall probe

density reduces the accessibility of the probes to target molecules, surface hybridization should consistently decelerate as the probe density increases. If instead probe crowding destabilizes hairpin conformation and reduces the barrier for hybridization as shown in our previous study,<sup>33</sup> the hybridization kinetics should consistently accelerate as the probe density increases. Even if the trend results from the interplay between these two competing effects, *i.e.*, inhibition at low probe densities due to reduced accessibility, and acceleration at higher densities due to destabilization of the hairpins, it remains unclear why reduced accessibility is observed even at such low probe densities  $< 8.25 \times 10^{10}$  probes/cm<sup>2</sup> (black dashed curve).

Since this counter-intuitive trend in binding kinetics is not readily explained by the overall probe density alone, we examined the impact of nanoscale spatial organization of probe molecules. Using single molecule imaging, our previous work found that individual probe molecules with low NNDs have faster hybridization kinetics, possibly because the hairpin destabilization by crowding interactions accelerates hybridization.<sup>33</sup> Moreover, even when the probes have similar NNDs, those with higher local crowding indices (LCIs), which describe crowding interactions beyond nearest neighbors by counting probe molecules within a radius 20 nm (equivalent to about twice the length of the probe), have faster hybridization rates.<sup>33</sup> To investigate whether the local spatial organization of probe molecules can account for the observed counter-intuitive trends in overall kinetics at different overall probe densities, we categorized the probes according to their NNDs and LCIs and the fraction of each category is displayed in a color map (Figure 3.2f). Figure 3.2f presents an increase in the most probable NND (yellow and orange domains) from 10 nm to 40 nm while the corresponding LCIs remain 1 or 2, when the overall density increased from  $1.83 \times 10^{10}$  to  $8.25 \times 10^{10}$  probes/cm<sup>2</sup>. This shift provides an alternative explanation for the slowdown of the overall kinetics with increasing overall density: the rising population of probes with high NNDs, which leads to lower rate constants. That a surface with a higher overall probe density has larger overall NNDs, *i.e.*, less probe crowding, is rather unexpected. However, the probe immobilization process is not completely random. Although the insertion method, which insert DNA into a preformed SAM, is known to produce a more uniform probe spatial pattern than the traditional backfilling method,<sup>19</sup> the AFM images in Figure 3.6 show that at the lowest surface density investigated ( $1.83 \times 10^{10}$ /cm<sup>2</sup>), the immobilized probes preferentially cluster near the step edges of the underlying gold substrate (green arrows), where the SAM defects are concentrated. The NNDs are substantially smaller than those on a surface with complete spatial randomness, which was estimated by averaging over 100 simulations of random points patterns with the same sample size and area as the AFM data, as shown in Figure 3.7a. As the surface density of probe molecules further increases, such SAM defects are saturated, and more and more DNA probes are inserted at random locations. Indeed, the NNDs of these surfaces are similar or higher than those of a

surface with complete spatial randomness (Figure 3.7b-d). Therefore, the slower hybridization kinetics is caused by increased NNDs, which reduced crowding effect that may destabilize the hairpins. Moreover, as the overall density further increases to  $2.03 \times 10^{11}$  probes/cm<sup>2</sup>, the most probable NND is reduced to 15 nm and the most probable LCI increases to 5. It should be noted that the majority of the probes possess NNDs smaller than that of  $4.44 \times 10^{10}$  and  $8.25 \times 10^{10}$  probes/cm<sup>2</sup>, and thus the corresponding kinetic traces differ considerably from each other (Figure 3.2e, green versus blue and black dashed curves, respectively). This acceleration in kinetics may also be ascribed to the abundance of probes with a high LCI of 5, whereas the surfaces with lower probe densities of  $4.44 \times 10^{10}$  and  $8.25 \times 10^{10}$  probes/cm<sup>2</sup> have LCI of 1 or 2.

These spatial statistical analyses revealed that the local proximity-induced enhancement in target binding of the individual probes can qualitatively explain counter-intuitive trends in the overall hybridization kinetics of the E-DNA sensor surface. The next question is whether a quantitative relationship between the local probe spatial pattern and the overall kinetics can be established. To address this question, we built a phenomenological kinetic model to predict rate constants of probe molecules in different local environments as described by NNDs and LCIs (Figure 3.3). Then we incorporated the single-molecule rate constants predicted by our model into the numerical simulation (see Methods and Materials for details), which allowed the prediction of the overall kinetics for a given probe spatial pattern and comparison with experimental data. Since the surface hybridization is reaction-limited, as indicated by the small values of the Damköhler number ( $< 0.08$  for all cases we consider, see details in Methods and Materials), we extracted the rate constants from the first-order Langmuir fitting of the kinetic curves in each of the categories of NNDs and LCIs mentioned above and displayed as a 2D histogram, as viewed in Figure 3.3a. The histogram demonstrates that the rate constant can vary by more than one order of magnitude and the highest rate (red histograms) was observed for those probes with low NND and high LCI, highlighting the multivariable nature of the rate constants.

Based on the histogram, we proposed a model to predict the single-molecule rate constant based on both NND and LCI. The Cox proportional hazard method (Cox PHM) is a multivariable method that uses a parametric linear combination of all risk factors to predict the survival rate in biology.<sup>30</sup> We applied the same concept to model the single-molecule rate constant using the following expression,

$$k_i = k_0 \exp(\alpha_{LCI} LCI_i + \beta_{NND}/NND_i) \quad (3.9)$$

where  $k_0$  is the baseline rate constant,  $\alpha_{LCI}$  and  $\beta_{NND}$  are regression parameters related to LCI and NND, respectively (Figure 3.3b). It should be



noted that  $k_i$  converges into a constant baseline rate constant  $k_0$  at infinity where LCI = 0 and NND = infinity. To justify the use of the two-parameter ( $\alpha_{LCI}$  and  $\beta_{NND}$ ) Cox PHM model, we applied the Bayes-Schwartz Information Criterion (BIC)<sup>34</sup> in which the addition of a new parameter will decrease the negative log-likelihood by  $\log(N)/2$ , where N is the total number of probes, i.e. the negative log-likelihood must be at least 3.8 (2044 probes in total) more than that of the null hypothesis ( $\alpha_{LCI} = 0$  and  $\beta_{NND} = 0$ ). We performed a maximum likelihood estimation (MLE) across all the probes using Equation 3.9 and we find negative log-likelihood of 20.69 and 287.52 exceed those of the null hypothesis for  $\alpha_{LCI}$  and  $\beta_{NND}$  respectively, justifying their appearance in single-molecule rate constant equation. Using the database of known single-molecule rate constants in Figure 3.3a, our model makes the prediction for  $k_i$  of an unknown hybridization reaction  $i$ . We found  $k_0 = 650.7 \text{ M}^{-1}\text{s}^{-1}$ ,  $\alpha_{LCI} = 0.1083 \text{ probe}^{-1}$  and  $\beta_{NND} = 22.01 \text{ nm}^{-1}$ . The obtained  $k_0$  is similar to what has been observed for hairpin probes in solution.<sup>35</sup> These hairpin probes have lower rate constants than linear probes because unlike linear probes, the hybridization of hairpin probes requires the melting of the stem. The parameter  $\beta_{NND}$  corresponds to the length scale where the crowding interaction can influence hybridization. This value is remarkably close to twice the length of the hairpin probe. As the surface immobilized hairpin molecules can rotate around their anchor points, the contour length defines their “spheres of influence”. Hence the presence of a hairpin molecule may alter the hybridization kinetics a hairpin of which the anchor point is twice the contour length away.

To connect these single-molecule behaviors in heterogeneous local environments to the overall hybridization kinetics, we incorporated the single-molecule rate constants predicted by our model into the numerical simulation, whose details are described in Methods and materials. As depicted in Figure 3.3c, the simulated kinetics traces, resulting from an average over 100 simulations (Figure 3.8), well reproduced the experimental data in Figure 2e. This includes both the inhibition from  $1.83 \times 10^{10}$  to  $8.25 \times 10^{10}$  probes/cm<sup>2</sup> and acceleration at  $2.03 \times 10^{11}$  probes/cm<sup>2</sup>. The overestimation at  $2.03 \times 10^{11}$  probes/cm<sup>2</sup> may be attributed to the errors in determining the rate constants arising from the limited resolution incapable of accurately identifying the tether points (side-by-side comparison of AFM-derived kinetics to simulations is shown in Figure 3.9). This effect is most pronounced at the surface of  $2.03 \times 10^{11}$  probes/cm<sup>2</sup>, which has a relatively high most probable NND (green dashed curve in Figure 3.2e vs green solid curve in Figure 3.3c). Because the target-probe duplex is significantly longer (26 nm), there is significant overlap between the features in the AFM image as the target molecules crowd the surface. As the spatial resolution of AFM is about 3-5 nm, it becomes difficult to identify the tether points on this crowded surface and accurately measure NND and LCI.

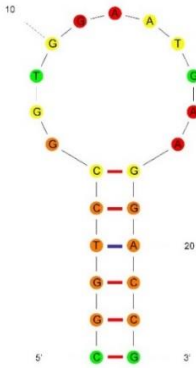
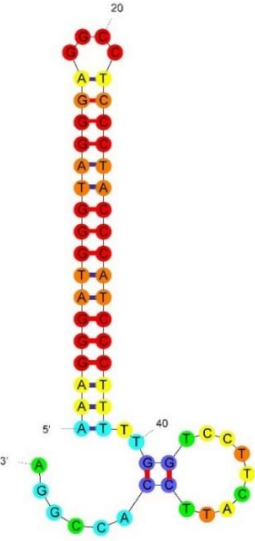
Our initial success in reproducing the overall hybridization kinetics at different probe densities lends support to our hypothesis that the local spatial arrangement of the probes is a major determinant of the overall kinetics of the biosensor. However, the validity of the model needs to be independently tested on a new E-DNA sensor surface that has not been used to establish the model of single molecule rate constants. A surface with a probe density of  $7.66 \times 10^{10}$  probes/cm<sup>2</sup> (Figure 3.4a), which is close to its counterpart of  $8.25 \times 10^{10}$  probes/cm<sup>2</sup> in Figure 3.2c, was prepared by changing both the salt (NaAc) and probe concentrations during the insertion step (see Methods and Materials for details). Unlike its counterpart, which possesses a relatively uniform distribution of probes (Figure 3.2c), the surface featured highly clustered probes. This is supported by the spatial statistics illustrating a major population of probes with a low NND of 15 nm and a high LCI of 4 (Figure 3.4c), which deviates from its counterpart with a NND of 30 nm and a LCI of 1 or 2 in Figure 3.2f. Numerical simulation based on the spatial patterns and our phenomenological kinetic model showed that despite the similar probe surface density, the kinetic trace of S5 (yellow solid curve in Figure 3.4d) would deviate significantly from the kinetic trace of S3 (black solid curve in Figure 3.2e or 3.4d). Due to the increased local crowding, the hybridization of S5 would be substantially faster than that of S3. Interestingly, the simulated traces in S5 (Figure 3.4d) was able to predict the major features of the experimental traces (Figure 3.4b). The divergent kinetic traces of E-DNA sensor surfaces with similar average surface densities but different spatial patterns constitute the clearest evidence that the average probe densities that are widely used<sup>8-15, 18</sup> do not serve as a reliable descriptor of the crowding interactions or predictor for the device performance. Together, these results revealed that the observed counter-intuitive overall kinetics of surfaces with similar or different probe densities are indeed a consequence of complex interactions comprising “two-body interactions” between nearest-neighboring probes, which depends on the inter-probe distance, and “many-body” interactions among the surrounding probes, which depends on the number of probes in a given area. Notably, while uniform probe densities are commonly considered to be more desirable because they are assumed to lead to more facile target capture for DNA sensors,<sup>20, 36</sup> the results herein paints a more complex picture. The more facile hybridization of S5 suggests that some degree of probe clustering may accelerate surface hybridization of hairpin probes.

### 3.4. Conclusion and outlook

In this study, high-resolution AFM imaging and a model of single-molecule rate constants were combined with numerical simulation, resulting in a framework that is capable of predicting the overall hybridization kinetics on various E-DNA sensor surfaces. The first successful prediction of the kinetics of surface hybridization using the nanoscale structural information of the

surface provide conclusive evidence that the spatial organization of the probe molecules is a major determinant of the performance of the devices. The framework established here provides a crucial starting point for more complex models encompassing additional factors such as the crowding effect of the target molecules. Moreover, the experimentally determined model of the single molecule rate constants in different local environments will serve as a benchmark to evaluate biophysical models<sup>1, 16</sup> that can help understand how crowding interactions influence interfacial molecular recognition and allow us to predict the behaviors of other types of DNA probes, such as linear probes, in crowded nanoscale environments. The molecular level understanding of the structure-function relationship of interfacial molecular recognition will unravel the origin of the significant device-to-device variabilities.<sup>21, 23-24, 37-38</sup> Moreover, the fundamental understanding may enable new design rules to rationally engineer the spatial patterns of probe molecules that will improve the performance of DNA biosensors and microarrays.

**Table 3.1.** Sequences of oligonucleotides and the corresponding secondary structures (generated using the mfold web server with the parameters set at 25°C and 1M Na) used in this study.

DNA Sequence & Modifications (5'-3')
<p data-bbox="467 380 1245 411">SS-(CH<sub>2</sub>)<sub>11</sub>-CGGTCCGGTGGGAATGAAGGACCG-NH<sub>2</sub>-MB</p> 
<p data-bbox="548 808 1172 877">AAAGGGATGGGTAGGGAGGCCTCCCTACC CATCCCTTTTGGTCCTTCATTCCACCGGA</p> 

**Table 3.2.** Summary of the probe insertion conditions.

Probe Density	$1.83 \times 10^{10}$ probes/cm <sup>2</sup>	$4.44 \times 10^{10}$ probes/cm <sup>2</sup>	$8.25 \times 10^{10}$ probes/cm <sup>2</sup>	$2.03 \times 10^{11}$ probes/cm <sup>2</sup>	$7.66 \times 10^{10}$ probes/cm <sup>2</sup>
Probe Concentration	250 nM	500 nM	1000 nM	2000 nM	100 nM
Na <sup>+</sup> Concentration	50 mM	50 mM	50 mM	50 mM	500 mM

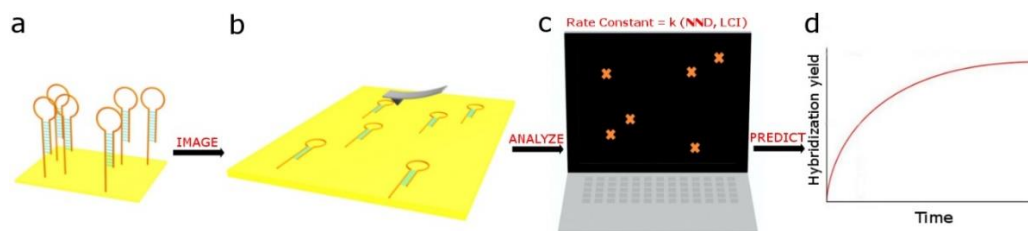


**Figure 3.1. Schematic overview of the kinetics prediction approach.** (a) The hairpin probes are immobilized on a single crystal Au surface and (b) scanned under AFM. (c) The spatial coordinates of the probes are extracted from analyzing the AFM images and then used to compute the single-probe rate constant using two key parameters in the nanoscale spatial patterns of probe molecules, NND, nearest neighbor distance, LCI, local crowding index. (d) The rate constants are implemented into the numerical simulation to predict the hybridization kinetics.

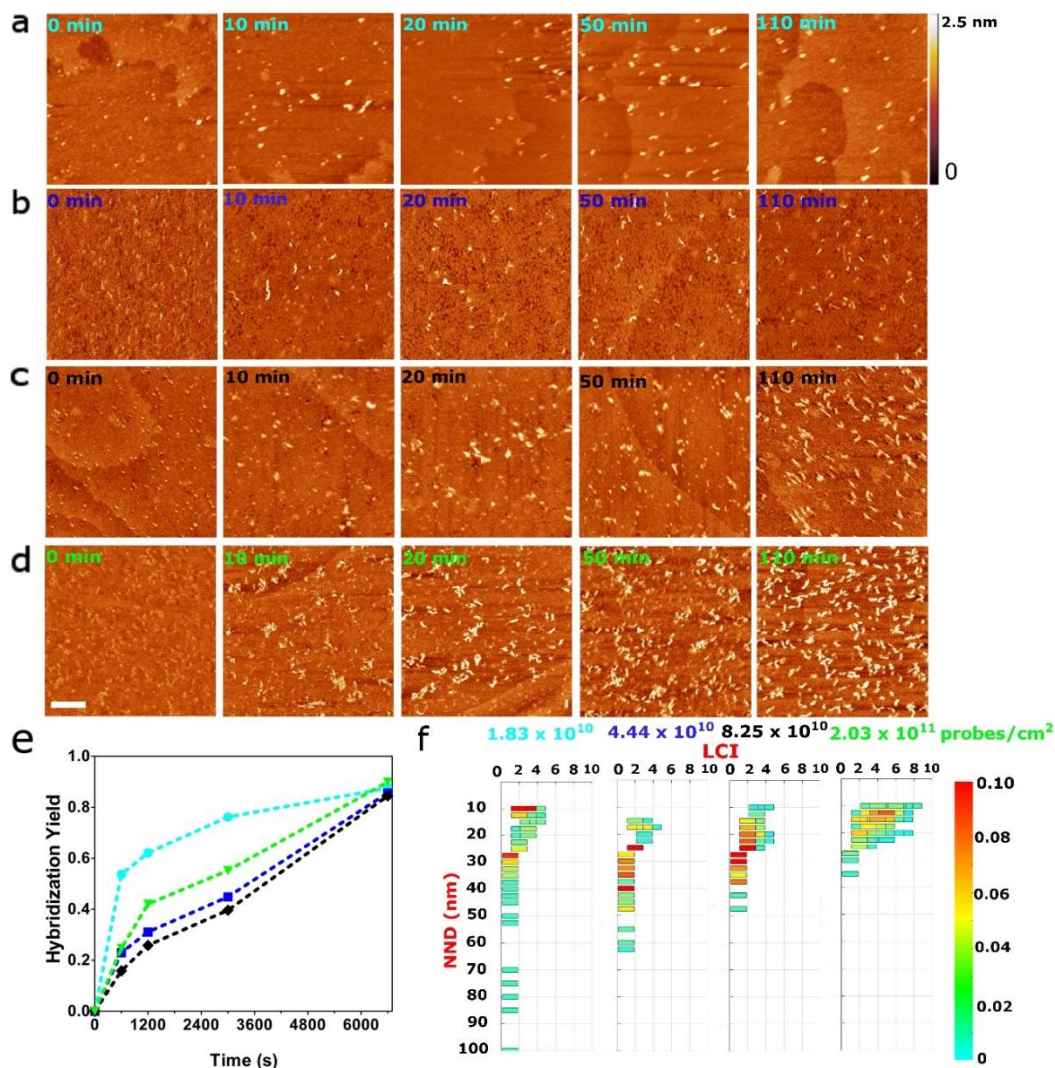


**Figure 3.2. Tracking time evolution of DNA surface hybridization.** (a-d) Representative AFM images and (e) the corresponding kinetics of the biosensor surface in the presence of 100 nM target DNA at  $1.83 \times 10^{10}$  (S1, cyan),  $4.44 \times 10^{10}$  (S2, blue),  $8.25 \times 10^{10}$  (S3, black) and  $2.03 \times 10^{11}$  (S4, green) probes/cm<sup>2</sup>. The scale bar is 100 nm. (f) Spatial organizations of the probes as a function of both NND and LCI at different probe densities.

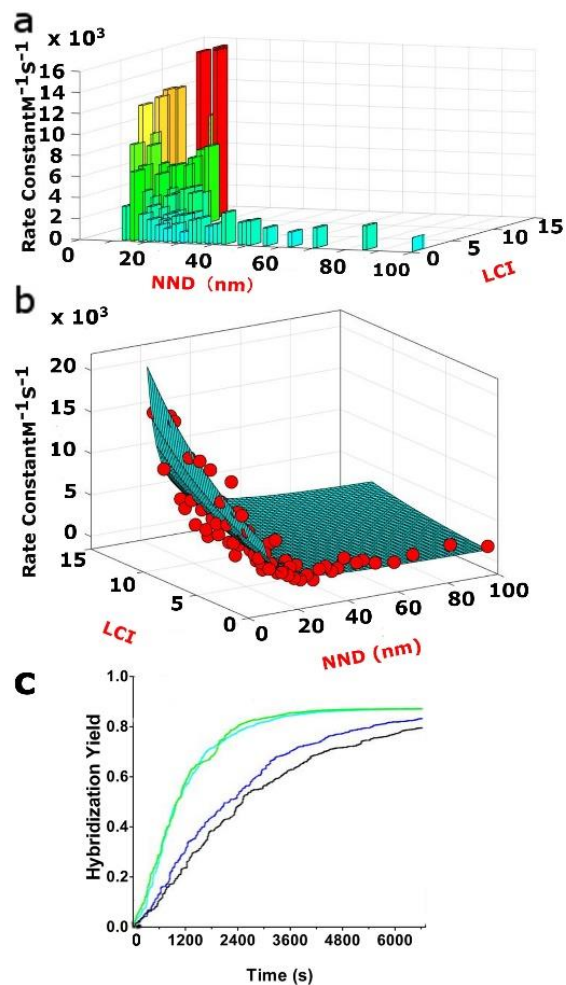


**Figure 3.3. Modeling and predicting the overall hybridization kinetics based on local spatial pattern.** (a) Rate constants distribution of the probes as a function of both NND and LCI. (b) Cox proportional hazard fitting of the rate constants. (c) Numerical simulation of the overall kinetics using the single-molecule rate constants predicted by the Cox proportional hazard model at  $1.83 \times 10^{10}$  (S1, cyan),  $4.44 \times 10^{10}$  (S2, blue),  $8.25 \times 10^{10}$  (S3, black) and  $2.03 \times 10^{11}$  (S4, green) probes/cm<sup>2</sup>.



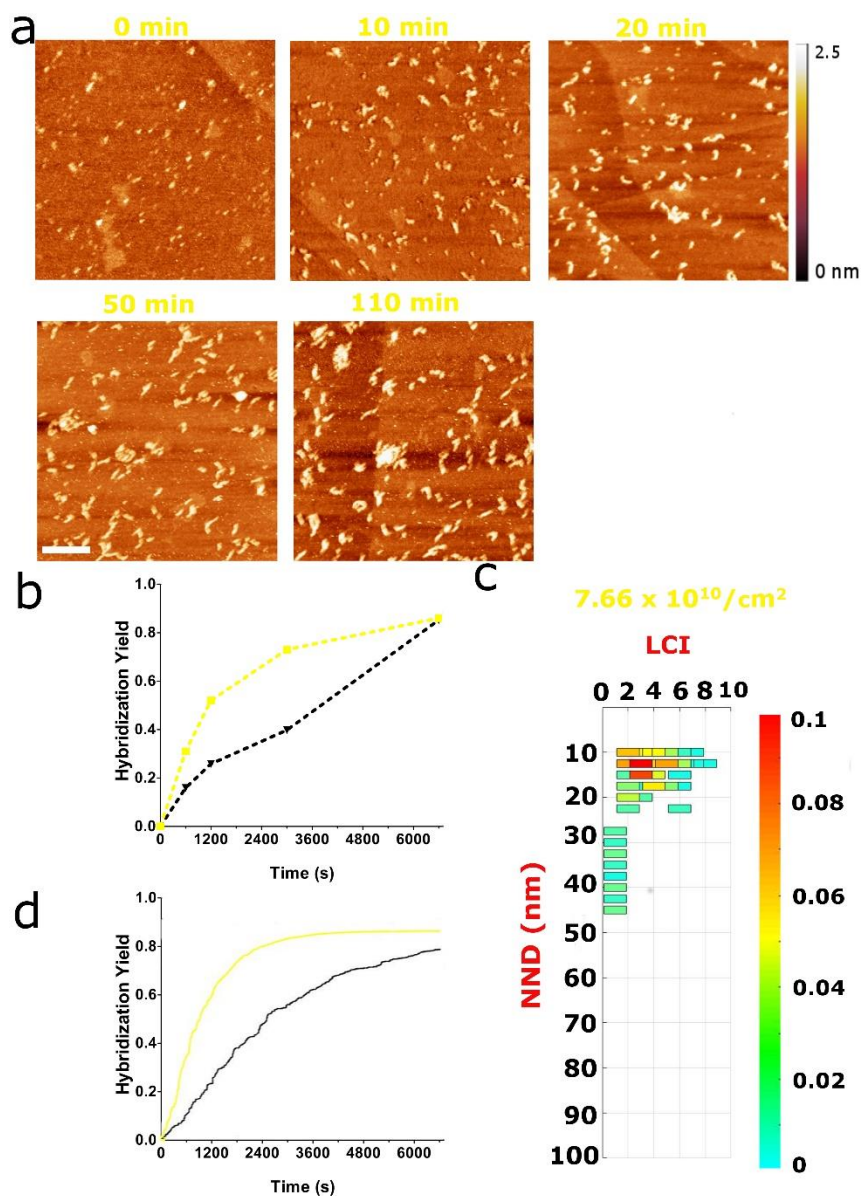


**Figure 3.4. Predicting the overall hybridization kinetics of surfaces with similar probe densities but different probe spatial patterns.** (a-b) Representative AFM images and the corresponding kinetics of the sensor surface S5, in the presence of 100 nM target DNA at  $7.66 \times 10^{10}$  probes/cm<sup>2</sup> (yellow dashed line), which is similar to the surface density of S3  $8.25 \times 10^{10}$  probes/cm<sup>2</sup> (black dashed line). The scale bar is 100 nm. (c) Spatial organizations of the probes as a function of both NND and LCI at different probe densities. (d) Numerical simulation of the overall kinetics using the single-molecule rate constants predicted by the Cox proportional hazard model at  $7.66 \times 10^{10}$  (yellow solid line) and  $8.25 \times 10^{10}$  (black solid line) probes/cm<sup>2</sup>.

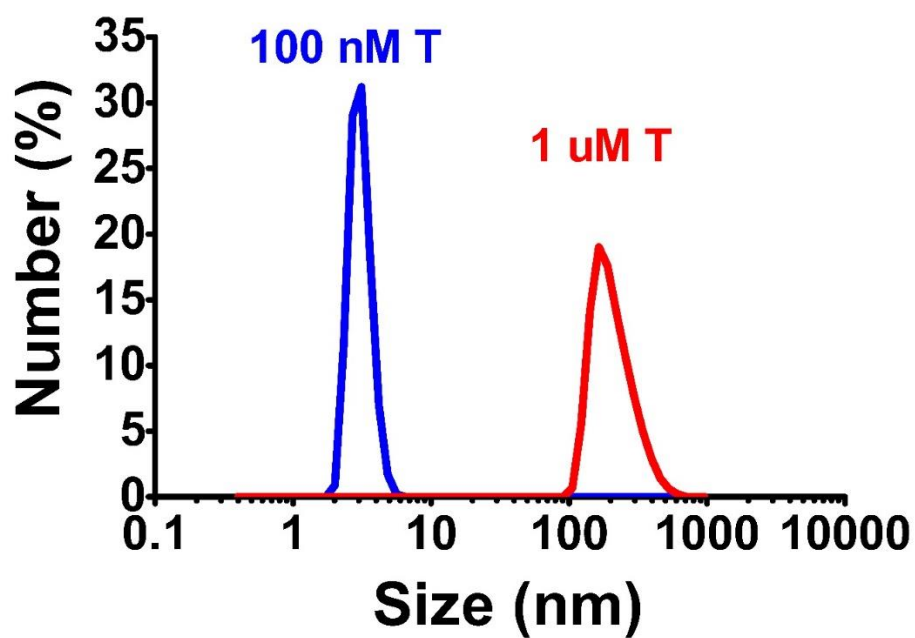


**Figure 3.5. Target molecule size distributions.** DLS measurement of the size distribution of target molecule T at the concentrations of 100 nM and 1  $\mu$ M in PBS7.

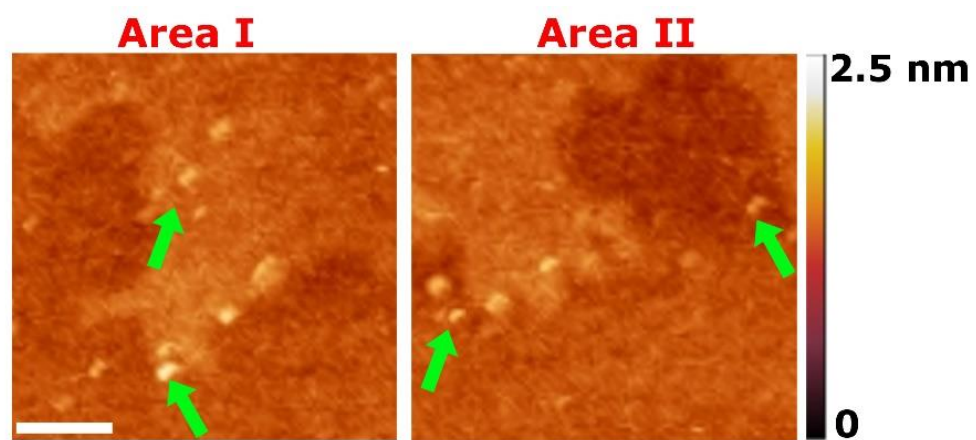


**Figure 3.6. High NND at low probe coverage.** Zoom-in images of Figure 3.2a at a probe density of  $1.83 \times 10^{10}/\text{cm}^2$ . The scale bar is 80 nm.

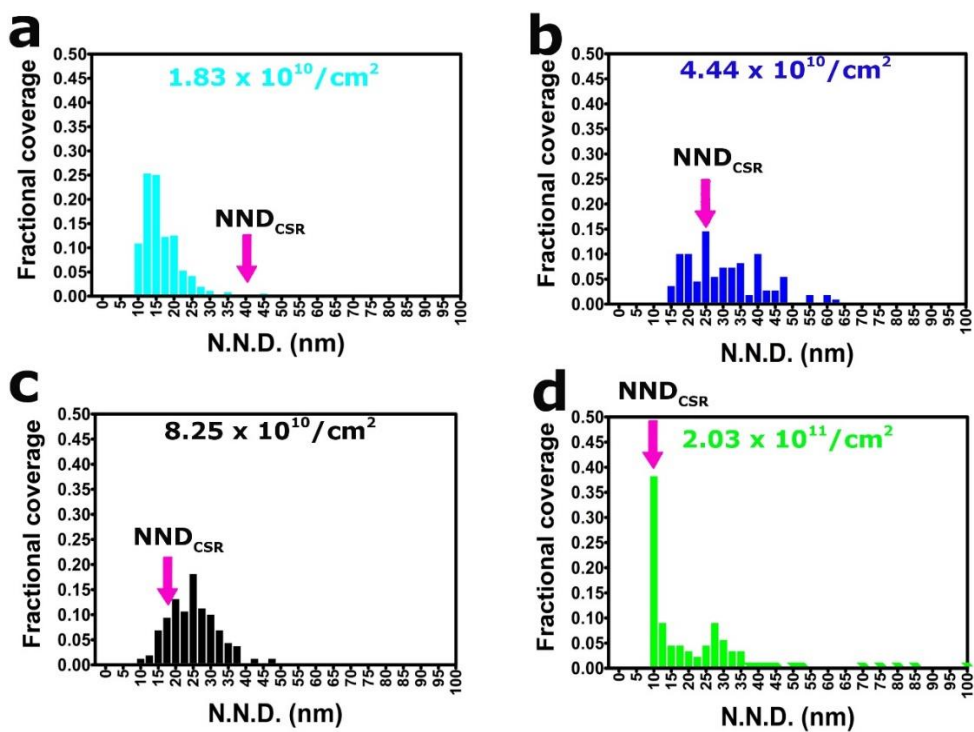


**Figure 3.7. Probe insertion process is not completely random.** Histograms of NNDs at  $1.83 \times 10^{10}$  (cyan),  $4.44 \times 10^{10}$  (blue),  $8.25 \times 10^{10}$  (black) and  $2.03 \times 10^{11}$  (green) probes/ $\text{cm}^2$ . Purple arrows indicate the expected mean NNDs of complete spatial randomness.

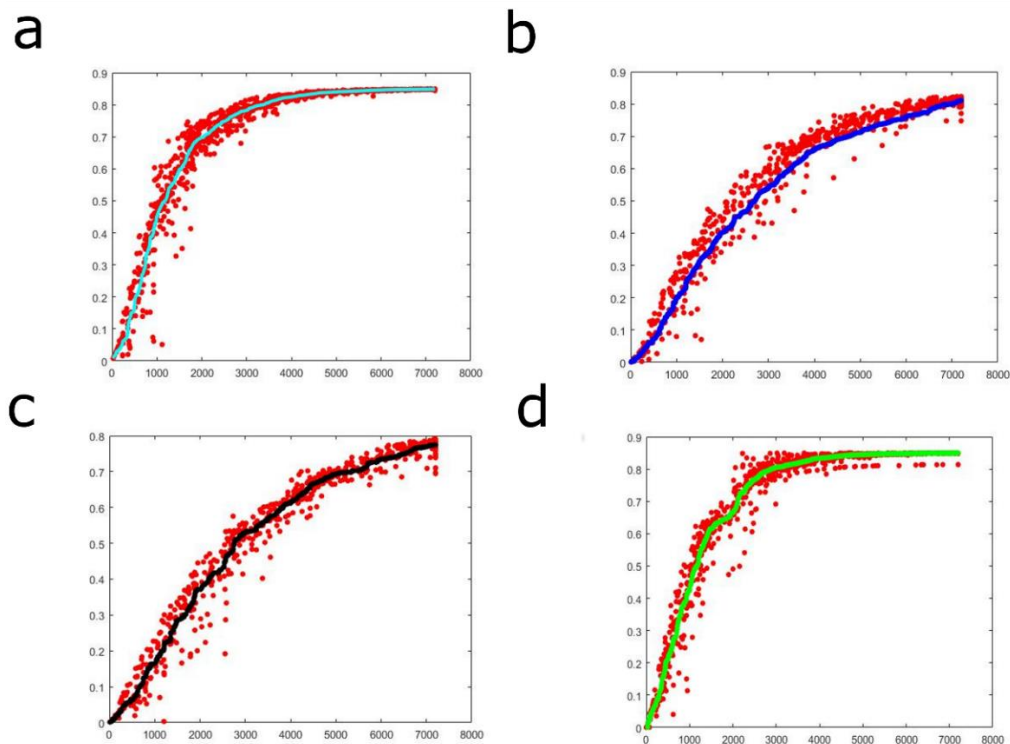


**Figure 3.8. Numerically simulated kinetic traces.** Numerical simulation of the hybridization kinetics at  $1.83 \times 10^{10}$  (cyan),  $4.44 \times 10^{10}$  (blue),  $8.25 \times 10^{10}$  (black) and  $2.03 \times 10^{11}$  (green).

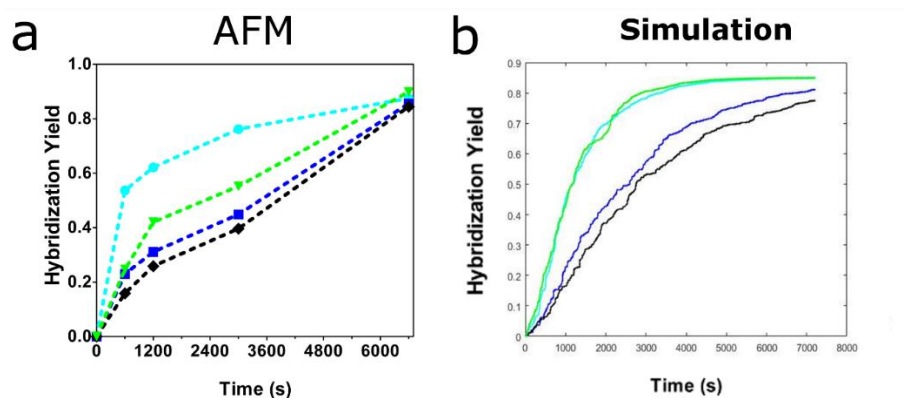


**Figure 3.9. Comparison of AFM-derived kinetics to numerical simulations.** (a) AFM-derived (Figure 2e) and (b) Numerically simulated kinetics (Figure 3c) of the biosensor surface in the presence of 100 nM target DNA at  $1.83 \times 10^{10}$  (S1, cyan),  $4.44 \times 10^{10}$  (S2, blue),  $8.25 \times 10^{10}$  (S3, black) and  $2.03 \times 10^{11}$  (S4, green).

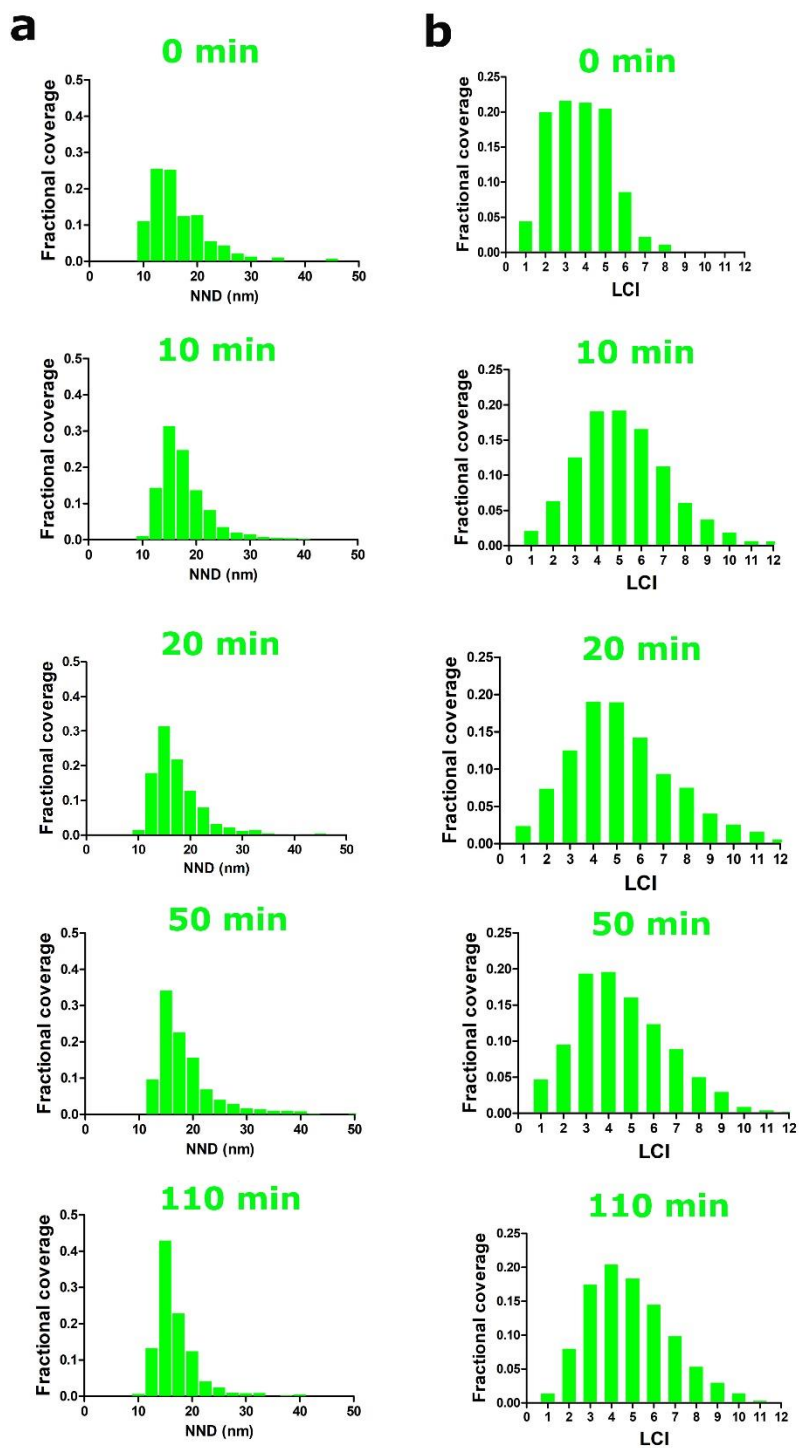


**Figure 3.10. Spatial statistical variance at different stages of hybridization.** Histograms of (a) NNDs and (b) LCIs ( $2.03 \times 10^{11}$  probes/cm<sup>2</sup>) at different time points.

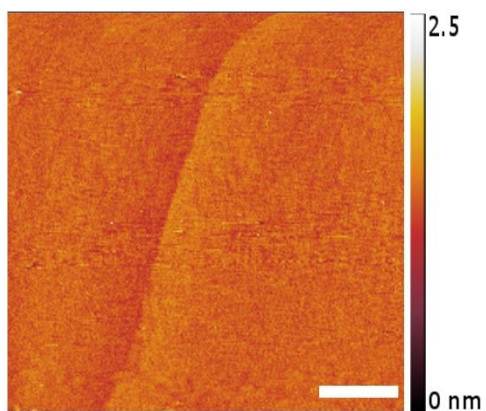


**Figure 3.11. Absence of nonspecifically adsorbed targets.** Representative AFM image of the MUUDA SAM surface (without probes) incubated with 100 nM large targets (T1) for 30 minutes. The absence of targets indicates that the non-specific adsorption is minimized. Scale bar is 100 nM.



## References

1. Rao, A. N.; Grainger, D. W., Biophysical Properties of Nucleic Acids at Surfaces Relevant to Microarray Performance. *Biomaterials Science* **2014**, *2* (4), 436-471.
2. Geiger, B.; Spatz, J. P.; Bershadsky, A. D., Environmental Sensing through Focal Adhesions. *Nat. Rev. Mol. Cell Bio.* **2009**, *10*(1), 21-33.
3. Huang, Y. F.; Liu, H. P.; Xiong, X. L.; Chen, Y.; Tan, W. H., Nanoparticle-Mediated Ige-Receptor Aggregation and Signaling in Rbl Mast Cells. *J. Am. Chem. Soc.* **2009**, *131* (47), 17328-17334.
4. Arroyo-Curras, N.; Somerson, J.; Vieira, P. A.; Ploense, K. L.; Kippin, T. E.; Plaxco, K. W., Real-Time Measurement of Small Molecules Directly in Awake, Ambulatory Animals. *P. Natl. Acad. Sci. USA* **2017**, *114* (4), 645-650.
5. Kelley, S. O., Advancing Ultrasensitive Molecular and Cellular Analysis Methods to Speed and Simplify the Diagnosis of Disease. *Accounts Chem. Res.* **2017**, *50* (3), 503-507.
6. Xi, Q.; Zhou, D. M.; Kan, Y. Y.; Ge, J.; Wu, Z. K.; Yu, R. Q.; Jiang, J. H., Highly Sensitive and Selective Strategy for Microrna Detection Based on Ws2 Nanosheet Mediated Fluorescence Quenching and Duplex-Specific Nuclease Signal Amplification. *Anal. Chem.* **2014**, *86* (3), 1361-1365.
7. Thomas, J. M.; Chakraborty, B.; Sen, D.; Yu, H. Z., Analyte-Driven Switching of DNA Charge Transport: De Novo Creation of Electronic Sensors for an Early Lung Cancer Biomarker. *J. Am. Chem. Soc.* **2012**, *134*(33), 13823-13833.
8. Cederquist, K. B.; Golightly, R. S.; Keating, C. D., Molecular Beacon-Metal Nanowire Interface: Effect of Probe Sequence and Surface Coverage on Sensor Performance. *Langmuir* **2008**, *24* (16), 9162-9171.
9. Cederquist, K. B.; Keating, C. D., Hybridization Efficiency of Molecular Beacons Bound to Gold Nanowires: Effect of Surface Coverage and Target Length. *Langmuir* **2010**, *26* (23), 18273-18280.
10. Peterson, A. W.; Heaton, R. J.; Georgiadis, R. M., The Effect of Surface Probe Density on DNA Hybridization. *Nucleic Acids Res.* **2001**, *29* (24), 5163-5168.
11. Peterson, A. W.; Heaton, R. J.; Georgiadis, R., Kinetic Control of Hybridization in Surface Immobilized DNA Monolayer Films. *J. Am. Chem. Soc.* **2000**, *122* (32), 7837-7838.
12. Ricci, F.; Lai, R. Y.; Heeger, A. J.; Plaxco, K. W.; Sumner, J. J., Effect of Molecular Crowding on the Response of an Electrochemical DNA Sensor. *Langmuir* **2007**, *23* (12), 6827-6834.

13. Herne, T. M.; Tarlov, M. J., Characterization of DNA Probes Immobilized on Gold Surfaces. *J. Am. Chem. Soc.* **1997**, *119*(38), 8916-8920.
14. Steel, A. B.; Herne, T. M.; Tarlov, M. J., Electrochemical Quantitation of DNA Immobilized on Gold. *Anal. Chem.* **1998**, *70*(22), 4670-4677.
15. Xu, F.; Pellino, A. M.; Knoll, W., Electrostatic Repulsion and Steric Hindrance Effects of Surface Probe Density on Deoxyribonucleic Acid (DNA)/Peptide Nucleic Acid (Pna) Hybridization. *Thin Solid Films* **2008**, *516*(23), 8634-8639.
16. Gong, P.; Levicky, R., DNA Surface Hybridization Regimes. *P. Natl. Acad. Sci. USA* **2008**, *105*(14), 5301-5306.
17. Pinheiro, A. V.; Nangreave, J.; Jiang, S. X.; Yan, H.; Liu, Y., Steric Crowding and the Kinetics of DNA Hybridization within a DNA Nanostructure System. *ACS Nano* **2012**, *6*(6), 5521-5530.
18. Johnson-Buck, A.; Nangreave, J.; Jiang, S.; Yan, H.; Walter, N. G., Multifactorial Modulation of Binding and Dissociation Kinetics on Two-Dimensional DNA Nanostructures. *Nano Lett.* **2013**, *13*(6), 2754-2759.
19. Josephs, E. A.; Ye, T., Nanoscale Spatial Distribution of Thiolated DNA on Model Nucleic Acid Sensor Surfaces. *ACS Nano* **2013**, *7*(4), 3653-3660.
20. Murphy, J. N.; Cheng, A. K. H.; Yu, H. Z.; Bizzotto, D., On the Nature of DNA Self-Assembled Monolayers on Au: Measuring Surface Heterogeneity with Electrochemical in Situ Fluorescence Microscopy. *J. Am. Chem. Soc.* **2009**, *131*(11), 4042-4050.
21. Li, H.; Dauphin-Ducharme, P.; Ortega, G.; Plaxco, K. W., Calibration-Free Electrochemical Biosensors Supporting Accurate Molecular Measurements Directly in Undiluted Whole Blood. *J. Am. Chem. Soc.* **2017**, *139*(32), 11207-11213.
22. Rao, A. N.; Rodesch, C. K.; Grainger, D. W., Real-Time Fluorescent Image Analysis of DNA Spot Hybridization Kinetics to Assess Microarray Spot Heterogeneity. *Anal. Chem.* **2012**, *84*(21), 9379-9387.
23. Du, H.; Disney, M. D.; Miller, B. L.; Krauss, T. D., Hybridization-Based Unquenching of DNA Hairpins on Au Surfaces: Prototypical "Molecular Beacon" Biosensors. *J. Am. Chem. Soc.* **2003**, *125*(14), 4012-4013.
24. Cao, H. H.; Nakatsuka, N.; Serino, A. C.; Liao, W. S.; Cheunkar, S.; Yang, H. Y.; Weiss, P. S.; Andrews, A. M., Controlled DNA Patterning by Chemical Lift-Off Lithography: Matrix Matters. *ACS Nano* **2015**, *9*(11), 11439-11454.
25. Fan, C. H.; Plaxco, K. W.; Heeger, A. J., Electrochemical Interrogation of Conformational Changes as a Reagentless Method for the Sequence-Specific Detection of DNA. *P. Natl. Acad. Sci. USA* **2003**, *100*(16), 9134-9137.

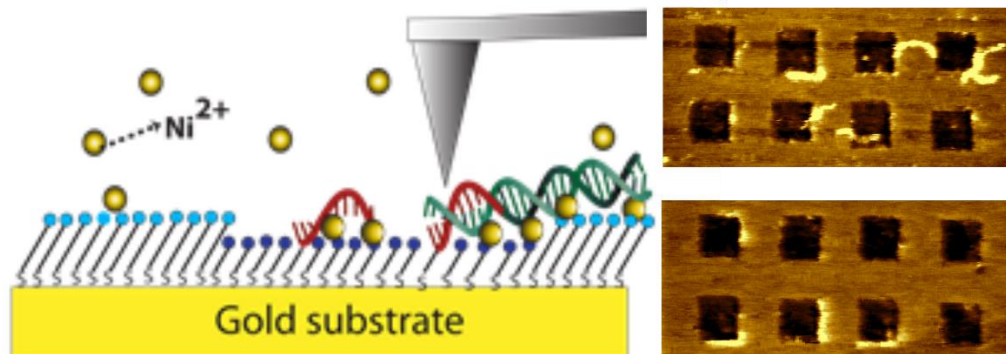
26. Vallee-Belisle, A.; Plaxco, K. W., Structure-Switching Biosensors: Inspired by Nature. *Current Opinion in Structural Biology* **2010**, *20* (4), 518-526.
27. Clavilier, J.; Faure, R.; Guinet, G.; Durand, R., Preparation of Mono-Crystalline Pt Microelectrodes and Electrochemical Study of the Plane Surfaces Cut in the Direction of the (111) and (110) Planes. *J. Electroanal. Chem.* **1980**, *107*(1), 205-209.
28. Horcas, I.; Fernandez, R.; Gomez-Rodriguez, J. M.; Colchero, J.; Gomez-Herrero, J.; Baro, A. M., Wsxn: A Software for Scanning Probe Microscopy and a Tool for Nanotechnology. *Review of Scientific Instruments* **2007**, *78* (1).
29. Jennings, A. A.; Kirkner, D. J., Instantaneous Equilibrium Approximation Analysis. *J. Hydraul. Eng-Asce.* **1984**, *110*(12), 1700-1717.
30. Cox, D. R., Regression Models and Life-Tables. *J. R. Stat. Soc. B* **1972**, *34* (2), 187.
31. Fan, C.; Plaxco, K. W.; Heeger, A. J., Electrochemical Interrogation of Conformational Changes as a Reagentless Method for the Sequence-Specific Detection of DNA. *Proc. Natl. Acad. Sci. USA.* **2003**, *100* (16), 9134-9137.
32. Abel, G. R., Jr.; Josephs, E. A.; Luong, N.; Ye, T., A Switchable Surface Enables Visualization of Single DNA Hybridization Events with Atomic Force Microscopy. *J. Am. Chem. Soc.* **2013**, *135* (17), 6399-6402.
33. Gu, Q. F.; Nanney, W.; Cao, H. H.; Wang, H. Y.; Ye, T., Single Molecule Profiling of Molecular Recognition at a Model Electrochemical Biosensor. *J. Am. Chem. Soc.* **2018**, *140* (43), 14134-14143.
34. Schwarz, G., Estimating Dimension of a Model. *Ann. Stat.* **1978**, *6* (2), 461-464.
35. Tsourkas, A.; Behlke, M. A.; Rose, S. D.; Bao, G., Hybridization Kinetics and Thermodynamics of Molecular Beacons. *Nucleic Acids Res.* **2003**, *31* (4), 1319-1330.
36. Pei, H.; Lu, N.; Wen, Y. L.; Song, S. P.; Liu, Y.; Yan, H.; Fan, C. H., A DNA Nanostructure-Based Biomolecular Probe Carrier Platform for Electrochemical Biosensing. *Adv. Mater.* **2010**, *22* (42), 4754.
37. Bizzotto, D.; Burgess, I. J.; Doneux, T.; Sagara, T.; Yu, H.-Z., Beyond Simple Cartoons: Challenges in Characterizing Electrochemical Biosensor Interfaces. *ACS Sensors* **2018**, *3* (1), 5-12.
38. Yang, L.; Zhang, C. H.; Jiang, H.; Li, G. J.; Wang, J. H.; Wang, E. K., Insertion Approach: Bolstering the Reproducibility of Electrochemical Signal Amplification Via DNA Superstructures. *Anal. Chem.* **2014**, *86* (10), 4657-4662.

## Chapter 4

# Molecular Conformations of DNA Targets Captured by Nanoarrays

When did the bright moon come to be? I raise my drink to ask the azure sky. I wonder about the palace and edifices in heaven, what year of which age do they go by tonight? I'd like to ride the wind to there, visit and return, yet I fear where such grand and fine architecture is. Must be unbearably cold because of its height. So I turn to dance among distinct light and shade, how it must appear beyond the promise of earthly delights. Soon the moon glides behind the red high-rise, and through the decorated window of the wakeful it shines. I know I shouldn't agonise over it, yet why does the moon always fuller seem at parting times? Life is full of happy reunions and parting sorrows, and the moon waxes and wanes in size. Nothing is ever perfect since the beginning of time. May we continue to survive life, so that we could the moon's loveliness share when separated by thousands of miles.

Su Shi, Lyric to the First Water Melody



**Abstract:** There is an emerging need to measure single DNA molecules deposited into supported arrays to enable a host of biotechnological applications, including single molecule sequencing, epigenetic analysis, and single-molecule biophysical measurements. In addition, it is desirable to self-assemble DNA on surfaces to form programmable nanostructures. An open question in these studies is how nanometer-scale interactions with the chemical and morphological heterogeneities of the solid support affect the properties of the DNA and how these interactions can be exploited to control their molecular properties. We generated arrays of individually-resolvable DNA molecules tethered to nanometer-scale patterns of alkanethiol monolayers that possess tailored surface heterogeneities. Using high-resolution *in situ* atomic force microscopy to probe the conformations of the DNA molecules interacting with these surface features, we found that the DNA conformations are highly sensitive to both the chemical functionality and sub-nanometer variations in the topographical height of carboxyl-terminated self-assembled monolayers onto which they were deposited. By exploiting the sensitivity of the DNA-surface interactions to the presence of divalent cations, we aligned the DNA into a range of shapes that follow the engineered chemical patterns but deviate significantly from their native conformations. Knowledge of how the nanoscale chemical functionality and morphology of arrayed surfaces impact the properties of DNA can enable effective means to control their molecular conformations at interfaces and enable new applications in single molecule measurement and DNA nanotechnology.

## 4.1. Introduction

An urgent need in single molecule measurement is to organize individual DNA molecules in an array format<sup>1</sup> to improve the throughput of measurement in a host of applications, such as parallel single molecule biophysical measurement,<sup>2</sup> single molecule sequencing<sup>3</sup> and epigenetic analysis.<sup>4-5</sup> An open question is how the interactions between DNA and the solid support of the array affect the conformations, molecular recognition, and other biophysical behaviors of the DNA molecules, which are intimately linked to the sensor device performance.<sup>6</sup> Even a tailored surface could have anomalously strong adsorption sites that significantly alter the dynamics of macromolecular adsorbates.<sup>7-9</sup> Therefore, patterned surfaces, which possess compositional heterogeneities (non-uniform lateral distributions of surface functionalities and probe molecules)<sup>10-11</sup> as well as morphological heterogeneities (surface roughness),<sup>12</sup> may have difficult-to-predict and pronounced effects on these molecular properties. Such heterogeneities have been recognized as a contributing factor to the limited reproducibility of many DNA microarrays<sup>6, 13</sup> and could have an even more pronounced impact on single-molecule nanoarrays.<sup>1, 4, 12, 14</sup>

There exist two major gaps toward a fundamental understanding of the molecular properties of DNA on nanoscale surface patterns. First, to understand the interactions between surface patterns and DNA molecules, the morphological and compositional heterogeneities need to be controlled at the relevant spatial scales, as the relevant length scales of surface interactions are typically less than a few nanometers.<sup>15</sup> Common patterning techniques<sup>16-18</sup> lack the ability to define the morphology and the lateral distribution of surface chemical functionalities with this level of precision, and hence the resulting arrays may be too complex for fundamental investigations.<sup>6</sup> Second, conventional surface characterization techniques, such as surface plasmon resonance,<sup>19</sup> X-ray photoelectron spectroscopy,<sup>10</sup> electrochemical measurements,<sup>20-21</sup> while capable of detecting the amount of targets/probes, have neither the spatial resolution nor the specificity to directly probe nanometer-scale interactions or their effects on microscopic processes such as adsorption, desorption, diffusion, and molecular recognition.<sup>22-23</sup> Schwartz and coworkers' single-molecule fluorescence microscopy studies of the interfacial dynamics of individual biomacromolecules highlighted the significance of heterogeneous surface interactions.<sup>7-9</sup> For instance, they found that the surface-mediated unfolding of proteins may not occur at random surface sites, and instead the molecules may undergo long-range diffusion before encountering isolated nanoscale sites where denaturation occurs. The sites, present on unpatterned as well as patterned surfaces, may originate from non-uniform lateral spatial patterns of surface chemical functional groups, varied orientations of these groups, or nanoscale roughness. However, the exact origin

of such nanoscale anomalous sites is difficult to elucidate even with super-resolution localization, as fluorescent labeling of such sites is typically not practical and the spatial resolution (~20-50 nm) remains insufficient. Therefore, it would be informative to probe how DNA interact with the patterned surface features using *in situ* AFM imaging, which is label-free and in principle capable of imaging both surface-tethered DNA molecules and the surface with a lateral resolution of a few nanometers or higher and a vertical resolution of a few angstroms.

We seek to understand the roles of surface heterogeneities in DNA layer end tethered to self-assembled monolayers on single-crystal Au (111) (Figure 4.1).<sup>24</sup> These surfaces are among the most well-defined biointerfaces and have broad utility in biosensors and micro/nanoarrays.<sup>20, 25-28</sup> Recent studies suggest that the surface heterogeneities in the DNA monolayers, such as non-uniform probe densities, may affect the sensitivity and reproducibility of these DNA biosensors and arrays.<sup>29-32</sup> In this study, we have conducted high resolution, label-free, single molecule imaging of DNA molecules interacting with surface chemical patterns with precisely tailored compositional as well as morphological heterogeneities.<sup>33</sup> The nanografting technique used in this study (see Figure 4.1 for details of this protocol) can routinely generate patterns of highly ordered self-assembled monolayers with a lateral dimension below ten nanometers, an edge width of only a few nanometers or less, and topographical height controlled with an angstrom level precision. In addition, the nanoarrays incorporate spatially isolated DNA probes that can capture larger DNA targets and place them in close proximity to the nanoengineered surface features.<sup>14, 34-35</sup> We found that the conformation of surface-immobilized DNA may be highly sensitive to the compositional and morphological heterogeneities of the surrounding chemical pattern in the presence of divalent cations,<sup>25-28, 36-38</sup> the DNA target molecules were quantitatively observed to preferentially adhere to the boundary between two carboxyl terminated monolayer domains that differ by only half a nanometer in topographical height. The study raises new questions on how target-capture in an array may be affected by such surface heterogeneities. Moreover, we show that these nanoscale interactions can be exploited to control the conformation of DNA molecules and align the molecules into novel shapes. The ability to selectively capture long DNA in spatially addressable arrays and achieve elaborate control over the molecular conformations may enable new applications in single molecule measurement and microarrays. In addition, understanding and controlling the interactions between DNA and surface patterns at the single molecule level can facilitate the self-assembly of complex DNA nanostructures on solid surfaces.<sup>39</sup>

## 4.2. Methods and materials

### 4.2.1. Materials

Gold wire (99.99%, 1 mm diameter) was purchased from Scientific Instrument Services, Inc. 16-Mercaptohexadecanoic acid (MHDA), 11-Mercaptoundecanoic acid (MUDA) and 16-thiohexadecanol were purchased from Santa Cruz Biotechnology, Inc. NiAc<sub>2</sub>, MgAc<sub>2</sub> were purchased from Sigma Aldrich. Tris-acetate-EDTA (TAE) and dithiothreitol (DTT) were used without further purification. Only ultrapure water (>18 MΩ·cm at 21°C) generated from a Barnstead Diamond Nanopure water purification system was used.

### 4.2.2. Oligonucleotides

The undecyldisulfide-DNA (SF-17) was reduced by overnight incubation in an aqueous buffer solution containing a 1M DTT and was purified using Illustra NAP-5 columns from GE Healthcare Life Sciences (Pennsylvania, USA). After reduction and purification, thiolated DNA probes were stored in TAE buffer, and the container was backfilled with nitrogen gas and stored at -20°C until use. DNA targets that have a 372 bp double-stranded segment and a 24 *nt.* single stranded tail were prepared by conventional PCR amplification from the M13 bacteriophage genome, as described in our previous work.<sup>33</sup> All oligonucleotide sequences are summarized in Table 4.1.

### 4.2.3. Surface monolayer preparation

A single-crystal gold bead substrate was prepared in house and used for all AFM experiments. The gold bead substrate was prepared following a standard protocol.<sup>2</sup> The gold bead substrate was cleaned by thoroughly rinsing with ultrapure water and organic solvents, followed by 20 min immersion in hot nitric acid. The gold substrate was then thoroughly rinsed with ultrapure water and annealed with a hydrogen flame, and then placed into 2mM alkanethiol solution at room temperature for overnight. Following the SAM assembly, the gold substrate was thoroughly rinsed with in 9:1 ethanol:acetic acid and ultrapure water.

### 4.2.4. Atomic force microscope and nanografting

An Agilent 5500 atomic force microscope (Keysight Technologies, Santa Rosa, CA, USA) was used for all experiments. SNL-10 tips (Bruker, Bellerica, MA, USA) with spring constants of approximately 0.2-0.4 N/m and a resonant frequency of approximately 16 kHz in liquid were used for all experiments. During AFM scanning, topographical, amplitude, and phase channels were simultaneously recorded. Equal volumes of TAE buffer containing 5-20nM of thiolated DNA probe and ethanol containing 20-400 μM of MUDA were added into a custom-made liquid cell for nanografting. Nanoshaving protocol was



performed as previously described: briefly, selected regions of the host self-assembled monolayer were removed by applying the lowest forces to the AFM probe using the PicoLith module of PicoView to achieve high-quality patterns into the host SAM. Generally, the force thresholds range from 100 nN and 200 nN.

#### 4.2.5. DNA surface hybridization

Prior to the addition of hybridization buffer, the patterned surfaces were repeatedly rinsed with STAE buffer (saline Tris-acetate-EDTA: 200 mM NaCl, 40 mM Tris acetate, 5 mM EDTA, pH 8.3) to remove any Ni(II) cations on the surface. The patterned surfaces were then exposed to the target DNA (200nM) in a hybridization buffer containing 1.0 M NaCl, 1X TAE, and 1.0 mM SDS (sodium dodecyl sulfate) for a predetermined amount of time, after which the surface were thoroughly rinsed three times with STAE and placed under the Ni(II) imaging buffer (5mM Ni(II) in 0.1x TAE).

#### 4.2.6. AFM image analysis

All experiments were repeated three times. AFM scanning was performed in at least four different areas each time and a total number of 120 DNA molecules were observed. Topographical heights and spatial organizations of DNA molecules were directly extracted from AFM images using Gwyddion image analysis software (<http://gwyddion.net/>) and statistical analysis were performed using MATLAB script developed in our previous work.

#### 4.2.7. Nonspecific adsorption

As a control experiment, we explored the extent of non-specific adsorption of DNA on highly ordered self-assembled monolayers on single-crystal Au(111) surface. After exposing an unpatterned 16-Mercaptohexadecanoic acid SAM on a single crystal Au(111) surface to a 1x TAE buffer solution containing 200 nM dsDNA targets, rinsing with the surface with SATE buffer, and imaging with AFM under Ni<sup>2+</sup> imaging buffer that can immobilize DNA, we observed few if any DNA over many microns (Figure 4.12). Consistent with our previous study, the absence or low level of non-specific adsorption shows that the unpatterned host SAM is highly ordered and does not possess a significant level of surface defects that can trap DNA non-specifically. A highly ordered SAM enables a precise introduction of surface heterogeneities using nanografting.

### 4.3. Results and discussion

Our study builds upon two techniques that we developed previously: single molecule AFM imaging of DNA on dynamically switchable surfaces<sup>33</sup> and AFM nanografting of single DNA probe molecules.<sup>35</sup> Although conventionally atomic force microscopy (AFM) can only measure the surface morphology/roughness and is incapable of resolving single DNA molecules on these surfaces, we have

used dynamically switchable surface interactions that allow us to repeatedly image single DNA molecules with a lateral resolution of a few nanometers. The interaction between a surface-immobilized DNA molecule and carboxyl-terminated alkanethiol self-assembled monolayers (SAMs) can be tuned when exposed to divalent cations: in the absence of divalent cations, the anchored DNA molecules are lifted up from the negatively charged surface and free to interact with other biomolecules in the solution; with divalent cations in solution, the DNA molecules bound strongly to the surface where they can be imaged with high resolution by AFM. The other key technique is AFM nanografting of spatially isolated DNA probe molecules. AFM nanografting can generate nanoscale surface chemical patterns by applying a high load on the AFM tip to selectively remove molecules in a host self-assembled monolayer and letting thiol molecules from the solution immediately fill the exposed area. While the AFM tip normally does not allow AFM nanografting to pattern single molecules due to the finite size, our previous work enabled nanografting to pattern features containing spatially resolved single DNA molecules by mixing thiolated DNA molecules with spacer thiol molecules that can compete for binding to the exposed Au surface.<sup>40</sup> We are able to generate model nanoscale structures where the surface-DNA interactions can be tailored by nanografting thiolated probes along with carboxyl-terminated alkanethiols.

We carried out nanografting in a solution containing 24 nucleotide (nt.) single-stranded DNA (ssDNA) molecules that each possessed a  $-C_{11}H_{22}SH$  tether, and 11-Mercaptoundecanoic acid (MUDA) spacer molecules into a pre-assembled host SAM composed of 16-Mercaptohexadecanoic acid (MHDA) (Figure 4.1a, b). AFM images illustrated that after nanografting, depressed areas that are  $0.5 \pm 0.1$  nm deep appeared (Figure 4.2 and Figure 4.4). These depressions correspond to MUDA SAM, which is approximately 0.6 nm thinner than the host MHDA SAM. Protrusions that are  $0.7 \pm 0.2$  nm taller (see histogram in Figure 4.3) than the depressed regions are also observed in the presence of  $Ni^{2+}$  (arrows in Figure 4.4a). These protrusions correspond to patterned ssDNA probe molecules that have the thiolated end anchored to the single-crystal Au(111) surface and the DNA segment pinned atop the carboxyl terminated monolayer (Figure 4.1).<sup>14, 33</sup> Then we exposed the surface pattern to a 1x Tris acetate EDTA (TAE, 40 mM Tris, 20 mM acetic acid, and 1 mM EDTA) buffer containing 100 nM of DNA “target” molecules for 30-60 min (Figure 4.1c). Each of the target molecules has a 372 bp double-stranded DNA (dsDNA) segment and a 24 nt. single-stranded tail that is complementary to the probe DNA (see Supporting Information). The surface was imaged under an imaging buffer that contained 5 mM  $Ni^{2+}$  and 4 mM Tris acetate (Figure 4.1d) after it was rinsed with a TAE buffer. The AFM scanning (Figure 4.4b) shows rod-like features that are  $120 \pm 20$  nm long and 2.0 nm high (over 100 molecules were analyzed). As we have showed in previous studies,<sup>33, 41</sup> these features correspond to dsDNA molecules attached to the SAM surface. In a

control experiment where a nanografted pattern that is free of DNA capture probes was exposed to the same DNA target solution, the absence of DNA targets on the surface (Figure 4.5) confirming that the patterned DNA probes can capture the target DNA through base-pairing interactions. Therefore, the surface pattern can function as a nanoarray that can not only capture DNA targets but also enable single molecule AFM imaging that can characterize nanoscale chemical and morphological heterogeneities.

Interestingly, a number of DNA molecules were aligned along the edges of the squares (Figure 4.4b). The preferential adhesion to the boundaries between MUDA and MHDA SAMs, which have the same surface functional groups but differ by  $\sim 0.6$  nm in topographical height (Figure 4.2), reveals the impact of morphological heterogeneity. However, the degree of the preference is likely affected by kinetic trapping of DNA in the presence of  $\text{Ni}^{2+}$ ,<sup>42</sup> which induces strong surface immobilization. To evaluate if the edge sites are indeed the energetically preferred sites for DNA, we adopted an “annealing” protocol that gradually raise the strength of the surface interactions to allow the DNA molecules to explore the different binding sites and settle into low energy configurations. The strength of the surface interactions was varied by adjusting the buffer composition: in a monovalent buffer, the end-tethered DNA molecules interact only weakly with the surface because both the DNA and the surface are negatively charged; divalent cations induce attractive interactions between the DNA molecules and the carboxyl terminated surface.<sup>33</sup> In a work under preparation, we also found that the interactions between DNA and the carboxyl surfaces are significantly weaker in  $\text{Mg}^{2+}$  than those in  $\text{Ni}^{2+}$ , a trend that was also observed for DNA adsorbed on mica surfaces.<sup>43</sup> Therefore, to gradually increase the binding strength, we first added 1 mM  $\text{Mg}(\text{II})$  to the TAE buffer every 2 minutes, up to 10 mM  $\text{Mg}(\text{II})$  in total, and then replaced the TAE buffer with an imaging buffer containing 5 mM  $\text{Ni}^{2+}$ . The fraction of the DNA contour length that adheres to the edge increased dramatically, from 29% to 89% (Figure 4.4c). The preferential binding is remarkable considering that it is impossible for many DNA targets to fully align with the edges as many of the DNA probes are located away from the edges. Moreover, the straight conformation is a sharp departure from the semi-flexible worm-like chain conformation that is observed in the solution phase as well as on unpatterned surfaces.<sup>41-42</sup> The results confirm that compared to flat surfaces, DNA molecules near the edge are stabilized by strong interactions.

The origin of the stronger attractive interactions at MUDA/MHDA boundaries when exposed to divalent cations is an open question. The attractive interactions between DNA and a flat carboxyl terminated SAM are thought to be induced by divalent cations that sandwich between the two negatively charged objects. Such salt bridging effects may result from electrostatic (counterion-correlation)<sup>44-45</sup> or chemical forces (the metal ions

likely form coordination bonds with both the phosphate backbone of the DNA and the carboxylate functional groups on the surface). Regardless of the origin, the divalent cations must be within less than a few angstroms away from the functional groups for such attractive interactions to occur. The short length scale of these interactions explains why the attractive interactions at MUDA/MHDA boundaries are stronger than those on a flat carboxyl surface; additional divalent cations can bridge DNA and the carboxylate groups at the top of the edge due to the curvature of DNA, increasing the interactions between DNA and the MUDA/MHDA domain boundary (Figure 4.4e).

Another possible origin for the preferential binding at the MUDA/MHDA boundary is the partial exposure of the hydrophobic alkyl chains of MHDA, because MHDA is 5 methylene groups longer than MUDA. Hydrophobic surfaces are known to favour the adsorption of DNA.<sup>46</sup> To see if hydrophobic interactions at the edge alone are responsible for the preferential binding of DNA, we used a host SAM of 16-Mercaptohexadecanol (MHD), which has an identical hydrocarbon chain and a hydroxyl terminal group that does not strongly interact with divalent cations (Figure 4.6). An AFM image of the pattern revealed DNA probe features as well as depressed MUDA squares that are 0.3 nm deep (Figure 4.7), which is smaller than the physical height difference between the MUDA and MHD SAMs,  $\sim 0.6$  nm. The smaller topographical contrast is attributed to the difference in how the two SAMs interact with the AFM tip, which is terminated with a negatively charged SiO<sub>2</sub> layer. Compared to the neutral MHD SAM, the negatively charged MUDA SAM has a stronger repulsive interaction with the AFM tip. The AFM image of the surface after exposure to dsDNA target molecules showed protrusions that are  $1.8 \text{ nm} \pm 0.2 \text{ nm}$  high and  $50 \text{ nm} \pm 20 \text{ nm}$  long (see histogram in Figure 4.8) in the nanografted MUDA regions. These protrusions are too high and too long to be single-stranded DNA probes on MUDA (see Figure 4.4a and ref.33). Instead, the height corresponds to that of a dsDNA target as shown in previous studies.<sup>33, 41</sup> Unlike Figure 4.4c, the molecular features in Figure 4.6a and Figure 4.6b have no strong preference to adhere to the MUDA/MHD boundaries. In addition, unlike those in Figure 4.4b and 4.4c, the lengths of the features are significantly below the full contour length, 131 nm. Similar partial features of dsDNA were observed in previous AFM studies<sup>14, 47</sup> and indicate that the molecule is only partially pinned to the surface and the rest is too mobile to be imaged (Figure 4.6c). Hydroxyl terminated SAMs do not immobilize DNA at the open circuit potential<sup>14, 47</sup> and the  $100 \text{ nm} \times 100 \text{ nm}$  MUDA squares may be too small to immobilize the entire length of a target DNA, one end of which that is hybridized with a DNA probe molecule inside a square (Figure 4.6c). Overall, the results suggest that the hydrophobic interactions at the MUDA/MHD boundaries alone are not sufficient for DNA immobilization. Hence, carboxyl groups at the top of the edge are responsible for the preferential binding of DNA to MUDA/MHDA boundaries (Figure 4.4c).

In the development of single molecule nanoarrays, the DNA molecules need to be not only patterned in a spatially addressable manner but also stretched and aligned to localize specific sequences,<sup>48-49</sup> DNA binding proteins<sup>50</sup> or epigenetic markers along the length. Fluid flow-based methods<sup>2, 51-52</sup> can align DNA along only a single direction. We hypothesized that strong binding of DNA along the edges of MUDA/MHDA patterns may be utilized to control the orientations of DNA molecules. We nanografted parallel long stripes of MUDA and ssDNA probe molecules into a host MHDA SAM matrix. Then we exposed the surface to a buffer containing the DNA target and used the aforementioned annealing procedure to progressively increase the interaction between the DNA and the surface. The AFM images showed channels that are 50 nm wide and 0.7 nm deep, as well as chains that are 1.1 nm higher than the MHDA regions, *i.e.*, 1.8 nm higher than the MUDA regions (Figure 4.9a. See also Figure 4.10a for patterned channels imaged prior to hybridization with the target dsDNA). These features resemble those in Figure 4.4c and suggest that DNA align to the patterns in a manner dictated by the geometry of the nanografted shapes. In a separate experiment, we incubated the nanografted MUDA/ssDNA patterns with longer DNA targets (1000 bps) containing a short, complementary ssDNA tail (Figure 4.10b). The results also indicated a clear preference for the DNA to be parallel to the edges.

Next, we explored if the MUDA/MHDA boundaries can be utilized to align DNA along arbitrary directions on the surface by fabricating hollow squares and hollow triangles of ssDNA probes and MUDA within a host MHDA SAM (Figure 4.9c and 4.9d). The AFM images showed chains that are 1.5 nm higher than MHDA regions and 2.0 nm higher than MUDA regions. Indeed, many of the DNA molecules align along the edges of the square and triangular shapes. Notably, some of the target DNA molecules appear to be crowded out of the pattern and are instead deposited on the MHDA SAM, possibly due to a higher density of DNA probes that can capture the DNA targets. Although further work optimizing nanografting and annealing conditions would be needed for more effective molecular alignment, the results here clearly indicate the potential of using surface chemical patterns to align DNA molecules into arbitrary nanoscale conformations.

#### 4.4. Conclusion and outlook

Single molecule, high resolution imaging of model nanoarrays has revealed surprising effects of nanoscale surface chemical functionality and morphology on the molecular behaviors of DNA. Future studies that investigate how such interactions impact the kinetics of DNA hybridization may help optimize molecular recognition in microarrays/nanoarrays. The combination of AFM, which can produce precisely tailored chemical patterns and image immobilized DNA and surface defects with high spatial resolution, with single molecule fluorescence microscopy, which has the temporal resolution to probe the

interfacial dynamics, may become a particularly powerful approach. On a practical level, our approach combines the ability to align long DNA molecules with a spatially addressable nanoarray format. DNA targets may be site specifically captured using patterned oligonucleotides, and elaborate control over the shape and orientation of DNA molecules can be achieved with the chemical patterns. In addition to enabling nanoarray measurements, the knowledge in how DNA interact with surface chemical patterns on a solid support could also aid in the development of novel complex DNA nanostructures on surfaces. Although patterning complex DNA structures on a solid support has attracted notable interest because of potential applications in nanophotonics, nanoelectronics, and nanoarray detection, existing efforts to assemble complex DNA structures on a solid support have been hindered by the limited control over the interaction between DNA and the surface.<sup>39, 53-55</sup> *E.g.*, the compositional heterogeneity of the mica substrate used for those studies was found to be responsible for low reproducibility in surface assembled structures.<sup>39</sup> Our approach may help advance the self-assembly of DNA on surfaces by enabling precise surface patterns that have more predictable and tunable interactions with DNA. Our approach to overcoming kinetic traps through dynamically adjusting DNA-surface interactions may serve as a general strategy that can reduce defect formation in self-assembly of complex DNA structures on surfaces.

**Table 4.1.** Summary of experimentally measured oligonucleotide sequences.

Name	DNA Sequence & Modifications
Sf- Prime396	5'-ACCTTATGCGATTTTAAGAACTGG-3'
Sf- DraPrime +Tail	5'- CGTACTGACTGCTCACGAGGTAGC/iSpC3/TCTGAACTGT TTAAAGCATTTGAGGG-3'
SF-17	5'-GCTACCTCGTGAGCAGTCAGTACGTTTTT-3'/C11
M13	5'-CGTACT GACTGC TCACGA GGTAGC TCTGAA CTGTTT AAAGCA TTTGAG GGGGAT TCAATG AATATT TATGAC GATTCC GCAGTA TTGGAC GCTATC CAGTCT AAACAT TTTACT ATTACC CCCTCT GGCAA ACTTCT TTTGCA AAAGCC TCTCGC TATTTT GGTTTT TATCGT CGTCTG GTAAAC GAGGGT TATGAT AGTGTT GCTCTT ACTATG CCTCGT AATTCC TTTTGG CGTTAT GTATCT GCATTA GTTGAA TGTGGT ATTCCT AAATCT CAACTG ATGAAT CTTTCT ACCTGT AATAAT GTTGTT CCGTTA GTTCGT TTTATT AACGTA GATTTT TCTTCC CAACGT CCTGAC TGGTAT AATGAG CCAGTT CTTAAA ATCGCA TAAGGT-3'

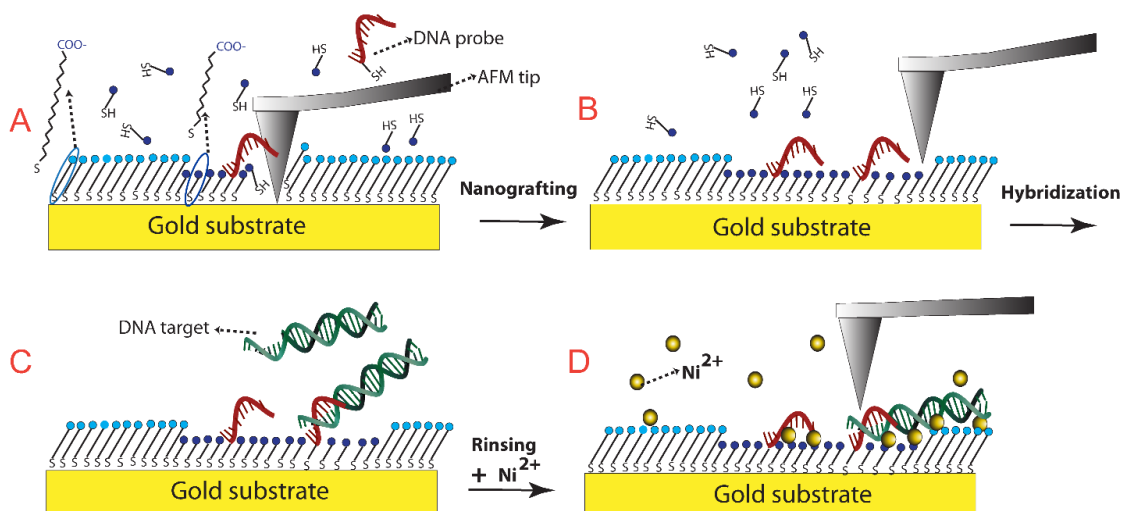


**Figure 4.1.** Schematic illustration of nanografting surface chemical patterns with DNA probes and capture of DNA targets. (a) A large force was applied on the AFM tip to displace the thiol molecules in the MUDA SAM on an Au(111) substrate. (b) The thiol molecules in the solution, 24 nt ssDNA with  $-C_{11}H_{22}SH$  tethers and MUDA form a mixed monolayer on the exposed gold surface. (c) The ssDNA molecules (DNA probes) can capture double-stranded DNA with a single-stranded segment. Hybridization was carried out in a monovalent cation buffer. (d) The addition of a divalent cation, such as  $Ni^{2+}$ , can immobilize the DNA and allow high resolution, single molecule AFM imaging.



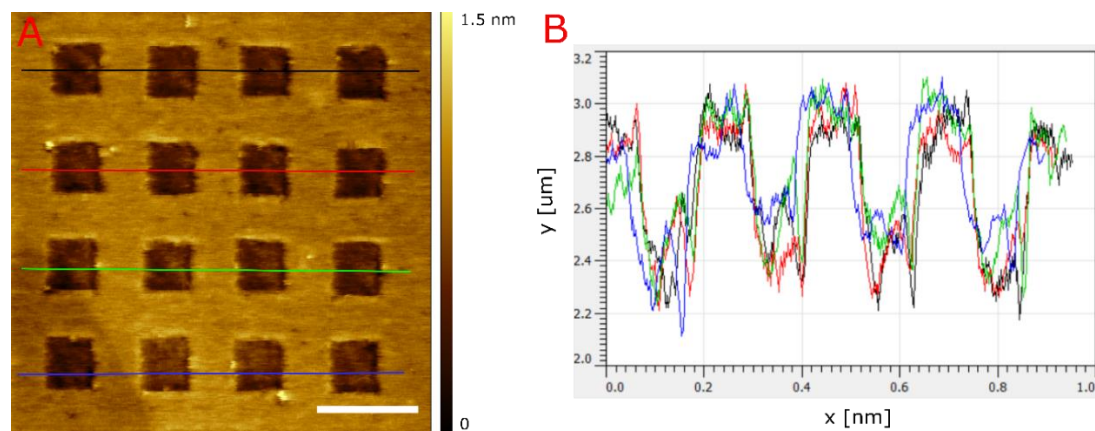


**Figure 4.2.** Representative AFM image of nanografted MUDA squares in a MHDA host SAM. The scale bar is 200 nm. The cross-sectional profiles show that the squares are  $\sim 0.6$  nm deep.

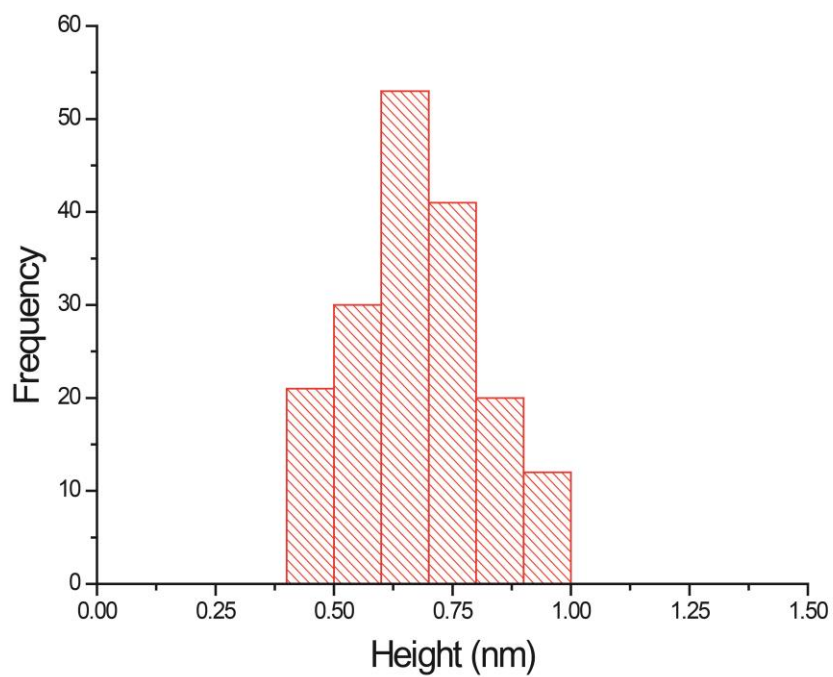


**Figure 4.3.** Histogram of the height distribution for ssDNA probe molecules in nanografted MUDA squares in MHDA host SAM. The DNA probes are  $0.7 \pm 0.2$  nm taller than the depressed regions.

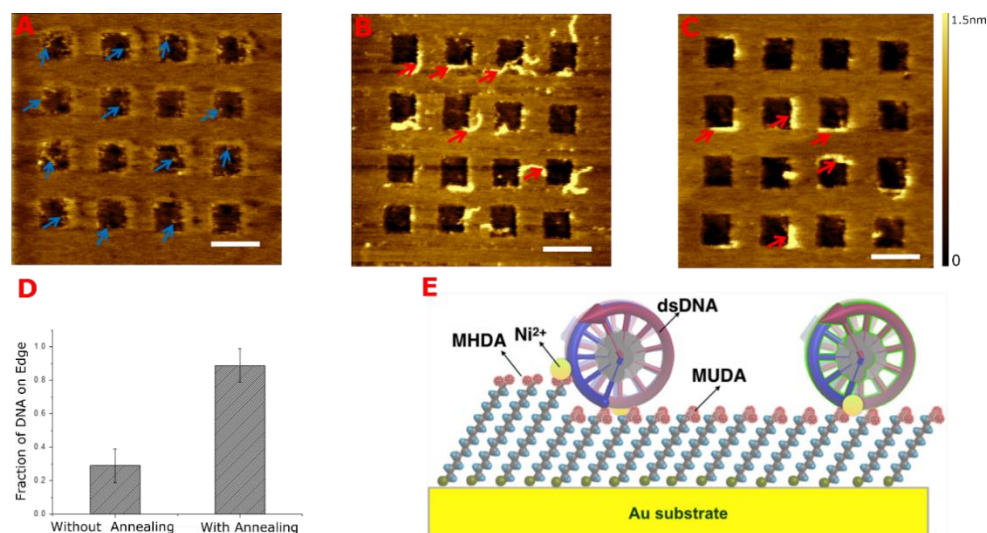


**Figure 4.4.** (a) AFM topographical image of nanografted DNA pattern before target capture. The squares are nanografted features containing MUDA and ssDNA probes (protrusions marked by blue arrows). (b) AFM image of an array that was exposed to dsDNA targets. Images were acquired under 5 mM Ni<sup>2+</sup> in a 0.1X TAE buffer solution by tapping mode AFM. Red arrows mark some of the features corresponding to captured targets. (c) AFM image of captured DNA targets that were immobilized using an annealing procedure: 1 mM Mg(II) was added to the TAE buffer every 2 min, up to 10 mM Mg(II) in total. The nanoarray was then transferred to an imaging buffer (5 mM Ni(II) buffer). The scale bar is 200 nm. (d) The fractional length of DNA adhering to MUDA/MHDA boundaries without and with the annealing step, the error bar is the standard deviation of the average fractional lengths of 8 separate AFM images containing ca.120 dsDNA. (e) Schematic showing possible interactions between DNA and a MUDA/MHDA domain boundary. The stronger adhesion to the edge is hypothesized to originate from additional salt bridging interactions at the top of the edge.

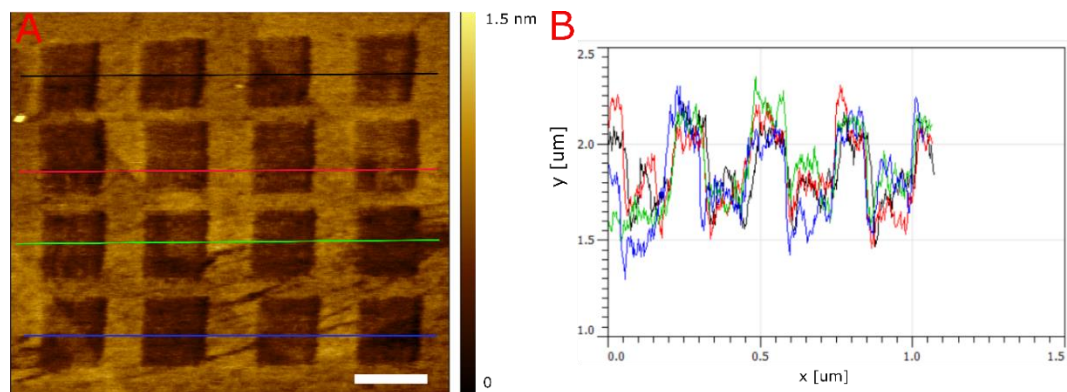


**Figure 4.5.** (a) AFM image of nanografted MUDA squares, which have no DNA probes, in MHDA host SAM after exposure to a 100 nM dsDNA target solution for 60 min. The lack of molecular-sized surface features inside the MUDA squares indicates that there is no nonspecific binding of DNA. The scale bar is 200 nm. (b) The cross-sectional profiles show that the squares are  $\sim 0.6$  nm deep.

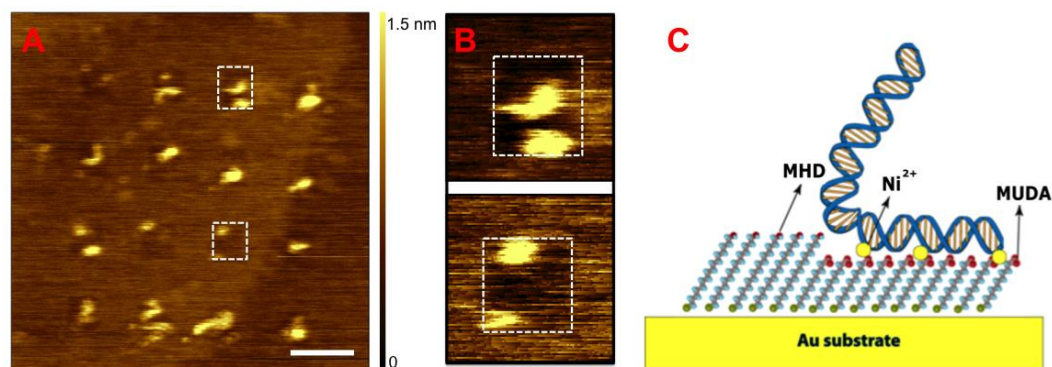


**Figure 4.6.** (a) AFM image of dsDNA targets captured by a nanoarray of MUDA in a host SAM of Mercaptohexadecanol (MHD),  $\text{HS}(\text{CH}_2)_{16}\text{OH}$ . The protrusions, which are 2 nm high, correspond to double-stranded DNA molecules. (b) Zoom in images of nanografted areas in (a). The dotted squares are used to outline the nanografted squares. (c) Schematic of DNA interacting with nanografted boundary of MUDA and MHD. The dsDNA target was immobilized by  $\text{Ni}^{2+}$  on MUDA. However, because  $\text{Ni}^{2+}$  cannot bind to MHD, the segment that is over MHD is not immobilized and hence is not imaged by AFM. Scale bar is 200 nm.

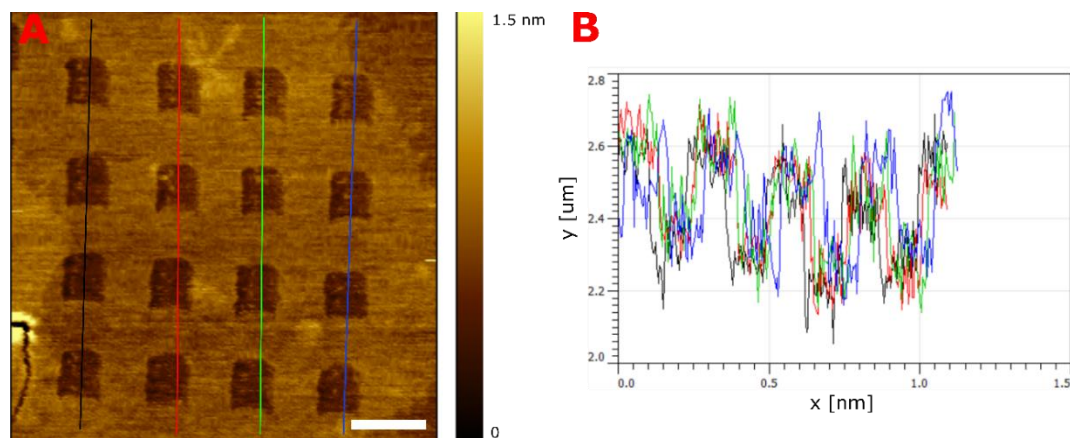


**Figure 4.7.** (a) Representative AFM image of nanografted MUDA squares with DNA probes. The image was acquired under 1:1 Ethanol/TAE buffer solution (the solution used for nanografting). (b) Cross-sectional profiles show that the squares are  $\sim 0.2$ - $0.3$  nm deep. The scale bar is 200 nm.

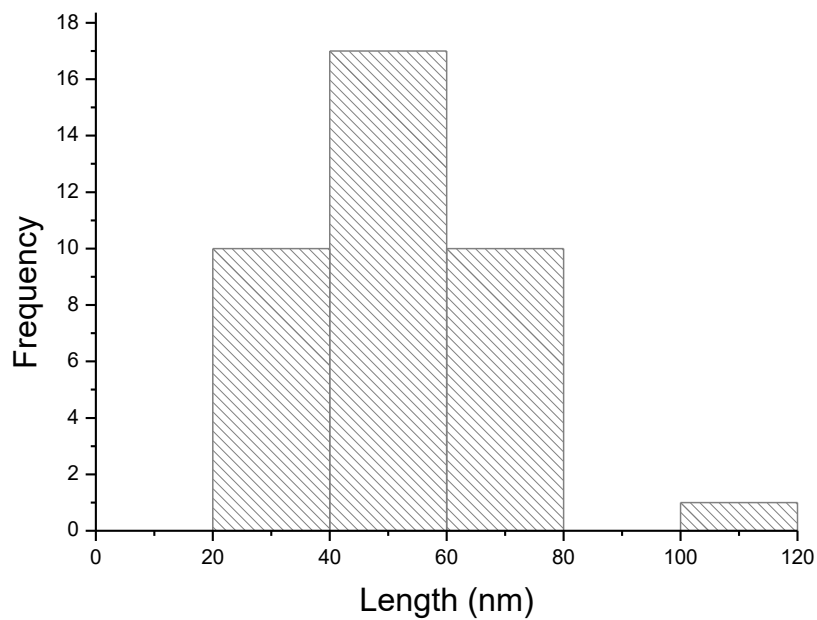


**Figure 4.8.** Histogram of the immobilized lengths of dsDNA on MUDA/MHD patterns. The average length, 50 nm, is much shorter than the full contour length of DNA, which is about 130 nm. It indicates that only a part of the molecule is pinned to the surface and the rest of the DNA is mobile and does not appear in AFM imaging, since the dsDNA cannot be immobilized on the MHD SAM, which is hydroxyl terminated.

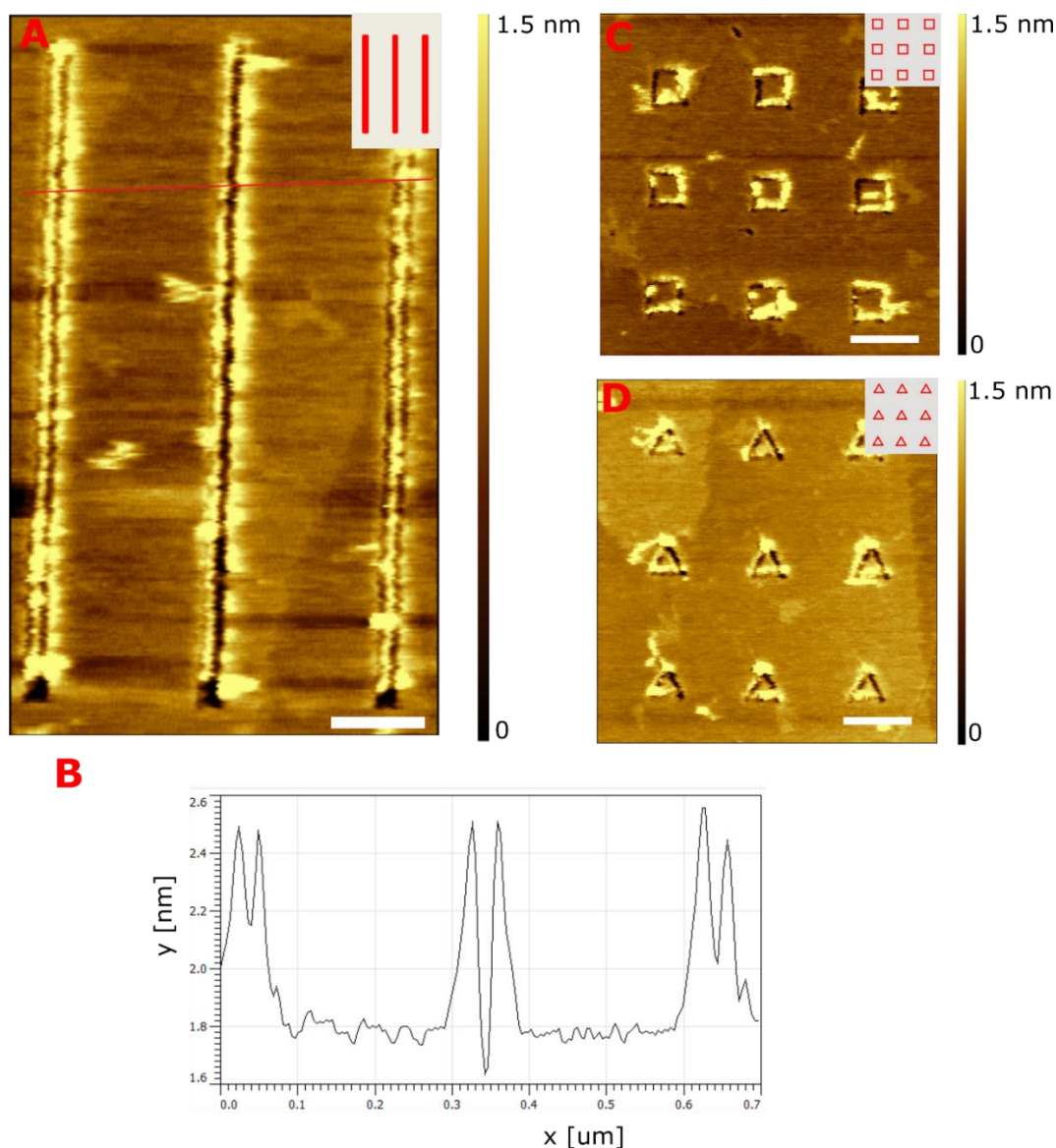


**Figure 4.9.** AFM images of dsDNA targets aligned with MUDA/MHDA boundaries. Images were acquired under 5mM Ni(II) in a 0.1x TAE buffer solution. Insets are the designs of surface patterns. Red features represent areas of MUDA and grey areas represent the host MHDA SAM. (a) DNA adhering to parallel gaps. (b) Corresponding cross-sectional profile. The heights suggest that the DNA protrudes  $\sim 2$ nm above the MUDA region. (c) DNA adhering to rectangular frames. (d) DNA adhering to triangular frames. The scale bar is 200 nm. Insets are the designs of the surface patterns.



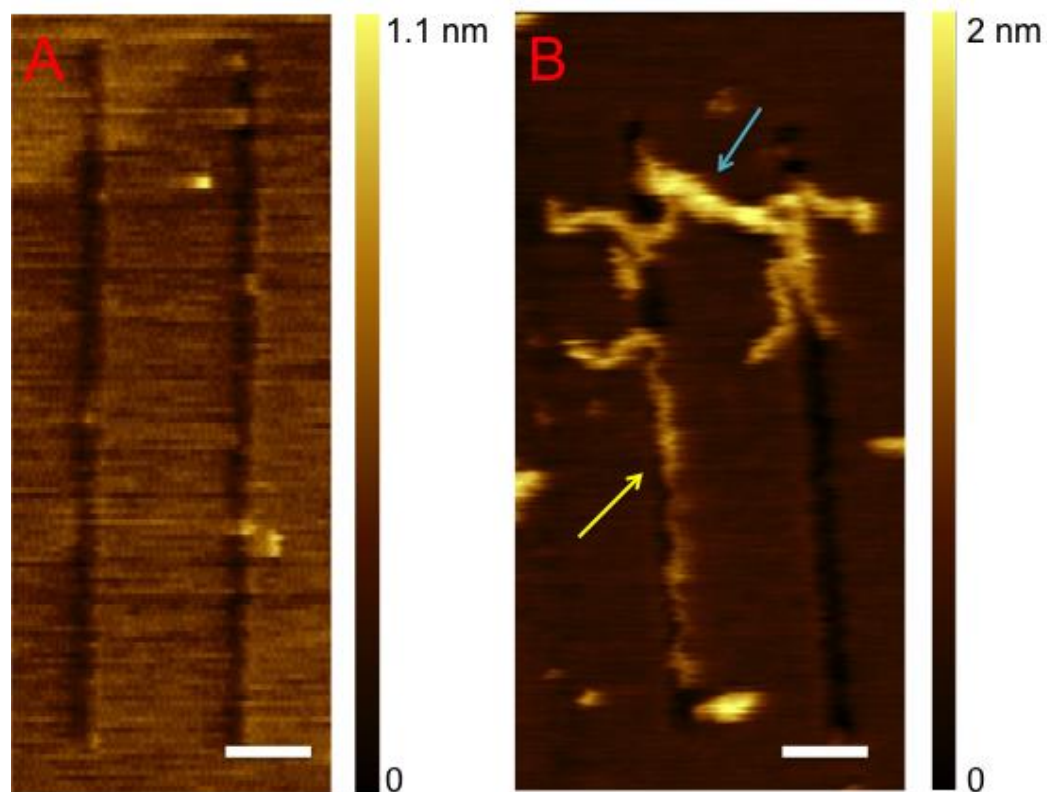


**Figure 4.10.** (a) Representative AFM image of nanografted MUDA channels with DNA probes, but without DNA hybridization. (b) AFM image of 1000 bp dsDNA aligned with MUDA/MHDA boundaries. The image was acquired under 5mM Ni(II) in 0.1x TAE buffer solution. The DNA duplex is notably longer, 320 nm. Therefore, while some of them are aligned along a trench (e.g., yellow arrow). Others may cross over to the neighboring channel (blue arrow). Scale bars are 100 nm.

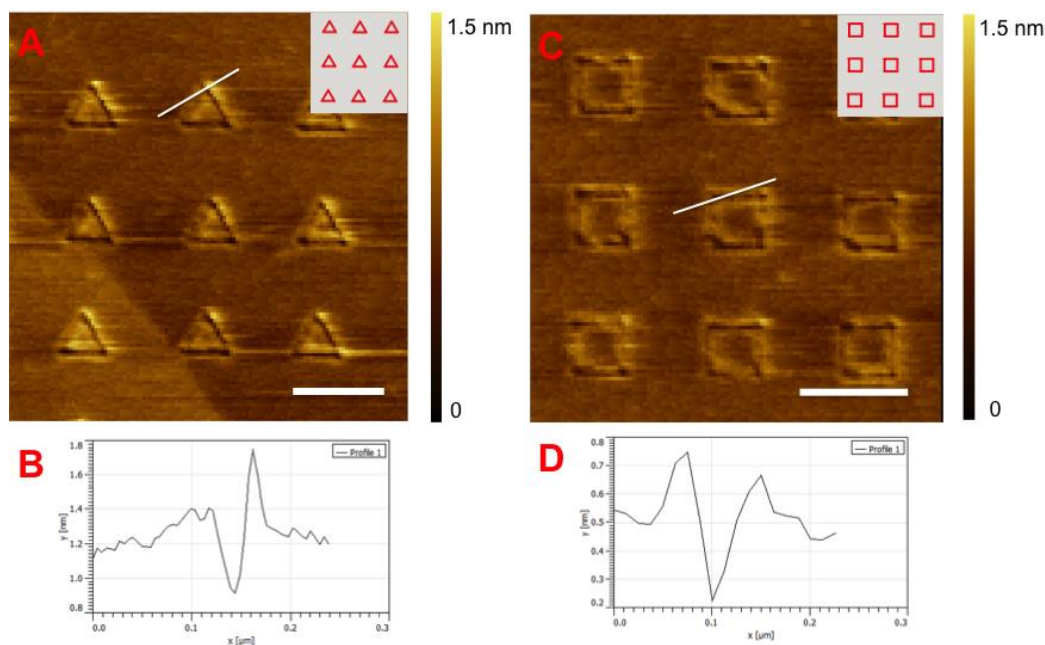


**Figure 4.11.** (a) and (c) AFM images of nanografted MUDA with DNA probe, but before dsDNA hybridization by rectangular and triangular frames, respectively. (b) and (d) are cross sectional profiles of (a) and (c), respectively. Images were acquired under a 0.1x TAE buffer solution that contained 5mM Ni(II). Insets are the designs of surface patterns. Some protrusions, 0.2-0.5 nm high, are observed at the edges. The scale bar is 200 nm. The origin of the protrusions in Figure 4.11 is unclear. It is possible that DNA probe jamming occurred in confined spaces and the DNA portion of some DNA probes was forced out of the nanografted MUDA channel and pinned atop the MHDA. Another possibility is that deformation occurred in the MHDA SAM near the nanografted region. The MHDA molecules may be forced to assume a more vertical orientation and become taller. Regardless of the origin, the height of the protrusions is much lower than 2.0 nm, the height of the protrusions in Figure 4.9.. Hence the features observed in Figure 4.9. correspond to captured dsDNA target molecules.

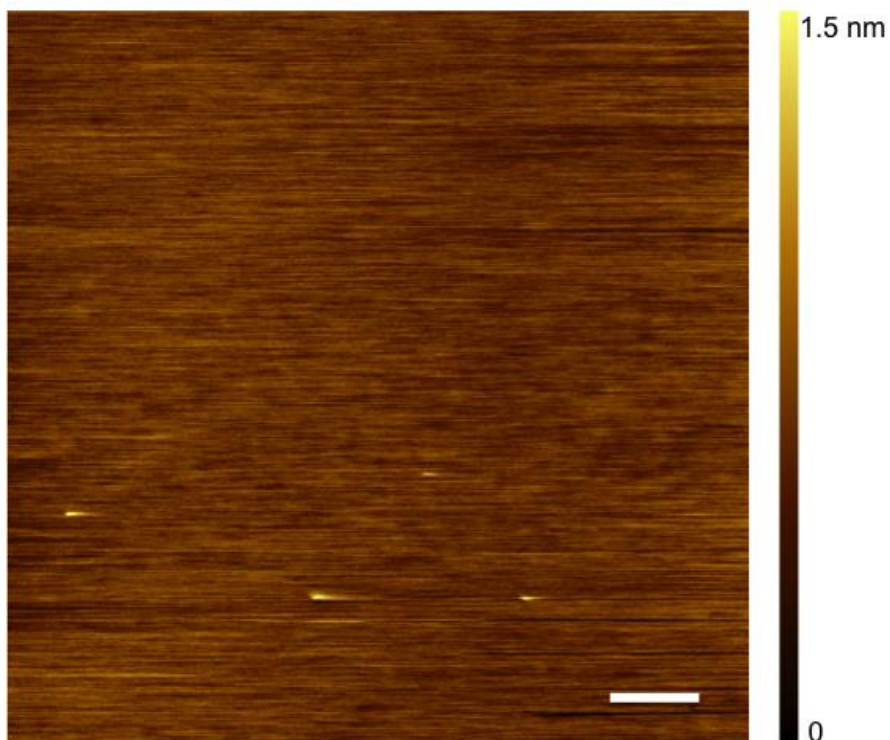


**Figure 4.12.** AFM image of non-specific adsorption of dsDNA on MHDA SAM on Au(111) surface. After exposing unpatterned MHDA SAM to a 1x TAE buffer solution containing 200 nM dsDNA targets, rinsing with the surface with the hybridization buffer, the SAM was imaged with AFM in the imaging buffer (5 mM Ni(II) in 0.1x TAE). The scale bar is 100 nm.

## References

1. Howorka, S.; Hesse, J., Microarrays and Single Molecules: An Exciting Combination. *Soft Matter* **2014**, *10* (7), 931-941.
2. Fazio, T.; Visnapuu, M. L.; Wind, S.; Greene, E. C., DNA Curtains and Nanoscale Curtain Rods: High-Throughput Tools for Single Molecule Imaging. *Langmuir* **2008**, *24* (18), 10524-10531.
3. Drmanac, R.; Sparks, A. B.; Callow, M. J.; Halpern, A. L.; Burns, N. L.; Kermani, B. G.; Carnevali, P.; Nazarenko, I.; Nilsen, G. B.; Yeung, G.; Dahl, F.; Fernandez, A.; Staker, B.; Pant, K. P.; Baccash, J.; Borcharding, A. P.; Brownley, A.; Cedenio, R.; Chen, L. S.; Chernikoff, D.; Cheung, A.; Chirita, R.; Curson, B.; Ebert, J. C.; Hacker, C. R.; Hartlage, R.; Hauser, B.; Huang, S.; Jiang, Y.; Karpinchyk, V.; Koenig, M.; Kong, C.; Landers, T.; Le, C.; Liu, J.; McBride, C. E.; Morenzoni, M.; Morey, R. E.; Mutch, K.; Perazich, H.; Perry, K.; Peters, B. A.; Peterson, J.; Pethiyagoda, C. L.; Pothuraju, K.; Richter, C.; Rosenbaum, A. M.; Roy, S.; Shafto, J.; Sharanhovich, U.; Shannon, K. W.; Sheppy, C. G.; Sun, M.; Thakuria, J. V.; Tran, A.; Vu, D.; Zaranek, A. W.; Wu, X. D.; Drmanac, S.; Oliphant, A. R.; Banyai, W. C.; Martin, B.; Ballinger, D. G.; Church, G. M.; Reid, C. A., Human Genome Sequencing Using Unchained Base Reads on Self-Assembling DNA Nanoarrays. *Science* **2010**, *327* (5961), 78-81.
4. Cerf, A.; Tian, H. C.; Craighead, H. G., Ordered Arrays of Native Chromatin Molecules for High-Resolution Imaging and Analysis. *ACS Nano* **2012**, *6* (9), 7928-7934.
5. Levy-Sakin, M.; Grunwald, A.; Kim, S.; Gassman, N. R.; Gottfried, A.; Antelman, J.; Kim, Y.; Ho, S. O.; Samuel, R.; Michalet, X.; Lin, R. R.; Dertinger, T.; Kim, A. S.; Chung, S.; Colyer, R. A.; Weinhold, E.; Weiss, S.; Ebenstein, Y., Toward Single-Molecule Optical Mapping of the Epigenome. *ACS Nano* **2014**, *8* (1), 14-26.
6. Rao, A. N.; Grainger, D. W., Biophysical Properties of Nucleic Acids at Surfaces Relevant to Microarray Performance. *Biomaterials Science* **2014**, *2* (4), 436-471.
7. Wirth, M. J.; Swinton, D. J., Single-Molecule Probing of Mixed-Mode Adsorption at a Chromatographic Interface. *Anal. Chem.* **1998**, *70* (24), 5264-5271.
8. Wertz, J.; Schwartz, D.; Kaar, J., Probing Protein Denaturation at the Solid-Liquid Interface with Single-Molecule Fluorescent Microscopy. *Abstr. Pap. Am. Chem. S.* **2015**, *249*.
9. Langdon, B. B.; Mirhossaini, R. B.; Mabry, J. N.; Sriram, I.; Lajmi, A.; Zhang, Y. X.; Rojas, O. J.; Schwartz, D. K., Single-Molecule Resolution of

Protein Dynamics on Polymeric Membrane Surfaces: The Roles of Spatial and Population Heterogeneity. *Acs. Appl. Mater. Inter.* **2015**, *7*(6), 3607-3617.

10. Rao, A. N.; Vandencastele, N.; Gamble, L. J.; Grainger, D. W., High-Resolution Epifluorescence and Time-of-Flight Secondary Ion Mass Spectrometry Chemical Imaging Comparisons of Single DNA Microarray Spots. *Anal. Chem.* **2012**, *84*(24), 10628-10636.
11. Nelson, N.; Schwartz, D. K., Unbiased Clustering of Molecular Dynamics for Spatially Resolved Analysis of Chemically Heterogeneous Surfaces. *Langmuir* **2015**, *31*(22), 6099-6106.
12. Palma, M.; Abramson, J. J.; Gorodetsky, A. A.; Penzo, E.; Gonzalez, R. L.; Sheetz, M. P.; Nuckolls, C.; Hone, J.; Wind, S. J., Selective Biomolecular Nanoarrays for Parallel Single-Molecule Investigations. *J. Am. Chem. Soc.* **2011**, *133*(20), 7656-7659.
13. Sassolas, A.; Blum, L. J.; Leca-Bouvier, B. D., Immobilization Strategies to Develop Enzymatic Biosensors. *Biotechnology Advances* **2012**, *30*(3), 489-511.
14. Josephs, E. A.; Ye, T., A Single-Molecule View of Conformational Switching of DNA Tethered to a Gold Electrode. *J. Am. Chem. Soc.* **2012**, *134*(24), 10021-10030.
15. Israelachvili, J. N.; Drummond, C., On the Conformational State of Molecules in Molecularly Thin Shearing Films. *P. Natl. Acad. Sci. USA* **2015**, *112*(36), E4973-E4973.
16. Qin, D.; Xia, Y. N.; Whitesides, G. M., Soft Lithography for Micro- and Nanoscale Patterning. *Nat. Protoc.* **2010**, *5*(3), 491-502.
17. Salaita, K.; Wang, Y. H.; Mirkin, C. A., Applications of Dip-Pen Nanolithography. *Nat. Nanotechnol.* **2007**, *2*(3), 145-155.
18. Vezenov, D. V.; Noy, A.; Rozsnyai, L. F.; Lieber, C. M., Force Titrations and Ionization State Sensitive Imaging of Functional Groups in Aqueous Solutions by Chemical Force Microscopy. *J. Am. Chem. Soc.* **1997**, *119*(8), 2006-2015.
19. Peterson, A. W.; Heaton, R. J.; Georgiadis, R. M., The Effect of Surface Probe Density on DNA Hybridization. *Nucleic Acids Res.* **2001**, *29*(24), 5163-5168.
20. Gong, P.; Levicky, R., DNA Surface Hybridization Regimes. *P. Natl. Acad. Sci. USA* **2008**, *105*(14), 5301-5306.
21. Fan, C. H.; Plaxco, K. W.; Heeger, A. J., Electrochemical Interrogation of Conformational Changes as a Reagentless Method for the Sequence-Specific Detection of DNA. *P. Natl. Acad. Sci. USA* **2003**, *100*(16), 9134-9137.

22. Monserud, J. H.; Schwartz, D. K., Mechanisms of Surface-Mediated DNA Hybridization. *ACS Nano* **2014**, *8* (5), 4488-4499.
23. Wang, D.; Gou, S. Y.; Axelrod, D., Reaction-Rate Enhancement by Surface-Diffusion of Adsorbates. *Biophys. Chem.* **1992**, *43* (2), 117-137.
24. Herne, T. M.; Tarlov, M. J., Characterization of DNA Probes Immobilized on Gold Surfaces. *J. Am. Chem. Soc.* **1997**, *119* (38), 8916-8920.
25. Drummond, T. G.; Hill, M. G.; Barton, J. K., Electrochemical DNA Sensors. *Nature Biotechnology* **2003**, *21* (10), 1192-1199.
26. Rant, U.; Pringsheim, E.; Kaiser, W.; Arinaga, K.; Knezevic, J.; Tornow, M.; Fujita, S.; Yokoyama, N.; Abstreiter, G., Detection and Size Analysis of Proteins with Switchable DNA Layers. *Nano Lett.* **2009**, *9* (4), 1290-1295.
27. Chen, Y. L.; Nguyen, A.; Niu, L. F.; Corn, R. M., Fabrication of DNA Microarrays with Poly(L-Glutamic Acid) Monolayers on Gold Substrates for Spr Imaging Measurements. *Langmuir* **2009**, *25* (9), 5054-5060.
28. Demers, L. M.; Ginger, D. S.; Park, S. J.; Li, Z.; Chung, S. W.; Mirkin, C. A., Direct Patterning of Modified Oligonucleotides on Metals and Insulators by Dip-Pen Nanolithography. *Science* **2002**, *296* (5574), 1836-1838.
29. Josephs, E. A.; Ye, T., Nanoscale Spatial Distribution of Thiolated DNA on Model Nucleic Acid Sensor Surfaces. *ACS Nano* **2013**, *7* (4), 3653-3660.
30. Cao, H. H.; Nakatsuka, N.; Serino, A. C.; Liao, W. S.; Cheunkar, S.; Yang, H. Y.; Weiss, P. S.; Andrews, A. M., Controlled DNA Patterning by Chemical Lift-Off Lithography: Matrix Matters. *ACS Nano* **2015**, *9* (11), 11439-11454.
31. Macazo, F. C.; Karpel, R. L.; White, R. J., Monitoring Cooperative Binding Using Electrochemical DNA-Based Sensors. *Langmuir* **2015**, *31* (2), 868-875.
32. Yang, L.; Zhang, C. H.; Jiang, H.; Li, G. J.; Wang, J. H.; Wang, E. K., Insertion Approach: Bolstering the Reproducibility of Electrochemical Signal Amplification Via DNA Superstructures. *Anal. Chem.* **2014**, *86* (10), 4657-4662.
33. Abel, G. R., Jr.; Josephs, E. A.; Luong, N.; Ye, T., A Switchable Surface Enables Visualization of Single DNA Hybridization Events with Atomic Force Microscopy. *J. Am. Chem. Soc.* **2013**, *135* (17), 6399-6402.
34. Doni, G.; Ngavouka, M. D. N.; Barducci, A.; Parisse, P.; De Vita, A.; Scoles, G.; Casalis, L.; Pavan, G. M., Structural and Energetic Basis for Hybridization Limits in High-Density DNA Monolayers. *Nanoscale* **2013**, *5* (20), 9988-9993.
35. Liu, M.; Amro, N. A.; Liu, G. Y., Nanografting for Surface Physical Chemistry. *Annu. Rev. Phys. Chem.* **2008**, *59*, 367-386.

36. Murphy, J. N.; Cheng, A. K. H.; Yu, H. Z.; Bizzotto, D., On the Nature of DNA Self-Assembled Monolayers on Au: Measuring Surface Heterogeneity with Electrochemical in Situ Fluorescence Microscopy. *J. Am. Chem. Soc.* **2009**, *131* (11), 4042-4050.
37. Liu, B. W.; Liu, J. W., Comprehensive Screen of Metal Oxide Nanoparticles for DNA Adsorption, Fluorescence Quenching, and Anion Discrimination. *Acs. Appl. Mater. Inter.* **2015**, *7*(44), 24833-24838.
38. Mirmomtaz, E.; Castronovo, M.; Grunwald, C.; Bano, F.; Scaini, D.; Ensafi, A. A.; Scoles, G.; Casalis, L., Quantitative Study of the Effect of Coverage on the Hybridization Efficiency of Surface-Bound DNA Nanostructures. *Nano Lett.* **2008**, *8*(12), 4134-4139.
39. Woo, S.; Rothmund, P. W. K., Self-Assembly of Two-Dimensional DNA Origami Lattices Using Cation-Controlled Surface Diffusion (Vol 5, 4889, 2014). *Nat. Commun.* **2014**, *5*.
40. Josephs, E. A.; Shao, J. R.; Ye, T., Nanografting Sodium Dodecyl Sulfate under Potential Control: New Insights into Tip-Directed Molecular Assembly. *Nanoscale* **2013**, *5*(10), 4139-4143.
41. Abel, G. R.; Cao, B. H.; Hein, J. E.; Ye, T., Covalent, Sequence-Specific Attachment of Long DNA Molecules to a Surface Using DNA-Templated Click Chemistry. *Chem. Commun.* **2014**, *50*(60), 8131-8133.
42. Rivetti, C.; Guthold, M.; Bustamante, C., Scanning Force Microscopy of DNA Deposited onto Mica: Equilibration Versus Kinetic Trapping Studied by Statistical Polymer Chain Analysis. *J. Mol. Biol.* **1996**, *264* (5), 919-932.
43. Hansma, H. G.; Laney, D. E., DNA Binding to Mica Correlates with Cationic Radius: Assay by Atomic Force Microscopy. *Biophys. J.* **1996**, *70* (4), 1933-1939.
44. Rouzina, I.; Bloomfield, V. A., Influence of Ligand Spatial Organization on Competitive Electrostatic Binding to DNA. *J. Phys. Chem. USA* **1996**, *100* (10), 4305-4313.
45. Gronbech-Jensen, N.; Mashl, R. J.; Bruinsma, R. F.; Gelbart, W. M., Counterion-Induced Attraction between Rigid Polyelectrolytes. *Phys. Rev. Lett.* **1997**, *78*(12), 2477-2480.
46. Kang, S. H.; Shortreed, M. R.; Yeung, E. S., Real-Time Dynamics of Single-DNA Molecules Undergoing Adsorption and Desorption at Liquid-Solid Interfaces. *Anal. Chem.* **2001**, *73*(6), 1091-1099.
47. Josephs, E. A.; Ye, T., Electric-Field Dependent Conformations of Single DNA Molecules on a Model Biosensor Surface. *Nano Lett.* **2012**, *12*(10), 5255-5261.

48. Jing, J. P.; Reed, J.; Huang, J.; Hu, X. H.; Clarke, V.; Edington, J.; Housman, D.; Anantharaman, T. S.; Huff, E. J.; Mishra, B.; Porter, B.; Shenker, A.; Wolfson, E.; Hiort, C.; Kantor, R.; Aston, C.; Schwartz, D. C., Automated High Resolution Optical Mapping Using Arrayed, Fluid-Fixed DNA Molecules. *P. Natl. Acad. Sci. USA* **1998**, *95* (14), 8046-8051.
49. Tanaka, H.; Kawai, T., Partial Sequencing of a Single DNA Molecule with a Scanning Tunnelling Microscope. *Nat. Nanotechnol.* **2009**, *4* (8), 518-522.
50. Sternberg, S. H.; Redding, S.; Jinek, M.; Greene, E. C.; Doudna, J. A., DNA Interrogation by the Crispr Rna-Guided Endonuclease Cas9. *Nature* **2014**, *507*(7490), 62.
51. Bensimon, A.; Simon, A.; Chiffaudel, A.; Croquette, V.; Heslot, F.; Bensimon, D., Alignment and Sensitive Detection of DNA by a Moving Interface. *Science* **1994**, *265* (5181), 2096-2098.
52. Matsuoka, T.; Kim, B. C.; Huang, J. X.; Douville, N. J.; Thouless, M. D.; Takayama, S., Nanoscale Squeezing in Elastomeric Nanochannels for Single Chromatin Linearization. *Nano Lett.* **2012**, *12* (12), 6480-6484.
53. Sun, X. P.; Ko, S. H.; Zhang, C. A.; Ribbe, A. E.; Mao, C. D., Surface-Mediated DNA Self-Assembly. *J. Am. Chem. Soc.* **2009**, *131* (37), 13248-13249.
54. Kershner, R. J.; Bozano, L. D.; Micheel, C. M.; Hung, A. M.; Fornof, A. R.; Cha, J. N.; Rettner, C. T.; Bersani, M.; Frommer, J.; Rothmund, P. W. K.; Wallraff, G. M., Placement and Orientation of Individual DNA Shapes on Lithographically Patterned Surfaces. *Nat. Nanotechnol.* **2009**, *4* (9), 557-561.
55. Rafat, A. A.; Pirzer, T.; Scheible, M. B.; Kostina, A.; Simmel, F. C., Surface-Assisted Large-Scale Ordering of DNA Origami Tiles. *Angew. Chem. Int. Edit.* **2014**, *53* (29), 7665-7668.



## Chapter 5

### Conclusions and future study

I listen to cicadas singing dolefully in the cold from across the gallery at dusk, the sudden rain has just come to a halt. She puts out a farewell toast outside a capital gate, yet dejected is the mood, while I wish to linger, ready to row off is the magnolia canoe. Holding hands, we look into each other's teary eyes, yet unable to words utter, on emotions we choke. As I think of the flow of misty waters that undulate for thousands of miles, leaden is the evening clouds that occupy the vast southern skies. As always, the romantic fear adieu the most, how especially so in this dismal fall! Where will I be when I recover from insobriety tonight? Perhaps somewhere along a willowy bank, in a breeze under a waning moon. This time for years I'll be gone, what should be brilliant days and beautiful scenery shall be of little use. Even though I may possess inexhaustible passion, whom have I to offer it to?

Liu Yong, Lyric to Tinkling Heavy Rain

## 5.1. Summary and conclusion

Biosensors capable of specifically detecting small quantities of analytes in complex biofluids are under active development in many laboratories. However, despite intense efforts, it remains challenging to engineer biosensors with the required sensitivity, selectivity and reproducibility. One of the root causes is the lack of understanding and control of how nanoscale surface heterogeneities impact molecular recognition. In this dissertation, we developed a single-molecule AFM (SM-AFM) imaging technique to characterize the spatial distribution and molecular structures of immobilized probes on functioning biosensing surfaces, which was not accessible by conventional ensemble-averaging or single-molecule techniques. The goal of the work in this dissertation is to quantify and manipulate the surface heterogeneities at nanoscale, thus establishing a structure-function relationship for the fabrication of highly efficient biosensor devices.

In chapter 2, we applied this strategy to a functioning electrochemical DNA (E-DNA) sensor. By spatially resolving surface hybridization and applying new single-molecule spatial statistical tools, we have for the first time characterized the spatial patterns of single molecules and correlated these patterns to interfacial molecular recognition. This novel framework led to a number of surprising findings. First, the probe distribution is highly heterogeneous as opposed to the idealized grid-like organization; second, the crowding interactions between structured probe molecules may enhance target binding under specific conditions, which raises the intriguing prospect that the spatial patterns of biosensor surfaces can be rationally tailored to improve the performance.

Inspired by the finding that the surface heterogeneity has tremendous impact on target recognition, we took a step further by developing a new model that connects nanoscale spatial patterns to surface hybridization kinetics (chapter 3). We have successfully rationalized and predicted the counter-intuitive trends in surface hybridization of a model electrochemical DNA sensor. The successes provide the clearest evidence that the lateral spatial patterns of the DNA probe molecules are a major determinant of the behaviors of surface hybridization. The study opens up new avenues in tailoring the spatial organization of the probe molecules to develop more sensitive and reproducible sensors and microarrays.

In chapter 4, we explored how nanometer-scale interactions with the chemical and morphological heterogeneities of the solid support affect the properties of the DNA and how these interactions can be exploited to control their molecular properties. We generated arrays of individually resolvable DNA molecules tethered to nanometer-scale patterns of alkanethiol monolayers that possess tailored surface heterogeneities. Using SM-AFM to probe the conformations of the DNA molecules interacting with these surface

features, we found that the DNA conformations are highly sensitive to both the chemical functionality and sub-nanometer variations in the topographical height of carboxyl-terminated self-assembled monolayers onto which they were deposited. By exploiting the sensitivity of the DNA-surface interactions to the presence of divalent cations, we aligned the DNA into a range of shapes that follow the engineered chemical patterns but deviate significantly from their native conformations. Knowledge of how the nanoscale chemical functionality and morphology of arrayed surfaces impact the properties of DNA can enable effective means to control their molecular conformations at interfaces and enable new applications in DNA biosensor fabrication.

## 5.2. Directions for future research

The functionality of molecular ensembles depends not only on individual building blocks but also the organization at molecular level. Our previous studies have shown that sub-10 nm variation in the intermolecular spacing has drastic influences on target recognition.<sup>1</sup> A more thorough research into this relationship ideally requires nanometer-sized patterning of biomolecules. DNA nanostructures have been used to precisely position biomolecules and chemicals that can then be transferred to substrates. Thus these structures can serve as a platform to pattern biomolecules.<sup>2-5</sup> However, the lack of means of directly resolving the spatial pattern of grafted DNA probe molecules and characterizing the target capture prevents the development of a structure-function relationship. The SM-AFM imaging technique presented in this dissertation could be used to address this challenge. Herein, we report a combination of DNA nanostructure-assisted lithography and SM-AFM imaging to selectively deposit DNA origami structures functionalized with spatially patterned capture strand DNAs on a dynamically switchable surface, resulting in a spatially ordered 2D assembly of DNA capture probes that can be directly resolved by AFM.

We controlled the spacing between DNA probes on the substrate through careful design of DNA nanostructures. As an example, we designed mini-rectangular DNA nanostructures possessing a pair of thiolated staples (capture probes) separated by a distance of about 10.3 nm (highlighted in green and purple in Figure 5.1) and inserted them into a MUDA SAM preassembled on gold surface (Figure 5.2a). A mini-DNA tile design was used to ensure a minimum surface probe coverage ( $>10^{10}$  probes/cm<sup>2</sup>) required for practical DNA biosensors.<sup>6</sup> The staple and scaffold sequences are designed using caDNAno software<sup>7</sup> and summarized in Table 5.1 and 5.2, respectively. The 10-base poly T extension on thiolated staples was used to minimize the non-specific adsorption of DNA tiles on surface and facilitate the formation of gold-thiol bonds.

DNA origami folding was performed by incubating a solution of 5 nM DNA scaffold, 25 nM for each DNA staple and 1M NaAc according to the following

annealing protocol: 90°C for 5 min and controlled cooling from 90°C to 20°C (1 min per °C). We have explored different compositions and a folding buffer containing Na<sup>+</sup> instead of Mg<sup>2+</sup> was used here to minimize the nonspecific adsorption of DNA origami tiles and ensure the specific adsorption of thiols, since Mg<sup>2+</sup>-mediated attractive interactions between DNA and carboxyl terminated SAM were observed in our previous work (no attractive interactions were observed in the presence of Na<sup>+</sup>).<sup>8</sup> The folded DNA origami tiles were incubated with 0.2 mM TCEP and used for deposition without further purification. It should be noted that Amicon columns cannot be used for the purification of mini-DNA tiles because of the large pore size on membrane and the use of larger DNA nanostructures may be expected in future studies. A sample of folded mini-DNA tiles were directly deposited on the gold surface passivated with MUDA SAM for 1 hour for covalent bonds to be formed between thiol and gold. The adsorption of DNA tiles on SAM surface is important as it encourages the insertion of thiolated capture staples. When the inserted DNA tiles were denatured with an alkaline buffer (1xAB = 10 mM NaOH, 330 uM EDTA, pH 12) to remove the DNA origami frame, *i.e.*, DNA scaffolds and free staples without thiol group, the thiolated staple pairs can be exposed (Figure 5.2a). As depicted in Figure 5.2b, both the inserted DNA tiles (left panel) and the exposed pairs of thiolated staples after denaturation (right panel) can be directly resolved by AFM. Spatial statistical analysis yields a mean NND value of  $7.3 \pm 2.0$  nm (left panel of Figure 5.2c) that is comparable to the expected separation distance of about 10.3 nm for a pair of thiolated staples, confirming a successful patterning of DNA probes on surface. This is further supported by its counterpart fabricated using insertion method exhibiting a random distribution with a mean NND of  $20.5 \pm 2.0$  nm (right panel of Figure 5.2c). We also used the mini-DNA tile without thiolated staples as a control (Figure 5.2d). The absence of probes on the surface confirmed that the surface-bound staples are all transferred from the DNA tiles. Although these initial results are promising, there are still a small number of DNA tiles remaining on the surface (right panel in Figure 5.2d), indicating a small amount of nonspecific adsorption of DNA tiles. Overall, this approach verifies the feasibility and fidelity of using DNA nanostructure to precisely control the spacing between individual probes on the biosensor surface.

Based on these initial results, further investigation on how hybridization performance varies at different inter-probe separations can be performed. Specifically, instead of the two staples in the middle, the staples at the edge of DNA origami structure (highlighted in red in Figure 5.1) will be modified as capture probes. A set of inter-probe distance can be obtained depending on the choice of staples located at different positions of DNA origami tile. Given that each staple on DNA tile has a unique sequence, the use of more than two thiolated staples will allow us to further explore the effect of the number of neighboring DNA probes on target recognition. In addition to the mini-DNA

tiles, the use of larger 2D and rigid 3D-DNA nanostructures would facilitate greater variability in spacing and alignment, allowing intricate probe layer structure to be fabricated. Eventually, we can also take into account the effect of target size and probe design as both are found to greatly impact the molecular recognition.<sup>6</sup>

Compared to the insertion method used in this dissertation, the DNA nanostructure-assisted patterning of DNA probes allowing the addressability of matter on surfaces with sub-10 nm precision represents an improvement in controlling the spatial patterns of probe molecules. This methodology can precisely control the inter-probe spacing of biosensor surface and optimize the sensing performance. Future studies could lead to the implementation of this methodology into multiplexed microfluidic<sup>9</sup> and multifractional sensing systems.<sup>10</sup>

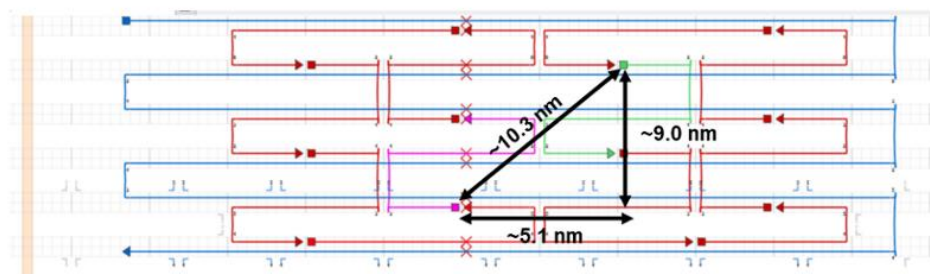
**Table 5.1.** DNA staple sequences (listed from 5' to 3' end direction).

Start	End	Staple Sequences for Mini DNA Tile	Length
4[79]	2[80]	ATTGTGAACAGTTGAG ATTTAGGACAACATAAT	32
1[64]	3[63]	SS-(CH <sub>2</sub> ) <sub>11</sub> - <i>TTTTTTTTTTTTTT</i> GCCAGATAACGCC AAAAGGAAAGGTAGAA	10+32
0[79]	1[63]	GTCCAATACTGCGGAAT CGTCATAAAAAGAAGT	32
5[72]	4[80]	TTGGGCTTGAGA TGGTCTTTAATC	24
0[47]	1[31]	ATTGAATCCCCCTCAA ATGCTTTAATAAAAAC	32
4[47]	2[48]	SS-(CH <sub>2</sub> ) <sub>11</sub> - <i>TTTTTTTTTTTTTT</i> GGCTCAT GAACAACATTACTTACGAG	10+30
3[32]	5[31]	AACTAACGTATAACCAG TCAGGACGAGTGAATA	32
2[79]	0[80]	GCAGATACAGGGGGTA ATAGTAAATGGATAGC	32
1[32]	3[31]	CAAATAGAGAGCAAC ACTATCATATAAAACG	32
5[32]	4[48]	AGGCTTGCCCTGACG AGAAACACTAAGAAC	30
3[64]	5[71]	AGATTCATTTACCTTATGCG ATTCAGAACGAGTAGTAAA	40
2[47]	0[48]	GCATAGTACGAGAGG CTTTTGCAAATATTC	30

**Table 5.2.** DNA scaffold sequence (listed from 5' to 3' end direction).

```
tctgaactgtttaaagcatttgaggggattcaatgaatatttatgacgattccgcagtattgga  
cgctatccagtcataaacattttactattaccctctggcaaaactcttttgcaaaagcctctgc  
tattttggttttatcgtcgtctggtaaacgagggttatgatagtggtgcttactatgcctcgta  
attcctttggcgttatgtatctgcattagttgaatgtggtattcctaaatcactgatgaatct  
ttctacctgaataatggtggtccgtagttcgttttattaacgtagatttttctccaacgtcctg  
actggtataatgagccagttctaaaatcgcataaggaattcacaatgattaaagttgaaatt  
aaaccatctcaagccaatttactactcgttctggtggttctcgtcagggcaagccttattcactg  
aatgagcagc
```

a



b

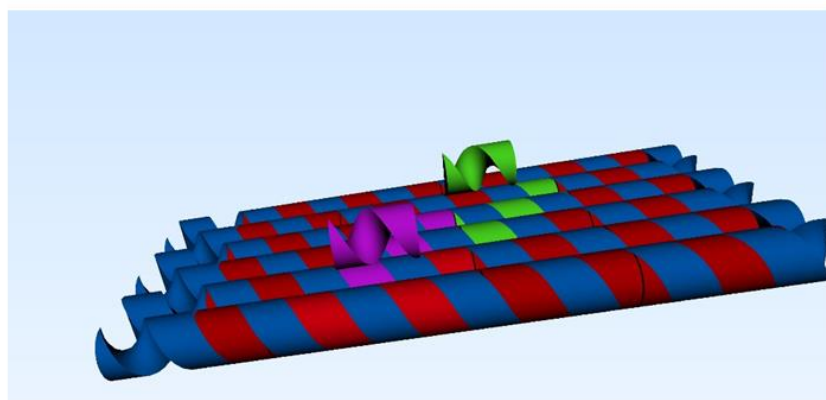


**Figure 5.1.** CaDNAno diagram and scheme of mini DNA tiles. (a) CaDNAno diagram showing the mini DNA tiles with 12 DNA staples (two thiolated DNA staples are highlighted by purple and green respectively) on the square lattice. (b) Scheme of the mini DNA tile and attached DNA probes (purple and green).



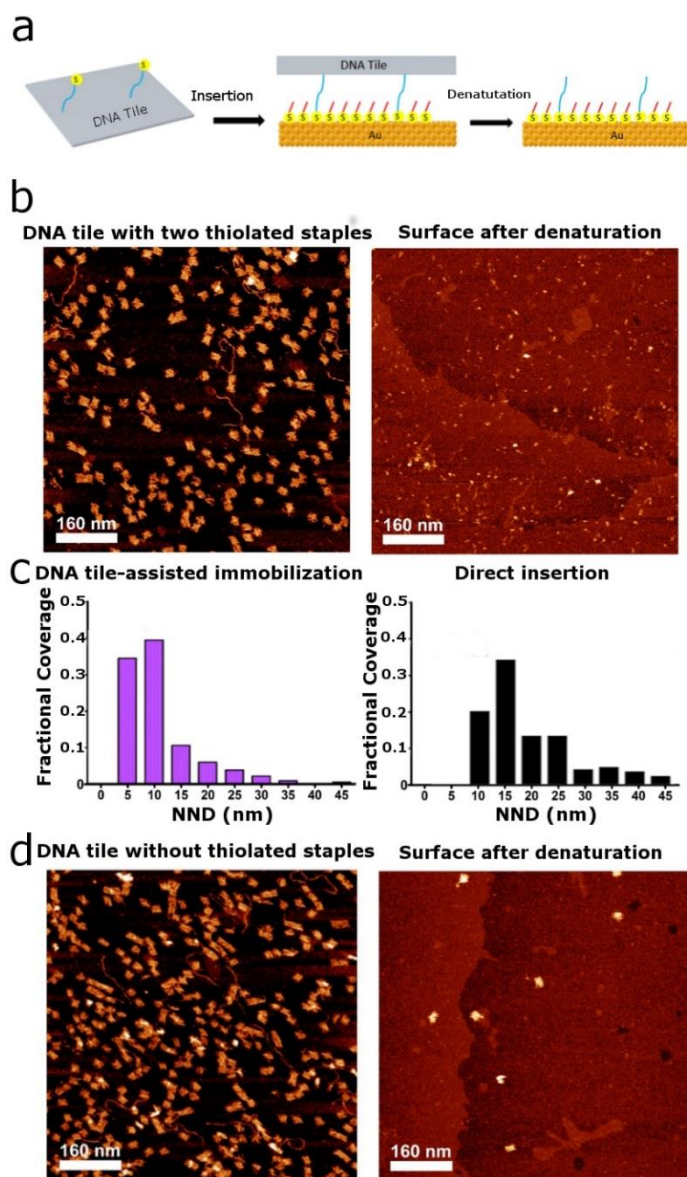


**Figure 5.2.** Methodology to transfer probe spatial pattern to surfaces. (a) Schematic of DNA-origami-assisted lithography. DNA mini tiles possessing a pair of thiolated probe staples are inserted into a MUDA SAM preassembled on Au(111) surface. The immobilized DNA tiles are then denatured with formamide and rinsed out to expose the surface-bound probe staples. (b) AFM images of DNA mini tiles possessing thiolated probe staples before (left) and after (right) denaturation. (c) Histograms of probes distribution as a function of NND using DNA tile-assisted immobilization (left panel) and direct insertion (right panel) at similar probe density. (d) AFM images of DNA mini tiles without thiolated probe staples before (left) and after (right) denaturation.

## References

1. Gu, Q. F.; Nanney, W.; Cao, H. H.; Wang, H. Y.; Ye, T., Single Molecule Profiling of Molecular Recognition at a Model Electrochemical Biosensor. *J. Am. Chem. Soc.* **2018**, *140* (43), 14134-14143.
2. Gallego, I.; Manning, B.; Prades, J. D.; Mir, M.; Samitier, J.; Eritja, R., DNA-Origami-Driven Lithography for Patterning on Gold Surfaces with Sub-10 Nm Resolution. *Adv. Mater.* **2017**, *29* (11).
3. Sajfutdinow, M.; Uhlig, K.; Prager, A.; Schneider, C.; Abel, B.; Smith, D. M., Nanoscale Patterning of Self-Assembled Monolayer (SAM)-Functionalised Substrates with Single Molecule Contact Printing. *Nanoscale* **2017**, *9* (39), 15098-15106.
4. Lin, M. H.; Wang, J. J.; Zhou, G. B.; Wang, J. B.; Wu, N.; Lu, J. X.; Gao, J. M.; Chen, X. Q.; Shi, J. Y.; Zuo, X. L.; Fan, C. H., Programmable Engineering of a Biosensing Interface with Tetrahedral DNA Nanostructures for Ultrasensitive DNA Detection. *Angew. Chem. Int. Edit.* **2015**, *54* (7), 2151-2155.
5. Edwardson, T. G. W.; Lau, K. L.; Bousmail, D.; Serpell, C. J.; Sleiman, H. F., Transfer of Molecular Recognition Information from DNA Nanostructures to Gold Nanoparticles. *Nat. Chem.* **2016**, *8* (2), 162-170.
6. Ricci, F.; Lai, R. Y.; Heeger, A. J.; Plaxco, K. W.; Sumner, J. J., Effect of Molecular Crowding on the Response of an Electrochemical DNA Sensor. *Langmuir* **2007**, *23* (12), 6827-6834.
7. Douglas, S. M.; Marblestone, A. H.; Teerapittayanon, S.; Vazquez, A.; Church, G. M.; Shih, W. M., Rapid Prototyping of 3d DNA-Origami Shapes with Cadnano. *Nucleic Acids Res.* **2009**, *37* (15), 5001-5006.
8. Cao, H. H.; Abel, R. A.; Gu, Q.; Gueorguieva, G. V.; Zhang, Y.; Nanney, W. A.; Provencio, E. T.; Ye, T. Seeding the Self-Assembly of DNA Origamis at Surfaces. *ACS Nano* **2020**, forthcoming.
9. Whitesides, G. M., The Origins and the Future of Microfluidics. *Nature* **2006**, *442* (7101), 368-373.
10. Johnson-Buck, A.; Nangreave, J.; Jiang, S.; Yan, H.; Walter, N. G., Multifactorial Modulation of Binding and Dissociation Kinetics on Two-Dimensional DNA Nanostructures. *Nano Lett.* **2013**, *13* (6), 2754-2759.